Thermal transport in three-dimensional nanoarchitected materials

Thesis by
Nicholas Gang Dou

In Partial Fulfillment of the Requirements for the
Degree of
Doctor of Philosophy

CALIFORNIA INSTITUTE OF TECHNOLOGY
Pasadena, California

2018
Defended April 13, 2018

© 2018

Nicholas Gang Dou
ORCID: 0000-0001-8199-5588

All rights reserved

ACKNOWLEDGEMENTS

During the course of my Ph.D., I sometimes felt like a heat-carrying particle in the vast expanse of an unexplored scientific domain. The trajectory of my research seemed like a random walk—every path I took led me back to where I started. Fortunately, the momentum and direction imparted to me through interactions with many extraordinary people has not only allowed me to accomplish the work reported in this dissertation, but also helped me to grow as a scientist and as a person. To these people, I am eternally grateful.

First I want to thank my advisor, Prof. Austin Minnich, for his thoughtful guidance and steadfast support throughout my graduate studies. He gave me tremendous freedom to forge my own path (and make mistakes), but also offered me useful suggestions upon request. Whenever I encountered difficulties, I could always rely on him for sensible advice and encouragement. His dedication to the advancement of science and to the development of his advisees is truly admirable. I am very thankful that I got the opportunity to learn from him.

I also extend my gratitude to my thesis committee members, Prof. Julia Greer, Prof. Guillaume Blanquart, and Prof. Melany Hunt for giving me useful feedback at critical academic milestones and for helping to make the MCE department such a friendly and close-knit community. I am particularly grateful to Julia for her valuable insights regarding the mechanics aspects of our research collaboration.

Thanks to the Minnich group and alumni for teaching me about nanoscale heat transfer and for providing comments and criticisms on countless practice talks. Thanks especially to Xiangwen Chen, who taught me TDTR and many other lab skills; and to Chengyun Hua and Navaneeth Ravichandran, who helped me learn and implement the Monte Carlo algorithm. Thanks also to Andrew Robbins, Nate Thomas, Zoila Jurado, and Peshi Cheng, who were great officemates and sources of random knowledge; and to Jaeyun Moon, Taeyong Kim, Junlong Kou, and Nina Shulumba, for many fun and interesting discussions.

Thanks to the Greer group and alumni for helping me with nanolattice fabrication and mechanical testing. Thanks especially to Lucas Meza, who first trained me on how to make nanolattices and paved the way for our thermal nanolattices work; to Carlos Portela, who performed mechanical experiments and simulations for our paper; and to Rob Jagt, who not only created many of the thermal samples, but

also assisted with building and troubleshooting the 3ω setup. Thanks also to Arturo Mateos, Alessando Maggi, and Xiaoxing Xia for their fabrication assistance.

I am thankful for the support of many Caltech staff, including the wonderful MCE administrative assistants, Maria Koeper, Cheryl Geer, Sonya Lincoln, Lynn Seymour, and Holly Golcher; and the incredibly helpful KNI staff, Melissa Melendes, Matt Sullivan, Alex Wertheim, and Steven Martinez. I acknowledge the support of the Resnick Sustainability Institute in my first year, and thank Dr. Neil Fromer for our regular conversations about my research.

Many of my classmates and peers have also become my close friends—they are the reason why my time at Caltech has been so enjoyable and will be so memorable. Thanks to Tess, Andres, Alex, Francesco, and Gerry for introducing me to hiking and climbing, and for inviting me to nice dinners and board game nights. Thanks to Natalie for always lending an ear in my times of need. Thanks to Andrew, Chengyun, and Ishan for many awesome outdoor adventures. To Kevin, Ishan, Dingyi, Reid, and Sean, thanks for being my 1055 Fam and 4-1 Crew. I will never forget our shenanigans. To Amber, thanks for always making me happy and for being there for me through thick and thin.

Finally, to my mother and father, thank you for supporting my education since childhood and for making every effort to set me up for success. I could not have done it without you.

ABSTRACT

Materials that simultaneously possess ultralow thermal conductivity, high stiffness, and damage tolerance are highly desirable for engineering applications. However, this combination of properties has never been demonstrated in a single material because thermal and mechanical properties are coupled in most fully dense and porous solids. A new class of lattice materials with nanoscale features, called nanolattices, can fill this void in the material property space by virtue of their architecture and nanoscale dimensions. Extensive work on nanolattice mechanical properties report their excellent stiffness-to-density ratio and recoverability from large compressive strains. In contrast, the framework for studying their thermal properties has not been established. Our work develops the computational and experimental tools necessary to study heat conduction in nanoarchitected materials and applies those tools to prove the viability of octet-truss nanolattices as multifunctional thermal insulators.

We implement significant improvements to a phonon Monte Carlo method to solve the Boltzmann transport equation (BTE) in highly complex geometries like the octet-truss. No prior works solve the BTE in a domain as intricate as a nanolattice, so we create a geometry representation scheme that can model any arbitrary 3-D body. Our enhanced variance-reduced Monte Carlo code incorporates this scheme, allowing us to predict the thermal conductivity of nanolattices and analyze the phonon transport behavior in them. Results suggest that hollow-beam silicon nanolattices indeed reach ultralow thermal conductivities. Based on Monte Carlo and finite element simulations, we develop a predictive thermal conductivity model that accounts for both diffusive and radiative phonon transport in nanolattices.

We also devise custom modifications to the 3ω method to experimentally measure the thermal conductivity of additively manufactured nanolattices. Since the serial fabrication process of nanolattices makes it costly to cover large areas, we design a specialized 3ω sample that minimizes the required structure size while maintaining good experimental sensitivity. We derive a new thermal model to account for conductive losses through the heater line in our novel sample geometry. 3ω measurements and compression tests of hollow-beam alumina nanolattices show that they combine ultralow thermal conductivity with excellent mechanical stiffness and resilience, which proves that nanolattices occupy a previously unreachable region in material property space. Our work provides motivation to further investigate and improve the thermal properties of architected materials.

PUBLISHED CONTENT AND CONTRIBUTIONS

1. Dou, N. G., Jagt, R. A., Portela, C. M., Greer, J. R. & Minnich, A. J. Ultralow thermal conductivity and mechanical resilience of architected nanolattices (in review).
   N. G. D. built the experiment, helped fabricate the samples, conducted the thermal measurements, developed the thermal model, analyzed the data, and wrote most of the manuscript.

2. Dou, N. G. & Minnich, A. J. Heat conduction in multifunctional nanotrusses studied using Boltzmann transport equation. *Applied Physics Letters* **108,** 011902. ISSN: 0003-6951 (Jan. 2016).
   DOI: 10.1063/1.4939266
   N. G. D. wrote the simulation code, developed improvements to the method, performed the simulations, analyzed the data, created the model, and wrote the manuscript.

TABLE OF CONTENTS

LIST OF ILLUSTRATIONS

Chapter 1

BACKGROUND AND MOTIVATION

Correlations between thermal and mechanical properties make it difficult to synthesize lightweight materials that are both thermally insulating and mechanically resilient. We can directly observe this phenomenon by examining the material property space, a multi-dimensional space of material properties in which all materials occupy a region [1]. Fig. 1.1 plots one projection of this space, showing specific modulus, or stiffness-to-density ratio, versus thermal conductivity for common materials. Fully dense solids occupy the upper right quadrant, where thermal conductivity and stiffness increase with the strength of interatomic forces. Lightweight porous solids, such as polymeric foams and aerogels, occupy the lower left quadrant where thermal conductivity and stiffness decrease precipitously with density. The void in the upper left quadrant highlights a lack of materials with ultralow thermal conductivity and high specific modulus.

Lightweight thermal insulators with high stiffness and damage tolerance would be invaluable for many aerospace applications. Aerospace vehicles operate in extreme environments that require their constituent materials to withstand large mechanical loads and sudden impacts, high and low temperatures and pressures, humidity, radiation, corrosion, and oxidation [2, 3]. The criteria for materials selection often consider density, stiffness, strength, damage tolerance, fracture toughness, fatigue, corrosion resistance, and heat resistance [4]. In some instances, no single material satisfies all of the performance requirements of a subsystem. Thermal protection systems, cryogenic storage tanks, and cryogenic feed lines require the use of multiple components made of materials that separately meet the mechanical and thermal design specifications. Additional adhesives, fasteners, or support structures often become necessary to hold parts together and accommodate thermal expansion mismatches. Structurally-integrated thermal insulation could greatly simplify such systems, thus reducing weight and cost while increasing robustness [5, 6]. We first evaluate existing thermal insulators and identify the physical mechanisms that govern their thermomechanical properties.

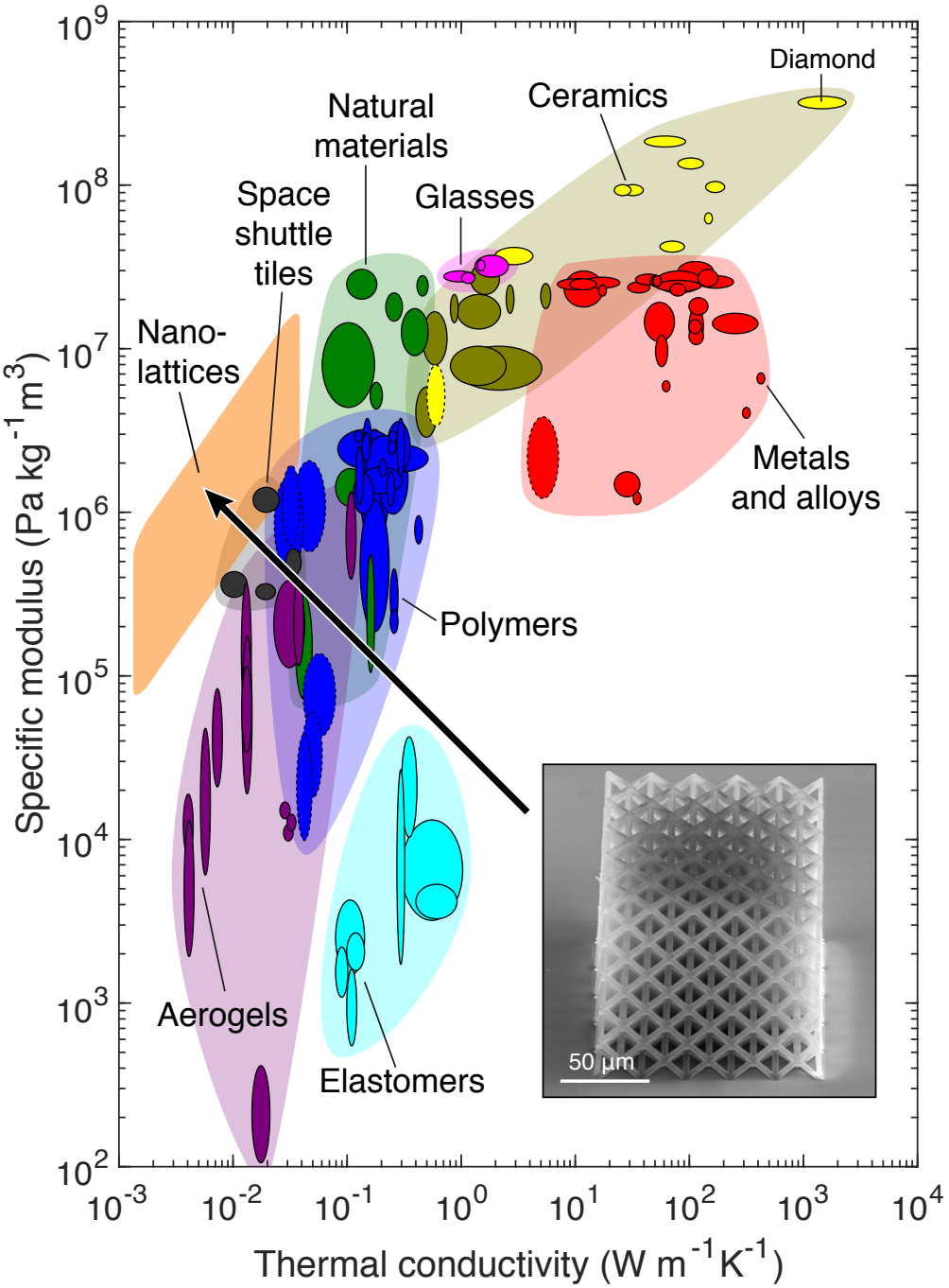

Figure 1.1: Specific modulus (stiffness-to-density ratio) versus thermal conductivity for common materials. Outlined ellipses indicate the range of properties for a particular material (i.e. diamond) and lightly shaded regions encompassing the ellipses indicate the approximate range of properties for an entire class of materials (i.e. ceramics). Dotted outlines indicate foams. Nanolattices can fill the specified region in the upper left quadrant of the material property space. The inset shows a scanning electron micrograph of a nanolattice.

1.1 Conventional porous thermal insulators

Most common thermal insulators are porous materials, also called cellular or lattice materials in the mechanics literature. Three-dimensional lattice materials frequently occur in nature as cork, wood, bone, and plant tissue. Man-made lattice materials can be created from polymers, metals, ceramics, and glasses. Cellular properties depend on intrinsic material properties of the solid material as well as structural characteristics. The cell shape and topology determine whether its mechanical behavior is bending or stretching dominated. The relative density $\bar{\rho} = \rho/\rho_s$, defined as the cellular material density ρ divided by the parent solid density ρ_s, serves as the primary parameter for the ratio of cellular-to-solid properties [7].

Pioneering works by Ashby and Gibson suggest that the properties of conventional foams are given by simple formulae. Open-cell foams deform by bending of cell edges, while closed-cell foams deform not only by cell edge bending, but also by cell face stretching and cell fluid compression [7]. Experiments and scaling arguments show that the stiffness of open-cell polymer foams scale quadratically with their relative density, $\bar{E} \propto \bar{\rho}^2$, because of their bending-dominated behavior [8]. Closed-cell foams typically exhibit the same scaling because their mass is concentrated in cell edges.

Simple physical arguments also lead to a formula for relative thermal conductivity. Assuming a vacuum environment and modest temperatures throughout the lattice, conduction, convection, and radiation through the empty spaces surrounding the lattice are negligible compared to conduction through the solid matrix phase. For a lattice composed of struts, Ashby proposes a linear $\bar{\rho}$ contribution from the struts and a $\bar{\rho}^{1.5}$ correction factor due to the nodes [1]. Other effective medium theories from Maxwell-Garnett [9], Bruggeman [10], Hashin-Shtrikman [11], and others [12–14], offer alternative models that don't capture the basic lattice structure as well as Ashby's model. Notably, these effective medium approximations for thermal conductivity depend only on relative density.

These models imply that minimizing thermal conductivity requires minimizing structural density. Up to the late 2000s, only a handful of materials could reach the ultralight regime ($\rho < 10\,\mathrm{kg\,m^{-3}}$): metallic foams, polymer foams, carbon nanotube aerogels, and silica aerogels [15, 16]. Of these, aerogels achieve the lowest densities and thermal conductivities.

Aerogels represent the state-of-the art for ultralow thermal conductivity [17], but their mechanical resilience is notoriously poor. The lightest monolithic silica

aerogels have thermal conductivity as low as $4\,\mathrm{mW\,m^{-1}\,K^{-1}}$ upon evacuation [18, 19]. These ultralight structures have a Young's modulus of 1 MPa and fail catastrophically at 20 kPa of applied flexural or tensile stress [20, 21]. The fragility of aerogels is attributed to their "pearl necklace" structure that consists of secondary particles weakly connected at narrow neck regions. Some approaches to improve the mechanical properties of silica aerogels include increasing their density, which increases the connections between secondary particles[22]; Oswald ripening or aging, where silica migrates to neck regions [23]; and polymer reinforcement by copolymerization, cogellation, or conformal coating [24–26]. The latter two methods widen the interparticle necks without substantially increasing density, thereby raising the specific compressive modulus by up to an order of magnitude. The wider necks also cause an increase in thermal conductivity, with $41\,\mathrm{mW\,m^{-1}\,K^{-1}}$ reported for polyurea-encapsulated silica aerogels [27]. The specific modulus and thermal conductivity are similarly correlated for organic and pyrolyzed carbon aerogels [28, 29]. Efforts to reduce aerogel thermal conductivity without affecting density have focused on opacification with carbon or TiO_2, which inhibits radiative heat transfer [18, 30].

Foams and aerogels both fall in the category of stochastic materials, which have random cell architectures. While the structural randomness enhances thermal resistance, particularly for aerogels, it simultaneously undermines mechanical stiffness and robustness. In contrast, ordered structures are usually more efficient and have better mechanical properties.

Inverse opals are one type of ordered cellular material with applications in photonics [31, 32], sensing [33], catalysis [34], energy storage [35], biological tissue engineering [36], and many other fields [37]. A study of silicon inverse opals reported thermal conductivities of $\sim 1\,\mathrm{W\,m^{-1}\,K^{-1}}$ [38, 39], which are significantly higher than those of aerogels and polymer foams. Mechanical studies of nickel inverse opals revealed specific strength and tunable specific modulus from 4 to $20\,\mathrm{MPa\,kg^{-1}\,m^3}$ [40]. Their architecture causes bending-dominated deformation, so the ideal stiffness scaling with relative density is quadratic, like foams. Next, we show how manipulating architecture can improve this scaling to obtain even better mechanical properties.

1.2 Architected lattices as structural thermal insulators

Architectures that satisfy Maxwell's stability criterion [41] sustain tension and compression in lattice members upon loading, so these structures are called stretching-dominated. For these architectures, stiffness scales linearly with relative density, $\bar{E} \propto \bar{\rho}$, rather than quadratically. Compared to bending-dominated lattices, stretching-dominated lattices offer higher modulus and initial yield strength for the same solid material and relative density, making them more suitable for lightweight, structural applications [1].

Developments in highly precise additive manufacturing techniques including self-propagating photopolymer waveguides (SPPW) [42], projection microstereolithography (PμSL) [43], and direct laser writing (DLW) [44, 45] have enabled the fabrication of successively smaller lattices in recent years. These lattices have exceptional mechanical properties such as high stiffness and ductile-like recoverability that originate from the size-independent structure, as well as high strength that emerges due to size effects [46]. Investigators have experimentally demonstrated that microlattices [16, 47] and nanolattices [48] can achieve the quadratic and linear relative density scalings for ideal bending- and stretching-dominated deformation.

Since the distinction between stretching- and bending-dominated architectures does not affect thermal conductivity, they should obey the same approximate scaling. This implies that architected lattices can theoretically attain much higher specific stiffnesses compared to low density foams and aerogels with the same thermal conductivity simply by employing a stretching-dominated architecture.

Furthermore, the nanoscale features of hollow-beam or core-shell nanolattices can have dimensions comparable to characteristic length scales of heat carriers. As phonons (or electrons) travel through a thin shell, increased scattering at the boundaries can lower the thermal conductivity if the shell thickness is comparable to the phonon mean free paths [49]. These classical size effects have been theorized [50, 51] and observed for thin films [52], nanowires [53, 54], and other geometries [55]. By choosing an appropriate material and wall thickness, we can leverage phonon size effects to get a reduction in thermal conductivity without further decreasing relative density.

Nanolattices hold considerable promise to satisfy the need for lightweight, stiff, and thermally insulating materials. Unlike most common materials, we can decouple their mechanical and thermal properties through their uniquely tunable architecture and structural parameters, and their potential for thermal size effects. These nano-

materials can occupy a region of property space unattainable by other fully dense or porous solids.

1.3 Thesis overview

Here, we report the methods and results of our study on nanolattice thermal properties. Since no prior work on this specific topic exists, we discuss the rationale behind our approach at every step. Chapter 2 covers our phonon transport simulations in nanolattices. We first introduce the Boltzmann transport equation (BTE) and derive its analytical solutions for thin film transport that underpin classical size effects. Then we show how a variance-reduced Monte Carlo method can solve the BTE in complex geometries while accurately capturing phonon properties of the constituent solid. We explain the computational representation of our simulation domain using a few different geometrical schemes. Finally, we present Monte Carlo simulation results for silicon nanolattices and compare them to finite element method results to isolate and model the roles of geometry and size effects. Chapter 3 covers our experimental measurements of nanolattice thermal conductivity, done using an electrothermal method called 3ω. We describe the theoretical basis of the technique, the details of our setup, and the data collection procedure. Next, we demonstrate how to adapt the 3ω sample design and thermal model to accommodate the limitations of nanolattice fabrication. Chapter 4 shows the results of our thermal conductivity measurements on polymer nanolattices, alumina nanolattices, and silicon nanolattices. We also show mechanical compression data for alumina nanolattices to evaluate their multifuncational performance. Finally, Chapter 5 summarizes key findings, explores potential directions for future study, and provides an outlook for nanoarchitected thermal materials.

Chapter 2

MONTE CARLO SIMULATIONS OF PHONON TRANSPORT

This chapter has been adapted, in part, from:

> Dou, N. G. & Minnich, A. J. Heat conduction in multifunctional nanotrusses studied using Boltzmann transport equation. *Applied Physics Letters* **108,** 011902. ISSN: 0003-6951 (Jan. 2016).

Computational simulations of heat conduction in the exact nanolattice geometry provide insight into the important transport mechanisms at play. Here, we consider only electrically insulating materials in which the primary energy carriers are phonons. Our approach will combine finite element simulations of the diffusion equation with much higher fidelity Monte Carlo simulations of the Boltzmann transport equation (BTE). First, we present analytical solutions of the BTE for bulk materials and thin films, which forms the basis of classical size effects. We describe the variance-reduced Monte Carlo method in detail and verify that it our code recovers the analytical BTE results. Then we turn our attention to the nanolattice geometry, explaining our choice of computational domain and how to computationally represent it using several geometric schemes. Finally, we discuss Monte Carlo and finite element simulation results for silicon nanolattices with the octet-truss architecture.

2.1 Boltzmann transport equation

Accurately simulating heat conduction in a nanolattice is difficult due to the wide range of length scales present in the structure. Figure 2.1 shows one example of a nanolattice composed of a periodic $5 \times 5 \times 5$ arrangement of octet-truss unit cells. The unit cell is 25 µm wide and consists of hollow beams with 2 µm radius and 121 nm wall thickness. In fact, the nanolattice fabrication process enables the construction of nanolattices with beam walls as thin as 10 nm. Size effects can occur at this length scale, meaning that thermophysical properties that typically do not vary with structure size at the macro-scale begin to change at the micro- and nano-scale. For heat conduction, the assumptions behind diffusive thermal transport break down when structural length scales approach the characteristic length scales

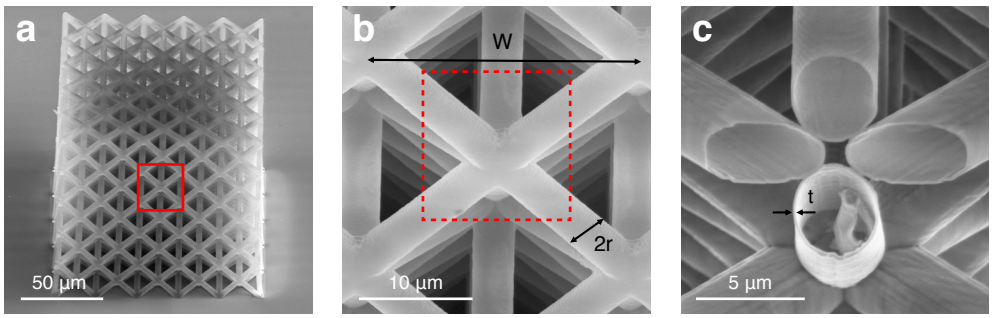

Figure 2.1: SEM images of a (a) nanolattice composed of (b) octet-truss unit cells of width $W = 25\,\mu\text{m}$ and (c) hollow beams of radius $r = 2\,\mu\text{m}$ and wall thickness $t = 121\,\text{nm}$. Panel (b) shows a magnified view of the square in panel (a) and panel (c) shows a cross-sectional view of the square in panel (b) after milling away exterior beams.

for transport of energy carriers such as phonons. To correctly simulate and model heat conduction in a nanolattice, we must consider phonon interactions with small-scale features in addition to their overall movement through large-scale features of the architected structure.

The Boltzmann transport equation governs the dynamic behavior of a phonon distribution at the mesoscale and can capture both diffusive and quasi-ballistic transport of a phonon gas. Under the relaxation time approximation, we can write the BTE as

$$\frac{\partial f}{\partial t} + \mathbf{v} \cdot \frac{\partial f}{\partial \mathbf{x}} = -\frac{f - f_0}{\tau}, \tag{2.1}$$

where f is the phonon distribution, f_0 is the equilibrium Bose-Einstein distribution

$$f_0 = \frac{1}{\exp(\hbar\omega/k_B T) - 1} \tag{2.2}$$

at the local pseudo-temperature $T(t, \mathbf{x})$, $\mathbf{v}(\mathbf{k}, s)$ is the group velocity, and $\tau(T, \mathbf{k}, s)$ is the relaxation time. The phonon distribution $f(t, \mathbf{x}, \mathbf{k}, s)$ is a time-dependent probability density function with a phase space that includes position $\mathbf{x}$, wavevector $\mathbf{k}$, and polarization s. Equivalently, we can express the phonon mode dependence in terms of frequency $\omega(\mathbf{k}, s)$ instead of wavevector, so the phonon distribution becomes $f(t, \mathbf{x}, \omega, s)$.

Using the BTE solution for a particular non-equilibrium situation, we can obtain many macroscopic quantities of interest. We demonstrate how to apply this strategy to phonon transport along a temperature gradient in a bulk solid and in a thin film.

First we show how the BTE leads to the basic constituitive equation that relates heat flux to temperature, Fourier's Law. To do this, we determine the spatially non-uniform phonon distribution caused by a steady thermal gradient and then calculate the resulting energy flux. The distribution function can be split into two parts,

$$f = f_0 + f_1, \tag{2.3}$$

where f_0 represents the local equilibrium and f_1 represents the first-order perturbation. Without loss of generality, we define x as the direction parallel to the temperature gradient. Eq. 2.2 suggests that the temperature variation causes a spatial dependence of $f_0(T(x), \omega)$ along x only, while self-similarity suggests that $f_1(\omega, s, \theta, \phi)$ has no spatial dependence at all. Since we seek a steady solution, the BTE becomes

$$v_x \frac{df_0}{dx} = -\frac{f_1}{\tau}. \tag{2.4}$$

Invoking the chain rule, we immediately obtain the perturbation distribution,

$$f_1 = -v_x \tau \frac{df_0}{dT}\frac{dT}{dx} \equiv -S_0, \tag{2.5}$$

which equals a source term S_0. Therefore, the phonon distribution is

$$f(\omega, s, \theta, \phi) = f_0 - v_\tau \frac{df_0}{dT}\frac{dT}{dx}\cos\theta, \tag{2.6}$$

where we define the polar angle θ with respect to x.

The energy flux carried by a single phonon depends on its frequency and velocity in the flux direction, $\hbar\omega v \cos\theta$. For an isotropic material, we can find the total heat flux in the x-direction by integrating the individual contributions of all phonons in frequency space and averaging over the solid angle,

$$Q_x = \int_0^{2\pi}\int_0^{\pi}\int_0^{\omega_{\max}} (\hbar\omega v \cos\theta)\, f D_\omega \, d\omega \, \frac{\sin\theta \, d\theta \, d\phi}{4\pi}, \tag{2.7}$$

where D_ω is the density of states in frequency space that accounts for degeneracy across polarizations. Inserting the distribution function, we get

$$Q_x = \int_0^{2\pi}\int_0^{\pi}\int_0^{\omega_{\max}} \frac{1}{2}\hbar\omega v \cos\theta \left(f_0 - v\tau \frac{df_0}{dT}\frac{dT}{dx}\cos\theta\right) D_\omega \, d\omega \, \frac{\sin\theta \, d\theta \, d\phi}{4\pi}. \tag{2.8}$$

If the phonon group velocities and relaxation times are isotropic, then we can evaluate the angular integrals. The heat flux expression becomes

$$Q_x = -\frac{dT}{dx}\left(\int_0^{\omega_{\max}} \frac{1}{3}\hbar\omega v^2 \tau \frac{df_0}{dT} D_\omega \, d\omega\right). \tag{2.9}$$

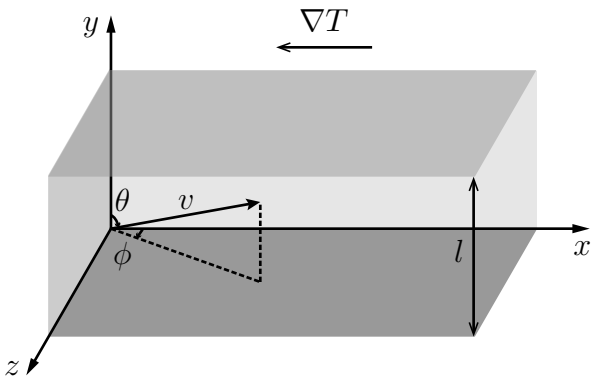

Figure 2.2: Schematic of phonon transport parallel to a thin film.

We observe that the isotropic equilibrium distribution does not contribute to the heat flux. By comparing this equation with Fourier's Law, we identify the thermal conductivity as the quantity in parentheses,

$$\kappa_{\mathrm{BTE}} = \int_0^{\omega_{\max}} \frac{1}{3} C v \lambda \, d\omega, \tag{2.10}$$

where the frequency-dependent heat capacity is

$$C = \hbar\omega \frac{df_0}{dT} D_\omega \tag{2.11}$$

and the phonon mean free path (MFP) is

$$\lambda = v\tau. \tag{2.12}$$

Eq. 2.10 is very similar to the kinetic theory result,

$$\kappa_{\mathrm{kinetic}} = \frac{1}{3} C v \lambda. \tag{2.13}$$

2.2 Classical size effects

When phonon mean free paths, or the average distances between two consecutive particle collisions, are comparable to or longer than the characteristic lengths of the propagation medium, then boundary collisions become a large source of phonon scattering. Fuchs and Sondheimer developed an accurate description of this classical size effect by solving the BTE in a thin film [50].

To derive the Fuchs-Sondheimer result for phonon transport along a thin film, we consider a temperature gradient parallel to a film of thickness l, as shown in

Figure 2.2. We again solve for the perturbation to the phonon distribution defined in Eq. 2.3. Self-similarity implies that spatial variations of f_1 can only exist along y, the direction normal to the film. In terms of $f_0(T(x), \omega)$ and $f_1(y, \omega, s, \theta, \phi)$, the BTE becomes

$$v_x \frac{df_0}{dx} + v_y \frac{df_1}{dy} = -\frac{f_1}{\tau}. \tag{2.14}$$

Rearranging, we obtain a first-order differential equation for f_1 with the same source term seen previously,

$$v_y \tau \frac{df_1}{dy} + f_1 = -v_x \tau \frac{df_0}{dT}\frac{dT}{dx} = -S_0. \tag{2.15}$$

The general solution of this problem is

$$f_1(y, \omega, s, \theta, \phi) = A \exp\left(-\frac{y}{v\tau \cos\theta}\right) - S_0(\omega, s, \theta, \phi), \tag{2.16}$$

where

$$S_0(\omega, s, \theta, \phi) = v\tau \frac{df_0}{dT}\frac{dT}{dx} \sin\theta \cos\phi. \tag{2.17}$$

Here, we define the polar angle with respect to y and the azimuthal angle with respect to x, as indicated in Figure 2.2. Now we need a boundary condition to determine the integration constant A.

The boundary condition describes how a phonon scatters when it collides with the top and bottom surfaces of the film. The phonon may reflect specularly, with the angle of reflection equal to the angle of incidence, or diffusely, with a randomized reflection direction and a thermalized equilibrium distribution. Boundary specularity is typically associated with the surface roughness compared to the phonon wavelength—a very smooth surface scatters specularly while a very rough surface scatters diffusely. We can distinguish between phonons arriving and leaving a boundary by splitting the distribution into two parts,

$$f_1 = \begin{cases} f_1^+ & \text{for} \quad 0 < \theta < \frac{\pi}{2} \\ f_1^- & \text{for} \quad \frac{\pi}{2} < \theta < \pi \end{cases}, \tag{2.18}$$

which separately govern the upward-moving and downward-moving phonons.

To specify film boundaries that scatter all phonons diffusely, we require that phonons departing from both surfaces follow the local equilibrium distribution, $f = f_0$. More precisely, the diffuse boundary conditions are

$$f_1^+ = 0 \qquad \text{on} \qquad y = 0 \tag{2.19}$$

$$f_1^- = 0 \qquad \text{on} \qquad y = l. \tag{2.20}$$

Applying these constraints to the general solution, Eq. 2.16, we get

$$f_1^+ = S_0 \left(\exp\left(-\frac{y}{v\tau \cos\theta} \right) - 1 \right) \qquad \text{for} \qquad 0 < \theta < \frac{\pi}{2} \tag{2.21}$$

$$f_1^- = S_0 \left(\exp\left(\frac{l-y}{v\tau \cos\theta} \right) - 1 \right) \qquad \text{for} \qquad \frac{\pi}{2} < \theta < \pi. \tag{2.22}$$

For convenience, we make the variable transformations $\mu = \cos\theta$ and $\eta = y/v\tau$, and define $\xi = l/v\tau$. The perturbation distributions then become

$$f_1^+ = S_0 \left(\exp\left(-\frac{\eta}{\mu} \right) - 1 \right) \qquad \text{for} \qquad 0 < \eta < 1 \tag{2.23}$$

$$f_1^- = S_0 \left(\exp\left(\frac{\xi - \eta}{\mu} \right) - 1 \right) \qquad \text{for} \qquad -1 < \theta < 0, \tag{2.24}$$

where

$$S_0 = v\tau \frac{df_0}{dT} \frac{dT}{dx} \left(1 - \mu^2 \right)^{1/2} \cos\phi. \tag{2.25}$$

With the phonon distribution in hand, we can calculate the heat flux in the x-direction by integrating the individual contribution of each phonon mode and averaging over solid angle, as in Eq. 2.7. Due to the y-dependence of the distribution, the heat flux also depends on cross-plane position within the film,

$$Q_x = \int_0^{2\pi} \int_0^{\pi} \int_0^{\omega_{\max}} \hbar\omega v_x f D_\omega \, d\omega \, \frac{\sin\theta \, d\theta \, d\phi}{4\pi}. \tag{2.26}$$

To get the average heat flux and eventually the thermal conductivity of the film, we also average over the film thickness,

$$Q_x = \int_0^{l} \int_0^{2\pi} \int_0^{\pi} \int_0^{\omega_{\max}} \hbar\omega v_x f D_\omega \, d\omega \, \frac{\sin\theta \, d\theta \, d\phi}{4\pi} \, \frac{dy}{l}. \tag{2.27}$$

Rearranging the order of integration and replacing θ and y with μ and η,

$$Q_x = \int_0^{\omega_{\max}} \hbar\omega \int_0^{2\pi} \int_{-1}^{1} v_x \int_0^{\xi} f \, \frac{d\eta}{\xi} \, \frac{d\mu \, d\phi}{4\pi} \, D_\omega \, d\omega. \tag{2.28}$$

We first find the spatially-averaged phonon distribution by averaging each part. The equilibrium distribution remains identical because it does not depend on y, so

$$\overline{f} = f_0 + \overline{f_1}, \tag{2.29}$$

where the bars denote averages over y or η. The perturbation averages are

$$\overline{f_1^+} = S_0 \int_0^{\xi} \left(\exp\left(-\frac{\eta}{\mu} \right) - 1 \right) \frac{d\eta}{\xi} \tag{2.30}$$

$$= \frac{S_0}{\xi} \left(\mu - \mu \exp\left(-\frac{\xi}{\mu} \right) - \xi \right) \tag{2.31}$$

and

$$\overline{f_1^-} = S_0 \int_0^\xi \left(\exp\left(\frac{\xi-\eta}{\mu}\right) - 1\right) \frac{d\eta}{\xi} \tag{2.32}$$

$$= \frac{S_0}{\xi}\left(-\mu + \mu \exp\left(\frac{\xi}{\mu}\right) - \xi\right). \tag{2.33}$$

Next, we simplify the average over solid angle by isolating the terms with direction dependence,

$$\int_{-1}^{1}\int_0^{2\pi} v_x \overline{f}\, \frac{d\mu\, d\phi}{4\pi} = \int_{-1}^{1}\int_0^{2\pi} v\left(f_0 + \overline{f_1}\right)\left(1-\mu^2\right)^{1/2} \cos\phi\, \frac{d\mu\, d\phi}{4\pi} \tag{2.34}$$

$$= \int_{-1}^{1}\int_0^{2\pi} v\overline{f_1}\left(1-\mu^2\right)^{1/2} \frac{d\mu}{4}\cos\phi\, \frac{d\phi}{\pi} \tag{2.35}$$

$$= v\int_{-1}^{1} v\tau \frac{df_0}{dT}\frac{dT}{dx}\left(\frac{\overline{f_1}}{S_0}\right)\left(1-\mu^2\right)\frac{d\mu}{4}\int_0^{2\pi}\cos^2\phi\, \frac{d\phi}{\pi} \tag{2.36}$$

$$= v^2\tau \frac{df_0}{dT}\frac{dT}{dx}\int_{-1}^{1}\left(\frac{\overline{f_1}}{S_0}\right)\left(1-\mu^2\right)\frac{d\mu}{4}, \tag{2.37}$$

where the equilibrium distribution again does not contribute to the flux. We can perform the integral over azimuthal angle because $\overline{f_1}/S_0$ does not depend on ϕ. We evaluate the remaining integral over μ by substituting the averaged perturbation distributions,

$$\int_{-1}^{1}\left(\frac{\overline{f_1}}{S_0}\right)\left(1-\mu^2\right)\frac{d\mu}{4} \tag{2.38}$$

$$= \int_{-1}^{0}\frac{1-\mu^2}{4}\left(\frac{\overline{f_1^-}}{S_0}\right)d\mu + \int_0^1 \frac{1-\mu^2}{4}\left(\frac{\overline{f_1^+}}{S_0}\right)d\mu \tag{2.39}$$

$$= \int_{-1}^{0}\frac{1-\mu^2}{4\xi}\left(-\mu + \mu\exp\left(\frac{\xi}{\mu}\right) - \xi\right)d\mu + \int_0^1 \frac{1-\mu^2}{4\xi}\left(\mu - \mu\exp\left(-\frac{\xi}{\mu}\right) - \xi\right)d\mu \tag{2.40}$$

$$= 2\int_0^1 \frac{1-\mu^2}{4\xi}\left(\mu - \mu\exp\left(-\frac{\xi}{\mu}\right) - \xi\right)d\mu \tag{2.41}$$

$$= \int_0^1 \left[-\frac{1-\mu^2}{2} + \frac{1}{2\xi}\left(\mu - \mu^3 - \mu\exp\left(-\frac{\xi}{\mu}\right) + \mu^3\exp\left(-\frac{\xi}{\mu}\right)\right)\right]d\mu \tag{2.42}$$

$$= -\frac{1}{3} + \frac{1}{2\xi}\left(\frac{1}{4} - \int_0^1 \mu\exp\left(-\frac{\xi}{\mu}\right)d\mu + \int_0^1 \mu^3\exp\left(-\frac{\xi}{\mu}\right)d\mu\right) \tag{2.43}$$

$$= -\frac{1}{3}\left[1 - \frac{3}{8\xi}\left(1 - 4E_3(\xi) + 4E_5(\xi)\right)\right]. \tag{2.44}$$

These equations show that the upward- and downward-moving phonons contribute equally to the flux due to symmetry. Eq. 2.44 depends on the n-th order integral exponential function, defined as

$$E_n(x) = \int_0^1 \mu^{n-2} \exp\left(-\frac{x}{\mu}\right) d\mu. \tag{2.45}$$

Back substituting the solid angle integrals, Eq. 2.44 and Eq. 2.37, into the heat flux integral, Eq. 2.28, we get

$$Q_x = -\frac{dT}{dx} \int_0^{\omega_{\max}} \frac{1}{3} K_{\mathrm{FS}}\left(\frac{l}{v\tau}\right) \hbar\omega v^2 \tau \frac{df_0}{dT} D_\omega \, d\omega, \tag{2.46}$$

so the thermal conductivity along the film is

$$\kappa_{\mathrm{FS}} = \int_0^{\omega_{\max}} \frac{1}{3} K_{\mathrm{FS}}\left(\frac{l}{\lambda}\right) C v \lambda \, d\omega. \tag{2.47}$$

The reduction factor due to classical size effects,

$$K_{\mathrm{FS},0}(\xi) = 1 - \frac{3}{8\xi}\left(1 - 4E_3(\xi) + 4E_5(\xi)\right), \tag{2.48}$$

depends on the ratio of film thickness to mean free path, known as the acoustic thickness $\xi = l/\lambda$ [57], whose inverse equals the phonon Knudsen number, $\mathrm{Kn} = \lambda/l$.

In contrast to diffusely-scattering boundaries, specularly-scattering boundaries reflect phonons in a mirror-like fashion. A scattered phonon's momentum normal to the surface reverses while its momentum parallel to the surface remains unchanged. The boundary conditions for a film with specular surfaces,

$$f_1^+(\mu, \dots) = f_1^-(-\mu, \dots) \qquad \text{on} \qquad y = 0 \tag{2.49}$$

$$f_1^+(\mu, \dots) = f_1^-(-\mu, \dots) \qquad \text{on} \qquad y = l, \tag{2.50}$$

imposes a symmetry constraint on the distribution function, which reflects the phonon scattering behavior. The thermal conductivity along the film equals its bulk thermal conductivity in this case, because surface scattering does not affect the in-plane transport of phonons.

More generally, we can model a boundary at which a fraction of phonons, p, scatter specularly and the rest of the phonons, $1 - p$, scatter diffusely. For a thin film with specularity parameter p, the in-plane thermal conductivity is reduced by

$$K_{\mathrm{FS},p}(\xi) = 1 - \frac{3}{2\xi}(1-p) \int_0^1 \left(\mu - \mu^3\right) \frac{1 - \exp(-\xi/\mu)}{1 - p\exp(-\xi/\mu)} \, d\mu. \tag{2.51}$$

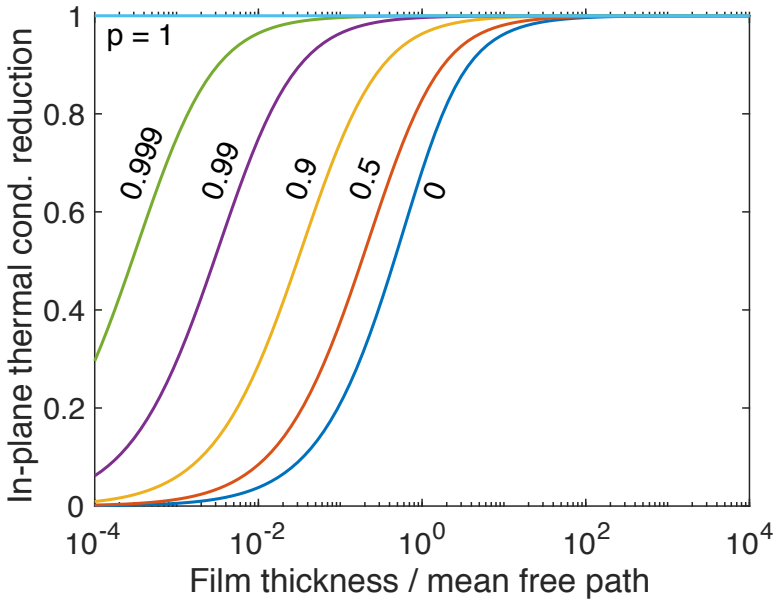

Figure 2.3: Fuchs-Sondheimer reduction of in-plane thermal conductivity contribution for a phonon mode with mean free path λ in a thin film with thickness l and specularity parameter p, given by Eq. 2.51. The horizontal axis represents l/λ and the curve labels indicate p.

In the fully specular limit, $p = 1$ and $K_{\mathrm{FS},1} = 1$, indicating no thermal conductivity reduction, as expected. In the fully diffuse limit, $p = 0$ and Eq. 2.51 becomes equivalent to Eq. 2.48. Figure 2.3 plots $K_{\mathrm{FS},p}(\xi)$ for several values of p. For partially diffuse boundaries $p < 1$, the contribution of a phonon mode with mean free path λ to in-plane thermal conductivity equals the bulk value for acoustically-thick films, decreases for films with thickness comparable to the MFP, and approaches zero for acoustically-thin films. We can alternatively say that long MFP phonons experience a greater reduction in their contribution to thermal conductivity than short MFP phonons for a given film thickness l.

2.3 Monte Carlo algorithm

The complexity of nanolattice geometries precludes any analytical solutions of the Boltzmann transport equation. Even numerical methods incur high computational costs because the phonon distribution has such a high dimensionality and because phonon modes interact nonlinearly. Solving the BTE deterministically quickly becomes intractable for complex domains, but stochastic methods lend themselves well to these types of problems. Borrowing from direct-simulation Monte Carlo methods for rarefied gas dynamics, Peterson [58] introduced the first Monte Carlo

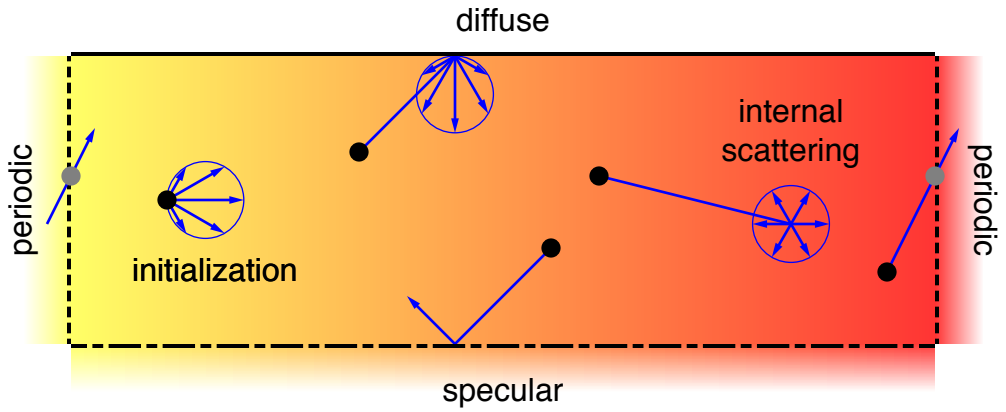

Figure 2.4: Schematic of the Monte Carlo algorithm used to solve the Boltzmann transport equation, illustrating particle initialization, advection, and scattering in a domain with diffuse, specular, and periodic boundaries.

(MC) method for phonon transport, which was improved by Mazumder and Majumdar [59]. Further developments enabled the inclusion of frequency-dependent mean free paths [60], transmission and reflection at interfaces [61], and periodic boundary conditions that facilitate simulations of periodic structure [62].

In our study, we employ an efficient variance-reduced Monte Carlo method developed by Péraud et al. [63, 64], which solves the deviational energy formulation of the BTE,

$$\frac{\partial g_1}{\partial t} + \mathbf{v} \cdot \frac{\partial g_1}{\partial \mathbf{x}} = -\frac{g_1 - \left(g_0 - g_{0,\mathrm{ref}}\right)}{\tau} - \mathbf{v} \cdot \frac{\partial g_{0,\mathrm{ref}}}{\partial \mathbf{x}}, \tag{2.52}$$

where the distributions defined as

$$g_{0,\mathrm{ref}} = \hbar\omega f_{0,\mathrm{ref}} \tag{2.53a}$$

$$g_0 = \hbar\omega f_0 \tag{2.53b}$$

$$g_1 = \hbar\omega \left(f - f_{0,\mathrm{ref}}\right), \tag{2.53c}$$

represent a time-invariant reference equilibrium distribution based on a reference temperature field $T_{\mathrm{ref}}(\mathbf{x})$, a local equilibrium distribution based the local pseudo-temperature $T_0(\mathbf{x})$ [62], and the unknown deviation from the reference equilibrium. All other symbols correspond to those found in the normal BTE formulation, Eq. 2.1. If all temperature fluctuations in the system are small with respect to a globally averaged reference temperature, $|T_0(\mathbf{x}) - T_{\mathrm{avg}}| \ll T_{\mathrm{avg}}$ and $|T_{\mathrm{ref}}(\mathbf{x}) - T_{\mathrm{avg}}| \ll T_{\mathrm{avg}}$,

then we can linearize Eq. 2.52 as

$$\frac{\partial g_1}{\partial t} + \mathbf{v} \cdot \frac{\partial g_1}{\partial \mathbf{x}} = -\frac{1}{\tau}\left(g_1 - (T_0 - T_{\text{ref}})\,\frac{dg_{0,\text{avg}}}{dT}\right) - \mathbf{v} \cdot \frac{\partial T_{\text{ref}}}{\partial \mathbf{x}}\frac{dg_{0,\text{avg}}}{dT}, \tag{2.54}$$

where $g_{0,\text{avg}}$ is the equilibrium distribution at T_{avg}. This average temperature is spatially and temporally constant, and is the temperature at which we evaluate phonon transport properties. Upon linearization, computational particles become completely independent from one another because their transport only relies on the pre-determined average temperature and reference profile. This variance-reduced algorithm is around 10^6 times faster than other MC methods for the nanolattice problem considered here, and enables simulations of thermal transport in large and complex structures.

The Monte Carlo algorithm computes the deviational energy distribution by stochastically simulating the trajectory of phonon bundles that each carry a fixed amount of energy. Each of these particles has a sign $\delta_\pm$, frequency ω, polarization s, position $\mathbf{x}$, and direction $\mathbf{u}(\theta, \phi)$, which are initialized based on the reference temperature distribution. The algorithm updates these properties and state variables as the particle advects and scatters through the domain according to its transport properties, the known equilibrium that dominates the distribution, and prescribed boundary conditions. The particle is terminated when the number of scattering events reaches a specified maximum. The algorithm calculates averaged temperature and heat flux fields using particle effective power, grid cell volume, and cumulative elapsed time and displacement of particle trajectories in each grid cell. We further describe the key algorithm details here, focusing mainly on the simulation mechanics rather than the theoretical basis of the technique.

We first discuss the process of sampling distributions—a fundamental concept for any stochastic numerical method. Sampling relies on a uniform random number generator (RNG) that outputs $r \in [0, 1)$. We refer to these RNG outputs as "random numbers" for the remainder of this section. Given a probability density function (PDF), $\psi(x)$, for a variable $x_{\min} < x < x_{\max}$, we sample from the distribution by setting the cumulative distribution function (CDF), $\Psi(x)$, equal to a random number. This amounts to solving

$$r = \Psi(x) = \frac{\int_{x_{\min}}^{x} \psi(x')\,dx'}{\int_{x_{\min}}^{x_{\max}} \psi(x')\,dx'}, \tag{2.55}$$

for the sample value x, where the denominator normalizes the distribution. If the independent variable is discrete instead of continuous, $x \in \{x_1 \ldots x_N\}$, then we

need the corresponding discrete probabilities, $\{p_1 \dots p_N\}$. We define the partial sum of probabilities as

$$P_n = \frac{\sum_{i=1}^{n} p_i}{\sum_{i=1}^{N} p_i} \tag{2.56}$$

so the sampling procedure involves searching for the index n such that

$$P_{n-1} \leq r < P_n, \tag{2.57}$$

where $P_0 = 0$, and the sample value is x_n. Finally, we can discretize a continuous variable x with a known $\psi(x)$ by setting the probably of a discrete x_i equal to $p_i = \psi(x_i)\Delta x_i$, where Δx_i is the potentially non-uniform step size between x values.

Three important distributions appear in this Monte Carlo method, which we call the energy distribution,

$$\psi_E = \frac{dg_{0,\text{avg}}}{dT} D_{\omega s}, \tag{2.58}$$

the flux distribution,

$$\psi_Q = v \cos\theta \frac{dg_{0,\text{avg}}}{dT} D_{\omega s}, \tag{2.59}$$

and the scattering distribution,

$$\psi_{\text{scat}} = \frac{1}{\tau} \frac{dg_{0,\text{avg}}}{dT} D_{\omega s}, \tag{2.60}$$

in which the density of states $D_{\omega s}$, group velocities $v(\omega, s)$, and relaxation times $\tau(\omega, s)$ depend on frequency and polarization. These expressions represent the relative contributions of particles to each of the corresponding physical quantities. They all depend on the temperature derivative of the Bose-Einstein distribution evaluated at the average reference temperature,

$$\frac{dg_{0,\text{avg}}}{dT} = k_B \left(\frac{\hbar\omega / 2k_B T_{\text{avg}}}{\sinh\left(\hbar\omega / 2k_B T_{\text{avg}}\right)} \right)^2, \tag{2.61}$$

which approaches

$$\frac{dg_{0,\text{avg}}}{dT} = k_B \left(1 - \frac{1}{12} \left(\frac{\hbar\omega}{k_B T_{\text{avg}}} \right)^2 \right) \tag{2.62}$$

for very low frequencies $\hbar\omega \ll k_B T_{\text{avg}}$.

To sample phonon properties, we draw from one of these particle distributions $\psi(\omega, s, \theta, \phi)$ that depend on frequency $0 < \omega < \omega_{\max}$, polarization $s \in \{1 \dots s_{\max}\}$, polar angle $0 < \theta < \pi$, and azimuthal angle $0 < \phi < 2\pi$. We discretize frequency as $\omega \in \{\omega_1 \dots \omega_N\}$ for convenience. Since the probability densities all have the form

$\psi(\omega, s, \theta, \phi) = \psi_{\omega s}(\omega, s)\psi_\theta(\theta)\psi_\phi(\phi)$, these sets of random variables are independent and we can draw them separately. We first draw the frequency by summing over polarizations to get their total probabilities

$$p(\omega_i) = \sum_s \psi_{\omega s}(\omega_i, s)\Delta\omega_i \tag{2.63}$$

and sampling based on Eq. 2.56 and 2.57. We then draw the polarization based on the selected frequency ω_n using the conditional probabilities

$$p(s \mid \omega_n) = \psi_{\omega s}(\omega_n, s)\Delta\omega_n. \tag{2.64}$$

Calculating the selection probability for polar and azimuthal angles involves an integral over solid angle, $\sin\theta\, d\theta\, d\phi$, which implies that the polar angle CDF for the isotropic energy and scattering distributions is

$$\Psi_{\text{iso},\theta} = \frac{\int_0^\theta \sin\theta'\, d\theta'}{\int_0^\pi \sin\theta'\, d\theta'} = \frac{1-\cos\theta}{2}. \tag{2.65}$$

Setting this equal to a random number, we find that the cosine of the sampled polar angle is uniformly distributed between 1 and -1, calculated as $\cos\theta = 1-2r$. For the anisotropic flux distribution, the polar angle has a restricted domain, $0 < \theta < \pi/2$, and its CDF is

$$\Psi_{\text{aniso},\theta} = \frac{\int_0^\theta \cos\theta' \sin\theta'\, d\theta'}{\int_0^{\pi/2} \cos\theta' \sin\theta'\, d\theta'} = \sin^2\theta. \tag{2.66}$$

The polar angle cosine thus becomes $\cos\theta = \sqrt{1-r}$. Finally, the azimuthal angle is isotropic in all cases, so we find that its CDF is linear, $\Psi_\phi = \phi/2\pi$, and the sampled value is just $\phi = 2\pi r$.

Boundary conditions also play a critical role in every step of the algorithm. Our code implements three types of adiabatic boundary conditions that represent diffuse, specular, and partially-specular surfaces, in addition to isothermal and periodic boundary conditions. We also include an interface boundary condition to split a domain into subdomains. Each type of boundary affects particle transport differently in simulations. Isothermal and periodic surfaces emit particles, adiabatic surfaces reflect particles, interfacial and periodic surfaces transmit particles, and isothermal surfaces absorb particles.

Particle initialization can occur either on the domain boundary due to imposed temperatures, or in the domain volume due to reference temperature gradients. We

refer to these as surface or volume sources, respectively. The average heat generated by a surface source with an enforced temperature difference ΔT_{bc} is

$$Q_{\text{surf}} = A \sum_s \int_0^{2\pi} \int_0^{\pi/2} \int_0^{\omega_{\max}} v \cos\theta \left(\Delta g_{0,\text{bc}}\right) D_{\omega s} \, d\omega \, \frac{\sin\theta \, d\theta \, d\phi}{4\pi} \tag{2.67}$$

$$= A \Delta T_{\text{bc}} \left(\frac{1}{4} \sum_{\omega,s} v \frac{dg_{0,\text{avg}}}{dT} D_{\omega s} \, \Delta\omega \right), \tag{2.68}$$

so the relative number of particles emitted by a surface source is proportional to

$$p_{\text{surf}} = A \left| \Delta T_{\text{bc}} \right|, \tag{2.69}$$

where we assume the boundary condition temperature ΔT_{bc} is constant across the surface. As suggested by rightmost term in the linearized BTE, Eq. 2.54, the heat generated by a volume source with a gradient in the reference temperature $\partial T_{\text{ref}} / \partial \mathbf{x}$ is

$$Q_{\text{vol}} = A \sum_s \int_0^{2\pi} \int_0^{\pi/2} \int_0^{\omega_{\max}} v \cos\theta \left(\Delta g_{0,\text{ref}}\right) D_{\omega s} \, d\omega \, \frac{\sin\theta \, d\theta \, d\phi}{4\pi}$$

$$- A \sum_s \int_0^{2\pi} \int_{\pi/2}^{\pi} \int_0^{\omega_{\max}} v \cos\theta \left(\Delta g_{0,\text{ref}}\right) D_{\omega s} \, d\omega \, \frac{\sin\theta \, d\theta \, d\phi}{4\pi} \tag{2.70}$$

$$= 2V \left| \frac{\partial T_{\text{ref}}}{\partial \mathbf{x}} \right| \left(\frac{1}{4} \sum_{\omega,s} v \frac{dg_{0,\text{avg}}}{dT} D_{\omega s} \, \Delta\omega \right), \tag{2.71}$$

so the relative number of emitted particles is proportional to

$$p_{\text{vol}} = 2V \left| \frac{\partial T_{\text{ref}}}{\partial \mathbf{x}} \right|, \tag{2.72}$$

where we assume that the reference temperature gradient is constant throughout the volume. The factor of 2 accounts for volumetric generation of particles in any direction compared to the half space available for surface generation. Given a set of particle sources, we can either select from the sources using the same process as drawing from a discrete distribution, or predetermine the number of particles to emit from each source based on the total number of particles. The effective amount of heat or power carried by each particle equals

$$Q_{\text{eff}} = \frac{1}{N_{\text{emit}}} \sum Q_{\text{src}}, \tag{2.73}$$

which is just the total heat generation given by Eqs. 2.69 or 2.72 divided by the total number of emitted particles.

After deciding the particle emission source, we draw a random position inside that source as the particle's initial position. For example, we obtain a random point in a parallelogram via

$$\mathbf{x}_0 = \mathbf{o} + r_1\mathbf{a}_1 + r_2\mathbf{a}_2, \tag{2.74}$$

where $\mathbf{o}$ specifies the coordinates of a vertex designated as the origin, $\mathbf{a}_1$ and $\mathbf{a}_2$ represent the relative positions of the two neighboring vertices with respect to the origin, and r_1 and r_2 are two random numbers. Likewise, we obtain a random point in a parallelepiped via

$$\mathbf{x}_0 = \mathbf{o} + r_1\mathbf{a}_1 + r_2\mathbf{a}_2 + r_3\mathbf{a}_3, \tag{2.75}$$

where we have one additional neighboring vertex and random number. These simple routines extend to triangles and tetrahedra by reflecting exterior points to the interior. Eq. 2.74 applies to triangles if we transform $r_1 \leftarrow (1 - r_1)$ and $r_2 \leftarrow (1 - r_2)$ when $r_1 + r_2 > 1$. For an arbitrary source geometry with an indicator function that tests domain membership and a bounding box that fully encloses it, we can obtain a random point by choosing points from the bounding box until we get a point inside the source domain. The efficiency of this procedure directly depends on the relative size of the source compared to the bounding box. Note that the area and volume in Eqs. 2.69 and 2.72 refer to the size of the source rather than the bounding box in this scenario. To avoid rejecting point selections, we instead divide sources with complex geometries into multiple sources with simple geometries.

Initial particle properties come from sampling the flux distribution, Eq. 2.59, which provides the frequency, polarization, and direction of motion. The polar angle is defined with respect to the gradient direction for a volume source or the surface normal for a surface source. The particle sign, $\delta_\pm \in \{-1, 1\}$, indicates whether the particle carries positive or negative deviational energy, allowing the algorithm to compute both positive and negative perturbations to the reference equilibrium state. For a volume source, we draw an additional random number to determine the sign with 50-50 probability. We align the $\theta = 0$ direction down the temperature gradient for positive particles, and up the temperature gradient for negative particles, such that

$$\delta_{\pm,\mathrm{vol}} = \mathrm{sign}\left(-\mathbf{v}_0 \cdot \frac{\partial T_{\mathrm{ref}}}{\partial \mathbf{x}}\right). \tag{2.76}$$

The sign of a particle emitted from a surface source corresponds to whether the source temperature is positive or negative,

$$\delta_{\pm,\mathrm{surf}} = \mathrm{sign}\left(\Delta T_{\mathrm{bc}}\right). \tag{2.77}$$

The source temperature for an isothermal boundary equals

$$\Delta T_{\text{bc,isot}} = T_{\text{surf}} - T_{\text{ref}}, \tag{2.78}$$

while the source temperature for a periodic boundary equals

$$\Delta T_{\text{bc,peri}} = \left(T_{\text{surf}} - T_{\text{ref,surf}}\right) - \left(T_{\text{pair}} - T_{\text{ref,pair}}\right), \tag{2.79}$$

where we take the temperature deviations of the surface and its periodic pair from their local reference temperatures and subtract them. The source temperature of the paired surface will have an equal magnitude but opposite sign.

Each particle also stores the distance to its next internal scattering event, which we randomly sample according to its relaxation time τ. Specifically, we draw the scattering time t_0 from the exponential distribution, $\psi_{t_0} = \exp(-t_0/\tau)$, by solving $r = \Psi_{t_0} = 1 - \exp(-t_0/\tau)$. Since r and $(1-r)$ are both uniformly distributed between 0 and 1, we can set

$$d_0 = v t_0 = -v\tau \log(r) \tag{2.80}$$

as the internal scattering distance, where $v(\omega, s)$ is the group velocity.

Particles in this Monte Carlo method do not interact, so the algorithm simulates each phonon trajectory independently. During the advection step, a particle moves directly to its next collision position, which occurs either in the domain or on the domain boundary. If the nearest boundary is further than the pre-determined internal scattering distance, then the particle advances $d_{\text{min}} = d_0$ along the trajectory to the internal scattering location. Otherwise, the particle advances to the boundary, $d_{\text{min}} = d_{\text{bdry}}$. The internal scattering distance decreases by the actual distance that the particle moved, $d_0 \leftarrow (d_0 - d_{\text{min}})$. We further discuss the calculation of boundary distances in Section 2.6.

Before proceeding with the trajectory simulation, the algorithm computes the contribution of the trajectory segment to macroscopic transport quantities. To compute average temperature and heat flux, we accumulate the displacement and elapsed time of particles inside specified measurement regions. These regions are often grid cells of equal size and spacing, so we refer to them as cells, but the following general procedure applies to any region of interest. By finding the intersections of the particle trajectory,

$$\mathbf{x} = \mathbf{x}_i + \xi \Delta \mathbf{x}_i \tag{2.81}$$

for $0 < \xi < 1$, with the cell boundaries, we calculate the fraction of the trajectory segment that lies inside the cell, $\Delta\xi_{\text{cell}}$. Then we add the particle's contribution to the cumulative displacement, $\Delta\mathbf{x}_{\text{cell}} \leftarrow \Delta\mathbf{x}_{\text{cell}} + \delta_{\pm}\Delta\xi_{\text{cell}}\Delta\mathbf{x}_i$, and the cumulative elapsed time, $\Delta t_{\text{cell}} \leftarrow \Delta t_{\text{cell}} + \delta_{\pm}\Delta\xi_{\text{cell}}\Delta t_i$, with consideration for the particle's sign.

Next, the algorithm executes the internal scattering or boundary scattering routines. For internal scattering, the particle relaxes to the local scattering distribution ψ_{scat}, so we redraw the particle direction and properties from Eq. 2.60. For scattering at an adiabatic boundary, the particle properties remain unchanged but the particle direction reflects back towards the domain interior in a manner that depends on the boundary specularity. A specular scattering event maintains the particle momentum parallel to the surface but reverses the particle momentum normal to the surface,

$$\mathbf{u}_{i+1} = \mathbf{u}_i - 2\left(\mathbf{u}_i \cdot \mathbf{n}\right)\mathbf{n}, \tag{2.82}$$

where $\mathbf{n}$ is the boundary normal pointing into the domain. A fully diffuse scattering event randomizes the particle direction in the half-space defined by the boundary plane. Since the flux of departing particles must equal the flux of arriving particles, we draw the particle direction from the anisotropic distribution $\psi_{\text{aniso},\theta}\psi_{\phi}$. The polar angle selected from Eq. 2.66 is defined with respect to $\mathbf{n}$. For partially specular boundaries, we draw a random number and compare it to the specularity parameter $p_{\text{spec}}(\omega, s)$. If $r < p_{\text{spec}}$, then the particle scatters specularly, otherwise it scatters diffusely.

Collisions with non-adiabatic boundaries do not necessarily result in particle scattering, but we still enforce their boundary conditions during the scattering step. For a periodic boundary pair, we use the invertible linear transformation that patterns the simulation domain through space, which always includes translation and sometimes includes rotation. When a particle hits a periodic boundary, we map its position and direction to the paired boundary with the same transformation. In general, the particle position translates and rotates about the origin, while the particle direction only rotates. An isothermal boundary behaves like a black body that absorbs all incident particles. We implement absorption by terminating the particle, which we discuss next. Finally, the interface boundary condition we implement only serves to split a complex domain into simpler subdomains, as described in Section 2.6, rather than representing grain boundaries or material interfaces. Therefore, none of the particle attributes change upon colliding with these interface boundaries.

Together, the advection, accumulation, and scattering steps represent a full iteration of the algorithm's main loop. The trajectory calculation continues until the algorithm detects one of the following termination conditions. First, the loop breaks if an isothermal boundary absorbs the particle. Second, we increment a counter and the loop breaks if we find that the particle escaped the domain. This happens infrequently, likely because of numerical errors at boundaries and corners. We implement a surface tolerance to reduce the probability of particle escape, which allows a boundary to interact with particles in a thin region that extends outward from the domain. Lastly, the loop breaks if the particle exceeds a specified number of randomizing scattering events, N_{scat}. The two types of randomized scattering in our implementation are internal scattering and diffuse scattering. The particle's averaged contribution to temperature and heat flux reaches a plateau after it fully explores the domain and loses "memory" of its source due to direction and property randomization. Beyond that point, the particle will add more statistical noise than useful signal, so it becomes counterproductive to continue the trajectory simulation. We determine N_{scat} empirically by accumulating elapsed times and displacements as a function of randomizing scattering events since initialization, n_{scat}.

The algorithm's outer loop repeats the trajectory simulation for all N_{emit} particles. At the end, we obtain the average heat flux,

$$\overline{\mathbf{Q}''_{\text{cell}}} = \frac{Q_{\text{eff}} \Delta \mathbf{x}_{\text{cell}}}{V_{\text{cell}}} \tag{2.83}$$

and average temperature deviation

$$\overline{T_{\text{cell}} - T_{\text{ref}}} = \frac{Q_{\text{eff}} \Delta t_{\text{cell}}}{C V_{\text{cell}}} \tag{2.84}$$

based on the cumulative elapsed time and displacement in each grid cell, along with the solid volume inside the cell V_{cell}, the effective particle power Q_{eff} given by Eq. 2.73, and the volumetric heat capacity,

$$C = \sum_{\omega,s} \frac{dg_{0,\text{avg}}}{dT} D_{\omega s} \, \Delta\omega. \tag{2.85}$$

2.4 Monte Carlo validation

Before using our Monte Carlo code to simulate nanolattices, we verify its correctness by simulating simple problems with known solutions. Here, we show that our Boltzmann Transport Equation solver gives numerical results that converge to analytical results derived in the previous sections. We compute macroscopic quantities such as temperature profiles, heat flux profiles, and thermal conductivity for bulk transport and thin-film transport of phonons.

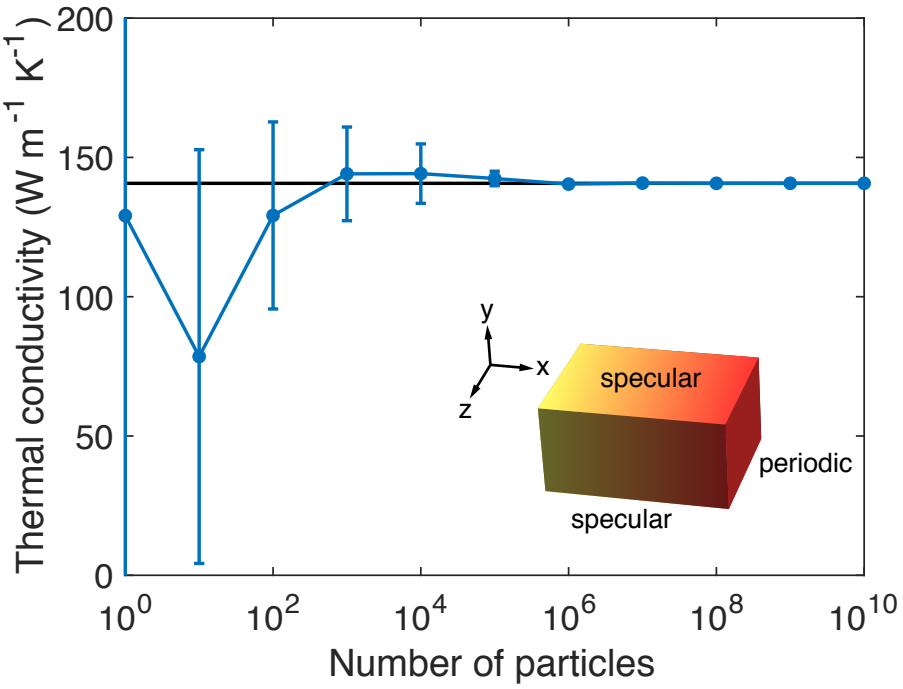

Figure 2.5: Linear temperature profile in bulk silicon with a constant temperature gradient. The thermal conductivity calculated from the average heat flux is consistent with the expected room temperature value, 148 $\mathrm{W\,m^{-1}\,K^{-1}}$.

A bulk simulation domain extends to infinity in all spatial directions, but we contain particles within a smaller region to avoid numerical overflow of the position coordinates. We mimic an infinite domain using a box with periodic boundaries along the temperature gradient direction and specular boundaries for all other faces, as shown in the inset of Figure 2.5. Similar to the optical illusion created by a pair of parallel mirrors, the two pairs of specular boundaries imitate an alternating sequence of the domain and its mirror image. The invariance of the solid box and the temperature gradient upon reflection across the lateral faces means that the specular boundary conditions capture the infinite extent of the domain in the lateral directions. Likewise, periodic boundary conditions provide a natural way to simulate the infinite extent of the domain in the transport direction. We could achieve the same goal with three pairs of periodic boundaries, but not with three pairs of specular boundaries, because the mirror image of the domain along the transport direction would have a reversed temperature gradient.

By repeating the bulk simulation several times with an increasing number of

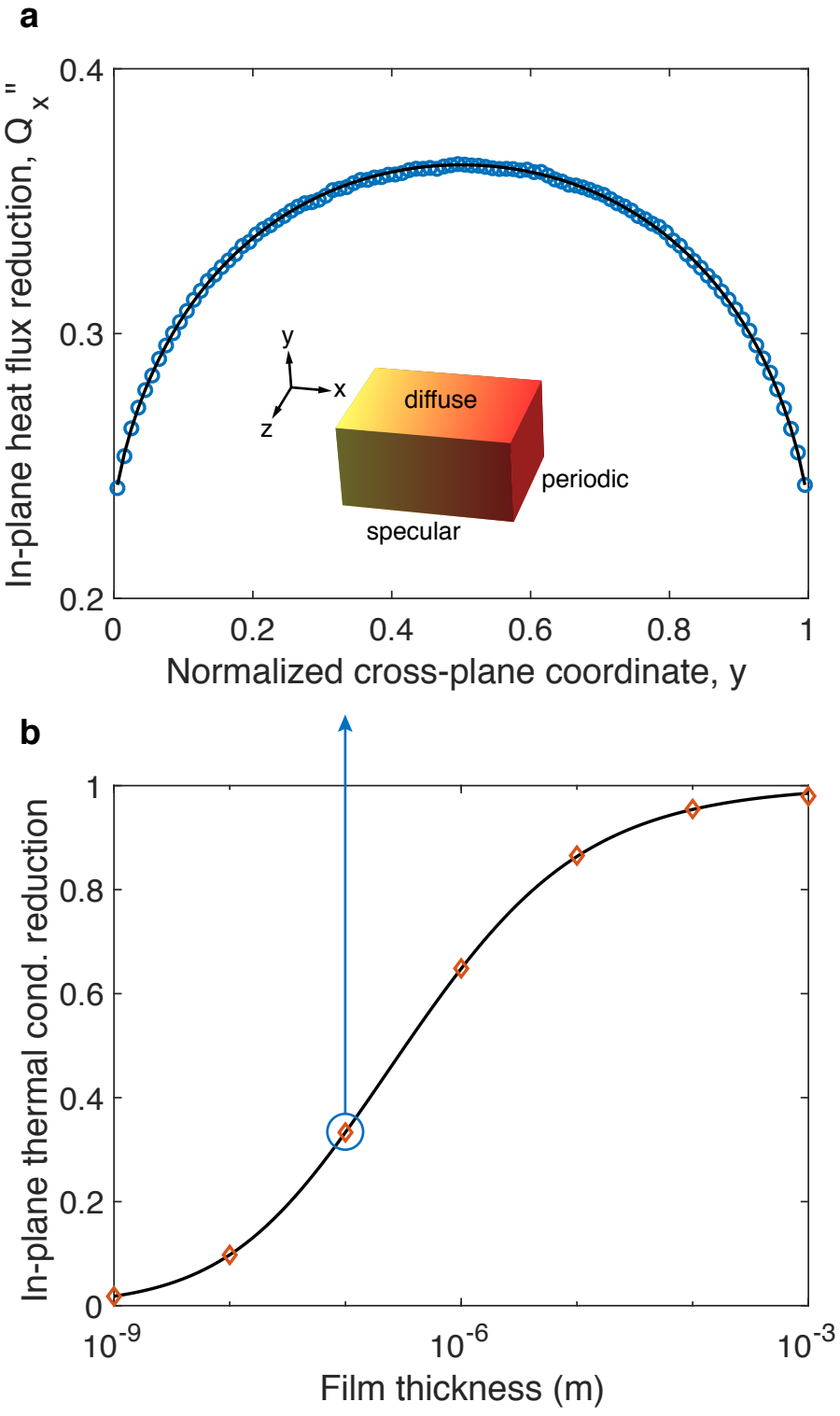

Figure 2.6: Heat flux profile across a 10 µm-thin silicon film with a temperature gradient along the film. The reduction of heat flux near the diffusely-scattering surfaces matches the analytical Fuchs-Sondheimer curve.

particles, we can observe the convergence of thermal conductivity. We use phonon properties of silicon at room temperature [65] and confirm that the simulated thermal conductivity approaches the analytically determined value from Eq. 2.10. The BTE agrees with the heat equation in this diffusive transport regime, so we recover the expected bulk thermal conductivity of silicon, $\kappa = 148\,\mathrm{W\,m^{-1}\,K^{-1}}$. This test case proves that we can correctly simulate phonon transport in the diffusive limit—a simple but important verification step.

Next, we consider phonon transport along a thin film with diffusely-scattering surfaces. We represent the film using a box with periodic boundaries along the temperature gradient direction, specular boundaries along the transverse in-plane direction, and diffuse boundaries for the physical surfaces of the film, as shown in the inset of Figure 2.6a. As in the bulk case, the periodic and specular boundary pairs allow us to simulate a domain with infinite extent in two directions. The distance between the two diffuse boundaries is the film thickness, while the other two dimensions of the box are arbitrary.

We confirm that the algorithm accurately captures classical size effects by computing the effect of diffuse scattering on phonon transport along the film. Figure 2.6a plots the in-plane heat flux as a function of cross-plane position, showing that the influence of "wall drag" decays into the film. The simulated data are consistent with the theoretical Fuchs-Sondheimer curve obtained by numerically integrating Eq. 2.26. Repeating this simulation for several film thicknesses from 1 nm to 1 mm, we calculate the average in-plane thermal conductivity reduction and confirm that it matches Eq. 2.48, as shown in Figure 2.6b.

If we replace the diffuse boundaries of the film domain with specular boundaries, then we notice that the simulation domain becomes identical to the bulk domain. Therefore, we can immediately conclude that transport along a film with specularly-reflecting surfaces is equivalent to bulk transport. The heat flux does not have spatial variations and the thermal conductivity equals the bulk value, as predicted by theory. This thin film test case demonstrates that our Monte Carlo code correctly simulates phonon transport in the classical size effects regime.

2.5 Octet-truss architecture

To numerically compute the effective thermal conductivity of a nanolattice, we impose a fixed temperature difference across the structure, calculate the steady-state heat flux, and deduce the thermal conductivity from Fourier's Law. The periodicity

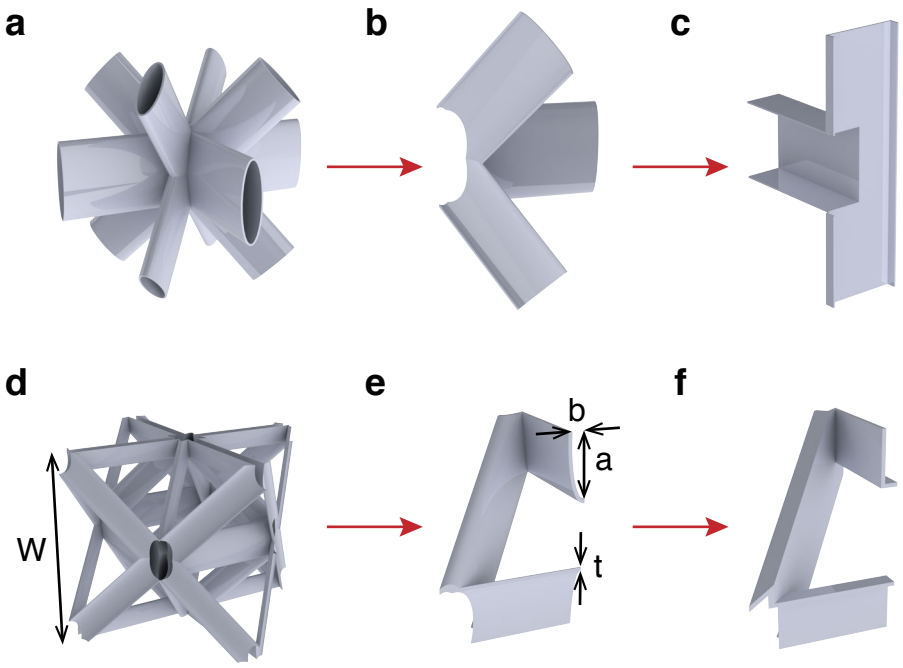

Figure 2.7: Geometry simplification for an octet-truss nanolattice. (a) Primitive unit cell, simplified into a (b) primitive representative subunit, and transformed into a (c) primitive polyhedron subunit. (d) Conventional unit cell, simplified into a (e) conventional representative subunit, and transformed into a (f) conventional polyhedron subunit. Simulations reported here use the domains shown in panels (e) and (f). The lattice dimensions that parameterize the octet-truss geometry are the unit cell size W, major axis a, minor axis b, and wall thickness t.

and symmetry of a nanolattice allow us to greatly simplify the simulation domain, but we must ensure that the transformed problem gives the same solution as the original problem.

One can conceive of many representative volume elements for the octet-truss architecture, but not all geometries facilitate convenient simulation of heat conduction or even possess identical effective properties. A suitable simulation geometry must satisfy several criteria. At minimum, it must have a space-filling bounding volume whose topology matches the octet-truss when tessellated. In addition, we must have *a priori* knowledge of the boundary conditions on the surface of the bounding volume. We consider two possible routes for geometry simplification, starting with the primitive and conventional cells shown in Figure 2.7a and d.

The primitive Wigner-Seitz cell has the advantage of containing only a single node. The bounding volume of the primitive cell is a rhombic dodecahedron,

which fills space when patterned in a face-centered-cubic lattice. We can simplify the star-like geometry by considering rotation and reflection symmetries and converting curved faces into flat faces, as illustrated by Figure 2.7b and c. The transformation from the representative subunit in panel b to the polyhedron subunit in panel c changes the beam angles, making it easier to model, but harder to define a transformed bounding volume. If we assume that the bounding volume becomes a rectangular prism, we find that each node only connects to four other nodes ($Z = 4$) whereas the nodal connectivity of the octet-truss architecture is twelve ($Z = 12$). We clearly cannot use the primitive polyhedron subunit as a representative geometry. The primitive representative subunit remains viable based on topological considerations, but other factors preclude its use as our simulation domain.

Assignment of boundary conditions becomes problematic when simulating any geometry derived from the primitive cell. We need to establish an effective temperature difference in the direction that we want to determine thermal conductivity, but none of the bounding volume faces align with the Cartesian directions of interest. Even if we wanted to calculate the thermal conductivity in a diagonal direction, we do not know the temperatures or heat fluxes at the beam ends that are not aligned with the overall transport direction. Therefore, we turn to the conventional cell.

The conventional cell has a cubic bounding volume that fills space when patterned in a simple-cubic lattice, making it straightforward to impose an effective temperature difference along any Cartesian direction. All faces that intersect the bounding volume with surface normal parallel to the transport direction must be isothermal. All other faces that intersect the bounding volume have surface normals perpendicular to the transport direction and must be adiabatic by symmetry. The primitive polyhedron subunit has these properties, but does not represent the octet-truss architecture, as noted above.

We again use mirror symmetries to reduce the conventional cell into a smaller representative subunit, which we transform into a polyhedron subunit by converting curved faces into flat faces, as illustrated by Figure 2.7e and f. The bounding volume of these two geometries is a right triangular prism whose base faces are normal to the vertical axis and whose lateral faces are normal to the horizontal plane, making it convenient to simulate effective transport in the vertical direction. Since we do not alter the beam orientations or bounding volume for the curved-to-flat transition, the topology remains consistent with the octet-truss.

In our simulations, we use the conventional representative subunit and conven-

tional polyhedron subunit as the computational domain because they can accurately reproduce the effective transport behavior of the full octet-truss nanolattice.

2.6 Geometry representation

To the best of our knowledge, nobody has previously attempted to simulate phonon transport in a structure as complex as a nanolattice. The literature describing Monte Carlo solvers of the Boltzmann transport equation does not address the issue of representing complex geometries. This section describes how to algorithmically find the nearest domain boundary during the advection step and how to determine whether a computational particle has escaped simulation domain. We present multiple schemes in order of increasing complexity and generality.

Consider a particle with initial position $\mathbf{x}_i$ and direction $\mathbf{u}_i$ moving along the trajectory $\mathbf{x}_i + \mathbf{u}_i d$ parameterized by distance d. For certain geometries, further specified later, we can find the nearest boundary by selecting the minimum non-negative distance,

$$d_{\text{bdry}} = \min_{d_j \geq 0} \{d_1, d_2, \dots\}, \tag{2.86}$$

to a set of hyperplanes that coincide with the domain boundaries $\partial\Omega_j$, which are lines in 2-D and planes in 3-D. To demonstrate how this works in practice, we look at an easy example.

One of the simplest, non-trivial simulation domains in 2-D is the unit square. We can mathematically describe the square as

$$\Omega_{\text{square}} = \{(x, y) \mid 0 < x < 1,\ 0 < y < 1\} \tag{2.87}$$

with boundary $\partial\Omega$. We also define the boundary lines formed by extending each edge,

$$\partial\Omega_1 = \{(x, y) \mid x = 0\} \tag{2.88a}$$

$$\partial\Omega_2 = \{(x, y) \mid x = 1\} \tag{2.88b}$$

$$\partial\Omega_3 = \{(x, y) \mid y = 0\} \tag{2.88c}$$

$$\partial\Omega_4 = \{(x, y) \mid y = 1\}. \tag{2.88d}$$

If a particle inside the domain has initial position $\mathbf{x}_i = (x_i, y_i)$ and direction $\mathbf{u}_i =$

(u_{xi}, u_{yi}), then we can determine the distances d_j to each boundary $\partial\Omega_j$ by solving

$$x_i + u_{xi} d_1 = 0 \tag{2.89a}$$

$$x_i + u_{xi} d_2 = 1 \tag{2.89b}$$

$$y_i + u_{yi} d_3 = 0 \tag{2.89c}$$

$$y_i + u_{yi} d_4 = 1. \tag{2.89d}$$

We can simplify the routine by considering the particle direction. The set of distances d_j usually consists of two positive and two negative values, corresponding to the boundary intersection points that lie forwards and backwards along the particle trajectory, respectively. We can readily categorize each boundary as ahead or behind based on the particle direction, so that we only need to calculate d_j for two of the boundaries. For example, a particle with $u_{xi} > 0$ and $u_{yi} < 0$ can only collide with either the $x = 1$ or $y = 0$ boundaries. If the particle moves vertically with $u_{xi} = 0$ or horizontally with $u_{yi} = 0$, then its trajectory never intersects either the x or the y boundaries. We check for these situations and set the corresponding distances to infinity.

We further observe that the routine relies on convexity. A domain is convex if it fully contains all line segments joining any pair of its points. The convexity of the unit square implies that none of the boundary lines extend into the domain and all candidate collision points lie on the domain boundary or outside of the domain. Therefore, the closest intersection point will always fall on the actual domain boundary, a convenient property that applies to all convex geometries.

In general, any convex domain with flat edges or faces can be described as

$$\Omega_{\text{convex}} = \{\mathbf{x} \mid \mathbf{n}_j \cdot \mathbf{x} \geq b_j\}, \tag{2.90}$$

whose boundary hyperplanes are

$$\partial\Omega_j = \{\mathbf{x} \mid \mathbf{n}_j \cdot \mathbf{x} = b_j\}, \tag{2.91}$$

where $\mathbf{n}_j$ are the boundary normal vectors pointing towards the domain interior and b_j are constants specifying the separation between the boundary and the origin. We can calculate a particle's distance d_j to boundary $\partial\Omega_j$ by solving

$$\mathbf{n}_j \cdot \left(\mathbf{x}_i + \mathbf{u}_i d_j\right) = \mathbf{b}_j. \tag{2.92}$$

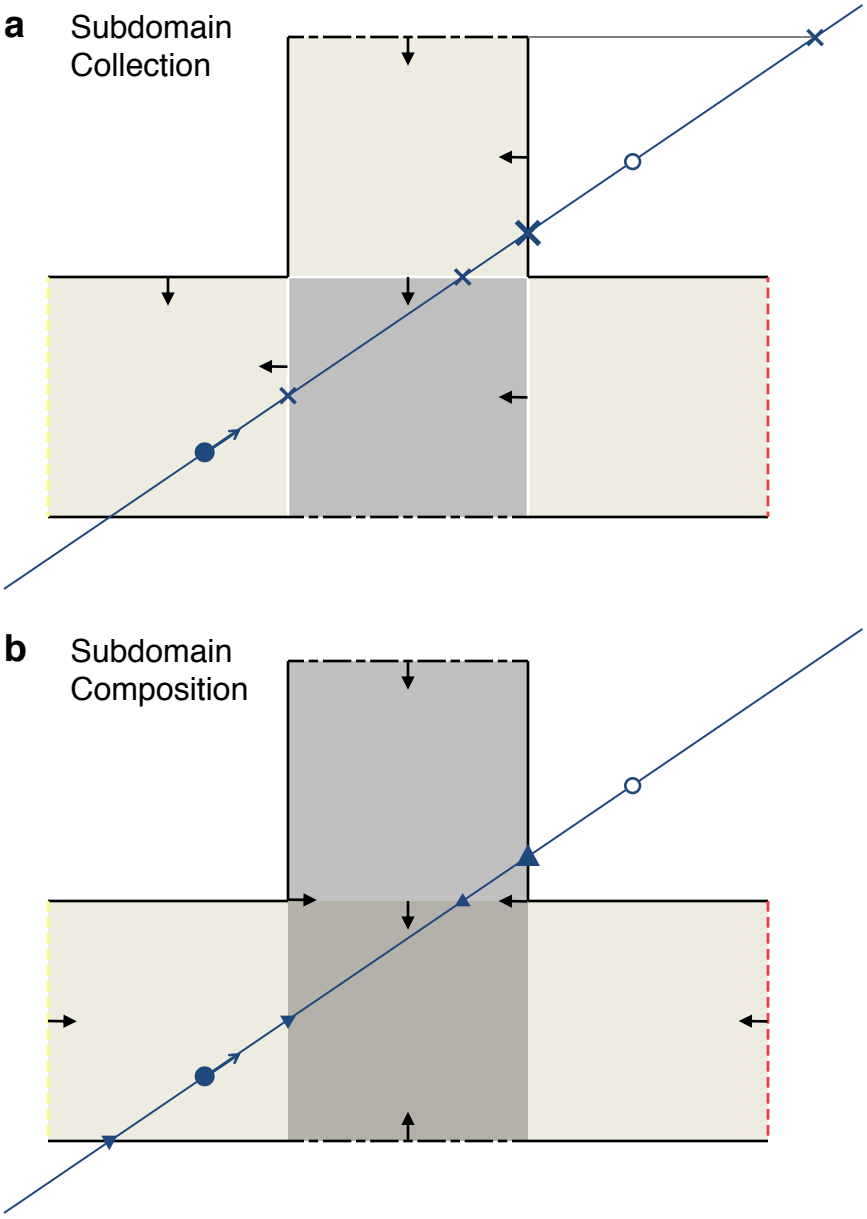

Figure 2.8: Two schemes for modeling a non-convex simulation geometry. We can represent the example tee domain as (a) a collection of non-intersecting subdomains or (b) a composition of intersecting subdomains. The advection procedure for each scheme differs, as explained in the main text.

The quantity $\mathbf{n}_j \cdot \mathbf{u}_i$ represents the direction component parallel to the boundary normal. As suggested for the unit square, we can ignore the boundary if the particle moves away from it, $\mathbf{n}_j \cdot \mathbf{u}_i > 0$, and we can set d_j to infinity if the particle moves parallel to it, $\mathbf{n}_j \cdot \mathbf{u}_i = 0$. Notably, this formulation works in both 2-D and 3-D.

For a non-convex domain with flat faces, we cannot use this strategy because the boundary hyperplanes cross into the domain. Without additional information, the algorithm would not allow particles to cross these "false" boundaries. We now explore three options for representing concave domains that involve finite boundaries, collections of subdomains, and compositions of subdomains.

The finite boundary approach still represents boundaries as hyperplanes, but it uses conditionals to specify the extent of the boundary. Every concave edge or vertex must have a conditional to test whether an intersection point actually lies inside the domain. With this scheme, particles may escape between a minuscule gap between two finite boundaries, and there does not exist an easy way to determine whether a particle has left the domain or not.

We can instead represent a concave geometry as a collection of non-intersecting, strictly convex subdomains. In this strategy, we partition the domain into smaller subdomains and track the region in which the particle resides. We apply the algorithm described above and consider only the boundaries of the current region. If the particle collides with a true domain boundary, then we apply the usual boundary conditions. Otherwise, if the particle collides with an inter-subdomain boundary, then we simply update the variable indicating the current subdomain. This scheme scales well with domain complexity because the number of checked boundaries does not increase with the number of overall domain boundaries. Instead, it corresponds to the number of subdomain boundaries, which remains low if we use simple building blocks.

We demonstrate how our subdomain collection method works by analyzing the tee geometry drawn in Figure 2.8. The existence of two 270° interior angles means that it is concave. To represent this tee in the current scheme, we split it into four square regions with four boundaries each. Now consider a particle in the lower left region of the tee moving towards the upper right. In Figure 2.8a, the solid blue circle and attached arrow indicate the particle position and movement direction. The blue line shows the particle trajectory line, which has four 'x' markers and an 'o' marker, which are boundary intersection points and the projected internal scattering location, respectively. In the first advection iteration, the particle resides in the lower left square, so the algorithm only checks the four boundaries of that subdomain. The particle cannot hit the bottom or left boundaries because of its direction, and the distance to the right boundary line is less than the distance to the top boundary line and the internal scattering distance, so the particle moves to the

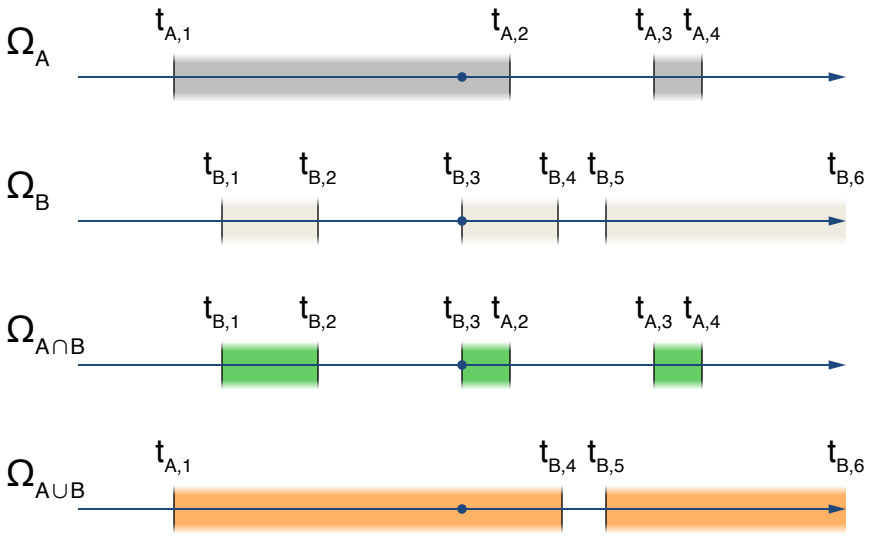

Figure 2.9: Trajectory line intersections for two subdomains Ω_A and Ω_B, their intersection $\Omega_{A\cap B}$, and their union $\Omega_{A\cup B}$. The circular marker and arrow represent the current particle position and direction. During the advection step, our subdomain composition scheme creates lists of the boundary crossing coordinates $\mathbf{d} = (d_1, d_2, \dots)$, and implements methods to merge these lists for intersections and unions of subdomains.

first 'x' marker. Since this boundary connects two subdomains, the algorithm shifts its attention to the middle subdomain. The particle moves to second and third 'x' markers in a similar manner.

The primary disadvantage of the subdomain collection scheme is the restriction that each boundary can only have a single boundary condition. We cannot define a face that scatters diffusely on one side and connects to another subdomain on the other, or even a face that connects with two different subdomains, without defining boundary extents within each boundary hyperplane. Therefore, a small region of high complexity can propagate small subdomain elements across the entire domain. A high number of subdomains not only requires extra care to ensure correct domain setup, but also leads to a high number of inter-subdomain boundaries. These intermediate boundaries can break the free-flight of a particle into several advection steps, and thus algorithm iterations, which may significantly increase computational cost.

Another way to represent concave geometries involves the composition of subdomains. Drawing inspiration from set theory, we implement unions and intersections of subdomains. The union of two subdomains $\Omega_A \cup \Omega_B$ includes all points inside

either Ω_A or Ω_B, while their intersection $\Omega_A \cap \Omega_B$ only includes points inside both Ω_A and Ω_B. These two set operations can also be applied to more than two subdomains at once. For even greater flexibility, the subdomains themselves can be unions or intersections, in addition to simple geometric primitives. This method offers the ability to represent complex geometries with far fewer subdomains than the collection method.

Upon closer investigation, we realize that the convex subdomains described above are a particular type of bounded intersection. Specifically, they are just intersections of half-spaces defined by their boundary hyperplanes, as suggested by Eq. 2.90. One can show that the same advection algorithm proposed above will still work for intersections of subdomains.

However, the addition of subdomain unions necessitates modifications to the advection algorithm. For any given boundary crossing, we need to check whether the candidate collision point lies in any other subdomain. If so, then the particle continues to advect through the containing subdomain. If not, then the particle collides with the union boundary at that point. We wish to avoid checking boundaries multiple times for each segment of free flight between collisions, even if there are intermediate boundary intersections. To achieve this, we develop a method that builds a list of entrance and exit points of the trajectory line for a particular subdomain,

$$\mathbf{d} = (d_1, d_2, \dots), \tag{2.93}$$

whose elements d_k represent the distance to an intersection point from the particle's current position. The algorithm maintains two invariant properties of the list. First, the intersection points are ordered by distance such that

$$-\infty \leq d_k \leq d_{k+1} \leq \infty. \tag{2.94}$$

Second, the intersection points with odd indices represent entrance points and those with even indices represent exit points, such that

$$d_{2n-1} \leq d \leq d_{2n} \iff \mathbf{x}_i + \mathbf{u}_i d \in \Omega \tag{2.95}$$

for positive integers n. This constraint requires the list to have an even number of elements. This list of boundary crossings therefore divides the trajectory line into segments that alternately lie inside and outside of the subdomain. Once we have $\mathbf{d}$, we determine the next collision point by finding the first intersection point in the list with a non-negative distance. This step boils down to searching an ordered

list, which we accomplish by invoking the bisection method commonly packaged in many programming libraries. Clearly, this advection method expends the most computational effort on calculating the intersection list. We explain how to do this with a top-down approach.

We calculate the list of boundary crossings for a union or intersection by merging the corresponding lists of its constituents. Assume that we know $\mathbf{d}_A$ and $\mathbf{d}_B$ for Ω_A and Ω_B. For the intersection of these subdomains $\Omega_A \cap \Omega_B$, we iterate through the interior segments of $\mathbf{d}_A$, which we denote $(d_{A,2n-1}, d_{A,2n})$, selecting the crossing points in $\mathbf{d}_B$ bounded by the interval $d_{A,2n-1} \leq d_{B,k} \leq d_{A,2n}$ to include in the merged list. We add the entry and exit points to the list if and only if they fall inside Ω_B. Our implementation uses bisection to find the indices of where $d_{A,2n-1}$ and $d_{A,2n})$ would be inserted into the ordered list $\mathbf{d}_B$. Slicing the list $\mathbf{d}_B$ with these indices gives all the elements in the desired range. Checking the parity, even or odd, of the indices reveals the domain membership in Ω_B of the entry and exit points and tells us whether or not to add them to the new list.[1] The resulting boundary crossings list only includes trajectory segments common to both subdomains.

In lieu of rigorously proving the correctness of our list merging algorithm, we analyze the example shown in Figure 2.9. The method first considers the interval $(d_{A,1}, d_{A,2})$ and finds that their insertion positions in $\mathbf{d}_B$ are 1 and 4. We immediately know that $(d_{B,1}, d_{B,2}, d_{B,3})$ fall within the interval of interest and that $d_{A,1}$ lies outside Ω_B while $d_{A,1}$ lies inside. Therefore, the new list is $(d_{B,1}, d_{B,2}, d_{B,3}, d_{A,2})$ after the first iteration. For the interval $(d_{A,3}, d_{A,4})$, we calculate that their insertion points both equal 6. The list slice contains no elements, suggesting that no boundary crossings in $\mathbf{d}_B$ fall inside this trajectory segment. Since 6 is even, both end points of the segment belong to Ω_B and should be appended to the list. The merged list becomes $(d_{B,1}, d_{B,2}, d_{B,3}, d_{A,2}, d_{A,3}, d_{A,4})$, which accurately identifies the crossing points of $\Omega_{A\cap B}$.

For the union of two subdomains, $\Omega_A \cup \Omega_B$, we also iterate through the interior segments $(d_{A,2n-1}, d_{A,2n})$, but this time we remove all elements of $\mathbf{d}_B$ bounded by $d_{A,2n-1} \leq d_{B,k} \leq d_{A,2n}$. The entry and exit points are added if and only if they fall outside Ω_B. In this case, the output list includes all trajectory segments from either subdomain and merges any overlapping segments. We apply these merging routines cumulatively for a union or intersection of multiple subdomains. Since

[1] Note that we index list elements starting from 1 in this report, but many programming languages use 0-indexing.

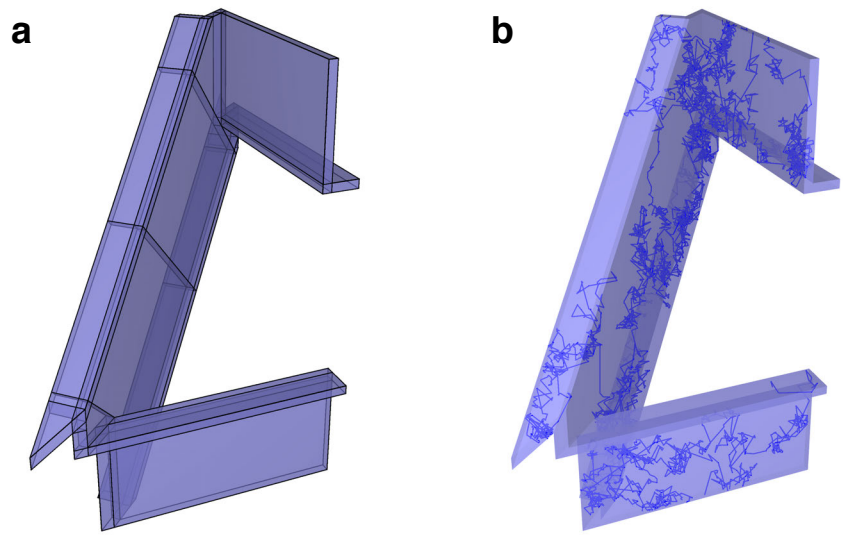

Figure 2.10: (a) Representation of the conventional polyhedron subunit (or rectangular subunit) as a collection of 42 convex subdomains. In our MC simulations, the faces that coincide with the top and bottom of the bounding volume (see Figure 2.11) have periodic boundary conditions and the remaining exterior faces have diffuse boundary conditions. (b) Example particle trajectory in the simulation domain.

these set operations commute, the order in which we combine the subdomains does not matter.

We compare and contrast the subdomain collection and subdomain composition schemes by revisiting the tee example. Figure 2.8b shows how we can represent the domain as the union of two rectangular domains. For the same initial position and direction as before, the particle moves through two intermediate boundaries and reaches its next collision location in a single advection step. However, the composition method calculates the boundary crossings list, which requires checking eight boundaries and merging the subdomain lists, compared to six boundary checks for the collection method.

We implemented both the subdomain collection and composition schemes in two versions of the Monte Carlo code written in C++ and Python, respectively. For our simulations of octet-truss nanolattices, we use the C++ code with the subdomain collection scheme. We split the conventional polyhedron subunit, or rectangular subunit, into the 42 convex subdomains illustrated in Figure 2.10a. It would not be possible to perform phonon Monte Carlo simulations efficiently in such a complex domain without these robust geometry representation schemes.

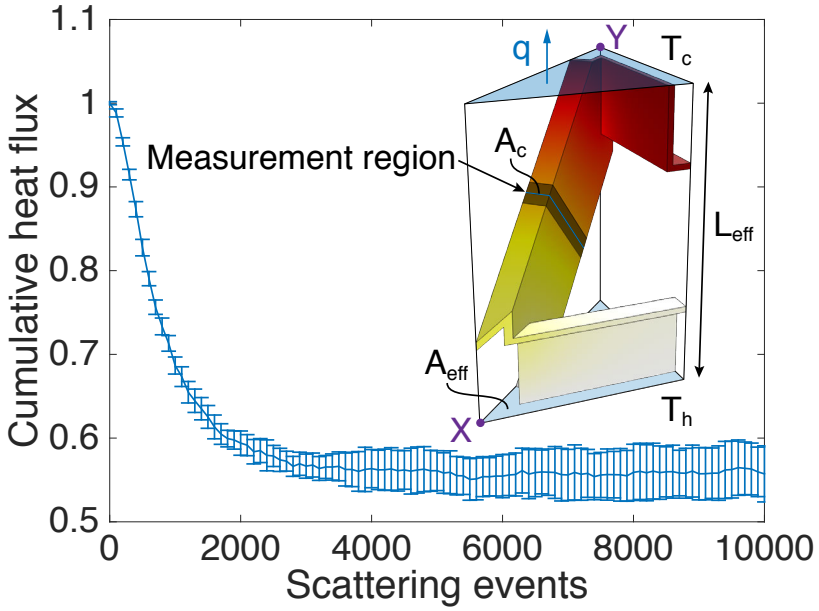

Figure 2.11: Example convergence of average heat flux with respect to scattering events in a MC simulation. Cumulative heat flux is normalized by the first scattering event contribution. The inset shows the FEM temperature field and measurement region with cross-sectional area A_c. Thermal conductivity is calculated from Fourier's law using the total heat current q, temperature difference $T_\mathrm{h} - T_\mathrm{c}$, effective area A_eff, and effective length L_eff. The full truss structure can be constructed by tessellating the bounding box, which contains two node points X and Y.

2.7 Silicon nanolattice simulations

We simulate a range of octet-truss nanolattices composed of silicon using our optimized MC method with the subdomain collection scheme. The structures have unit cell sizes W from 5 to 15 µm, major axis widths a from 0.4 to 1.2 µm, and wall thicknesses t from 10 to 100 nm. The minor axis width is $b = a/4$. We take the phonon dispersion and relaxation times of silicon from Reference 65. In each MC simulation, we establish a vertical temperature gradient across the geometry and calculate the average steady-state heat flux in a central measurement region as depicted in Figure 2.11 inset. Faces that intersect the top and bottom of the bounding volume (shaded blue) have periodic boundary conditions, and all other faces have diffuse boundary conditions, representing rough material surfaces. The effective thermal conductivity of the nanolattice is obtained using Fourier's law. We propagate ten million particles for ten thousand scattering events each, computing particle trajectories like the one shown in Figure 2.10b. Figure 2.11 demonstrates the

convergence of heat flux with respect to scattering events for a particular geometry.

Our BTE approach captures the thermal conductivity reduction due to both relative density and classical size effects. To isolate the role of size effects, we also solve the heat equation using the finite element method (FEM) software COMSOL and apply the same procedure as above to calculate effective thermal conductivity. The heat equation does not capture phonon size effects, so comparing MC and FEM results is a convenient way to isolate geometrical and size effects in nanolattice structures.

We now present the results of our calculations for the nanolattices. Figure 2.12a plots MC and FEM thermal conductivities of the rectangular subunit versus relative density. The thermal conductivities of all the nanolattices obtained from FEM collapse onto a single curve, implying that the relative density can mostly describe the geometrical factors affecting heat conduction. On the other hand, the MC results lie on separate curves that shift downwards as wall thickness decreases. This decrease in thermal conductivity suggests that size effects occur at the length scale of wall thickness, and that the geometrical reduction in thermal conductivity remains the same as that in the absence of size effects.

To explain the FEM data, we use a thermal resistance network consisting of a single resistor connecting node points X and Y in the subunit bounding box, as indicated in Figure 2.11 inset. This model assumes that no heat flows through the horizontal beams connecting isothermal nodes and that beam lengths are much greater than beam widths, $W \gg a, b, t$. We obtain a simple linear relation between thermal conductivity and relative density $\bar{\rho}$,

$$\frac{k_{\text{eff}}}{k_{\text{solid}}} = \frac{\bar{\rho}}{3}. \tag{2.96}$$

As shown in Figure 2.12a, the FEM simulation results are consistent with this resistor model, particularly for small values of $\bar{\rho}$ where the thin beam approximation is well satisfied. Therefore, the thermal conductivity of nanolattices in the absence of classical size effects can be determined using only the relative density.

We examine the role of phonon size effects by computing the ratio of MC to FEM thermal conductivities in Figure 2.12b. When plotted against wall thickness, the data matches well with Fuchs-Sondheimer theory [50], which describes thermal transport along thin films. The decrease in thermal conductivity with decreasing wall thickness is caused by boundary scattering at length scales commensurate to

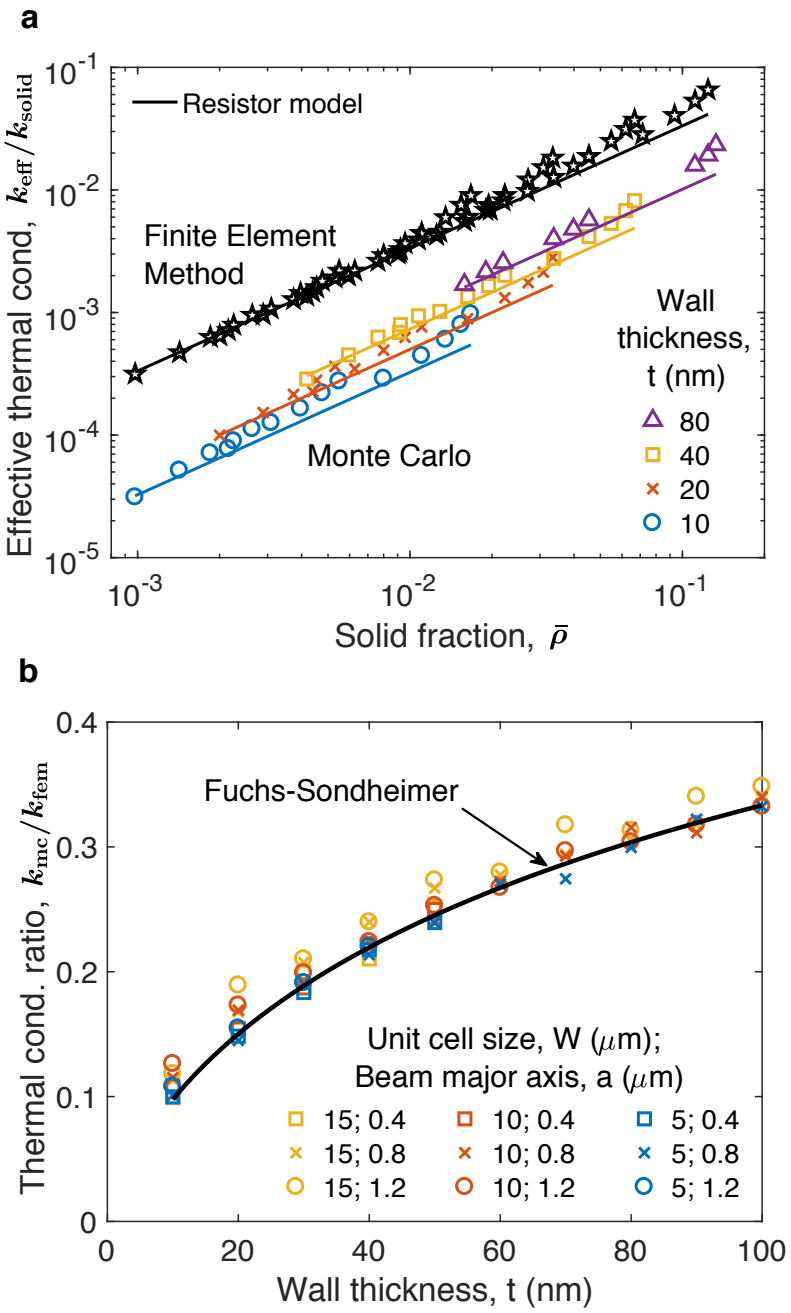

Figure 2.12: (a) Effective thermal conductivities of the rectangular subunit (symbols) versus relative density, calculated by our Monte Carlo method and the finite element method. These relative thermal conductivities are normalized by the solid phase thermal conductivity. The results are consistent with a simple thermal resistance model (lines). (b) Ratio of MC to FEM thermal conductivities (symbols) versus wall thickness, which reveals the thermal conductivity reduction due to phonon size effects. Agreement with Fuchs-Sondheimer theory (line) suggests that wall thickness is the critical thermal length.

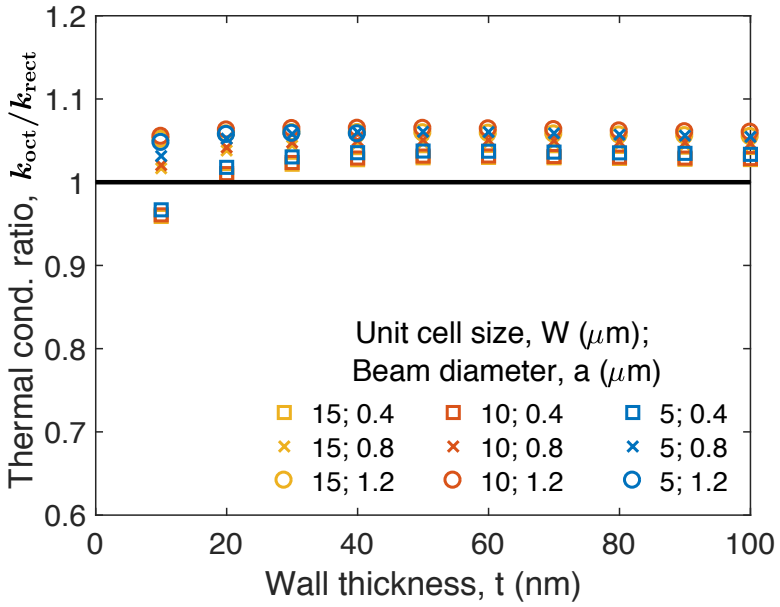

Figure 2.13: Ratio of octet (Figure 2.7e) and rectangular subunit (Figure 2.7f) thermal conductivities versus wall thickness calculated from finite element simulations. The ratio is close to unity, thereby justifying the geometric approximation of curved faces as flat faces.

phonon mean free paths. The theory explains our simulation results for the entire range of cell sizes and major axes considered in this study, implying that the dominant thermal length scale for nanolattices in this regime is wall thickness. Further, our calculation shows that the effect of boundary scattering can be described using the well-known analytical equation from Fuchs-Sondheimer theory.

The MC simulation results can be explained by combining the thermal resistance model with Fuchs-Sondheimer theory. The wall-thickness-dependent family of curves plotted in Figure 2.12a demonstrates that this hybrid theory can provide a reasonable estimate for the MC thermal conductivities. Hence, these simulation results show that octet-truss nanolattices can be modeled as a simple thermal resistance network with reduced solid thermal conductivity. Specifically, their thermal conductivity can be determined by two parameters—relative density describes geometrical effects through a thermal resistance model, and wall thickness describes size effects through Fuchs-Sondheimer theory.

To justify the approximation of curved faces as flat faces in this work, Figure 2.13 compares FEM simulations of the octet-truss and rectangular subunit structures, shown in Figure 2.7e and f, respectively. The thermal conductivities are within

6% of each other, which validates the approximation of curved faces as flat faces. Although these heat equation calculations do not account for classical size effects, we have demonstrated that size effects are primarily dependent on wall thickness, which is the same for both structures.

In summary, we simulated phonon transport in hollow-beam silicon nanolattices with the octet-truss architecture using a variance-reduced Monte Carlo algorithm to solve the BTE. Results indicate that nanolattice thermal conductivity can be calculated using only two parameters, relative density and wall thickness, which describe geometrical and size effects, respectively. Our technique enables the predictive design of nanolattice thermal conductivity.

Chapter 3

ELECTROTHERMAL METHOD FOR THERMAL CONDUCTIVITY MEASUREMENT

Our phonon transport simulations in Chapter 2 demonstrate that nanolattices achieve ultralow thermal conductivity because of low relative density and phonon size effects. Here, we experimentally prove those findings by fabricating and measuring the effective thermal conductivity of nanolattices using the 3ω technique. We first justify the suitability of 3ω for measuring nanolattices and explain the principles of how it works. We then describe the experimental setup built in our lab and the standard operating procedures. Next, we discuss the sample design and fabrication procedure adapted specifically for nanolattices. The unique sample geometry demands a custom thermal model for data analysis, which we derive.

3.1 Evaluation of thermal metrology techniques

The dimensions of nanolattices restrict the possible ways to measure their thermal conductivity. Existing technologies for synthesizing nanolattices make it infeasible to build a structure more than a few millimeters along a side, which is too small for conventional laser flash or hot wire methods. On the other hand, fabrication constraints set the minimum unit cell size to around 5 μm, below which lattice features become less clearly defined. A suitable experiment must have a measurement domain that encompasses a sufficient number of unit cells to accurately determine the effective thermal conductivity. We therefore seek an experimental technique that probes thermal properties at length scales of tens to hundreds of microns.

Several optical pump-probe techniques exist for nanoscale thermal metrology, most notably time-domain thermoreflectance (TDTR). TDTR uses a pulsed femtosecond laser to heat a sample and monitor its thermal response with excellent spatial and temporal resolution. The laser impinges on the sample surface and creates a Gaussian heating and sensing area with radius on the order of tens of microns. Researchers have used TDTR as a spectroscopic tool to study micro and nano-scale phonon transport phenomena in many materials. Despite the advantages of TDTR, there are thermal penetration depth concerns when investigating materials with ultralow thermal conductivity such as nanolattices.

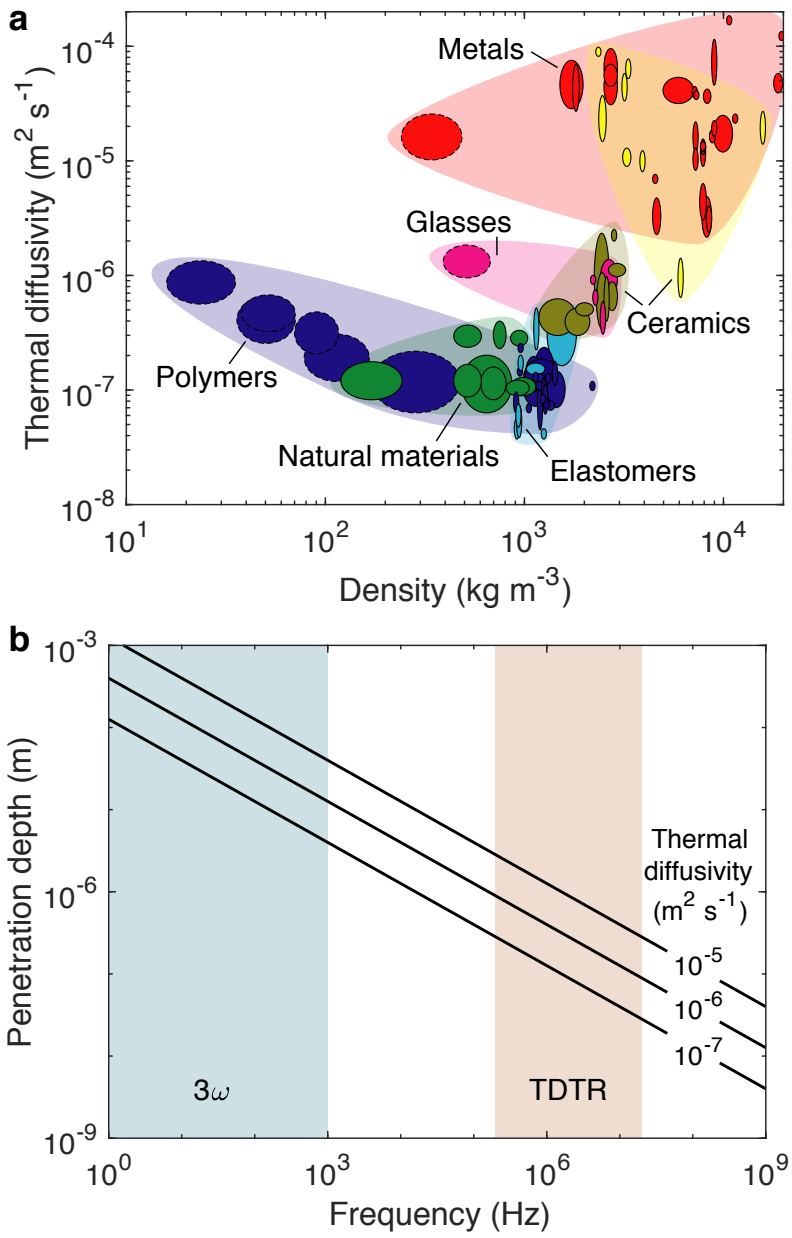

Figure 3.1: (a) Thermal diffusivity versus density of common materials, plotted using CES Selector. Outlined ellipses indicate the range of properties for a particular material (i.e. alumina) and lightly shaded regions encompassing the ellipses indicate the approximate range of properties for an entire class of materials (i.e. ceramics). Dashed outlines indicate foams. (b) Penetration depth versus frequency of a thermal wave, as given by Eq. 3.1. Shaded regions indicate the frequency ranges for the 3ω and TDTR experiments.

In this context, the concept of penetration depth arises from the spatial decay of a time-harmonic thermal wave. Oscillatory heating applied to a surface leads to temperature fluctuations whose amplitude is largest at the surface and exponentially smaller away from the surface. The length scale of thermal decay, called the penetration depth, is given by

$$\delta = \left(\frac{\alpha}{\omega}\right)^{1/2}, \tag{3.1}$$

where $\alpha = \kappa/(\rho c_p)$ is the thermal diffusivity of the medium and ω is the angular frequency of the wave. The penetration depth equals the thermal wavelength, or the distance that the wave travels within one period of oscillation.

All types of thermal metrology that rely on oscillatory heating rather than steady heating have a finite penetration depth, which determines the approximate region of experimental sensitivity. For such techniques, including TDTR, the thermal properties of the sample at locations far from the heating source relative to the penetration depth have negligible impact on the experimental signal. The penetration depth thus delineates the measurement domain in the direction normal to the heating surface.

Figure 3.1a shows the thermal diffusivities of common materials, grouped by class. The polymers and amorphous ceramics that compose nanolattices have relatively low thermal diffusivities from 10^{-7} to $10^{-6}\,\mathrm{m^2\,s^{-1}}$. In low density foams, air contributes significantly to thermal conductivity but does not add much to heat capacity, leading to elevated diffusivity compared to their constituent materials. We expect evacuated foams to possess diffusivities more similar to their bulk counterparts.

Heating frequency plays an equally important role in determining penetration depth, as illustrated by Figure 3.1b. TDTR operates at megahertz modulation frequencies, leading to penetration depths of 0.1 to 1 μm in nanolattice materials. A measurement domain of this size only covers a fraction of a unit cell, implying that we cannot use TDTR to characterize nanolattices.

Another technique called 3ω operates in the hertz to kilohertz frequency range, resulting in penetration depths of 10 to 1000 μm for polymers and ceramics. We note that the heating frequency for 3ω is twice the driving frequency, such that $\omega = 2\omega_0$ in Eq. 3.1. The measurement area has typical dimensions of around $10 \times 1000\,\mu\mathrm{m}$. Since the measurement domain of 3ω satisfies the stated size requirements, we choose this method to evaluate the thermal conductivity of nanolattices.

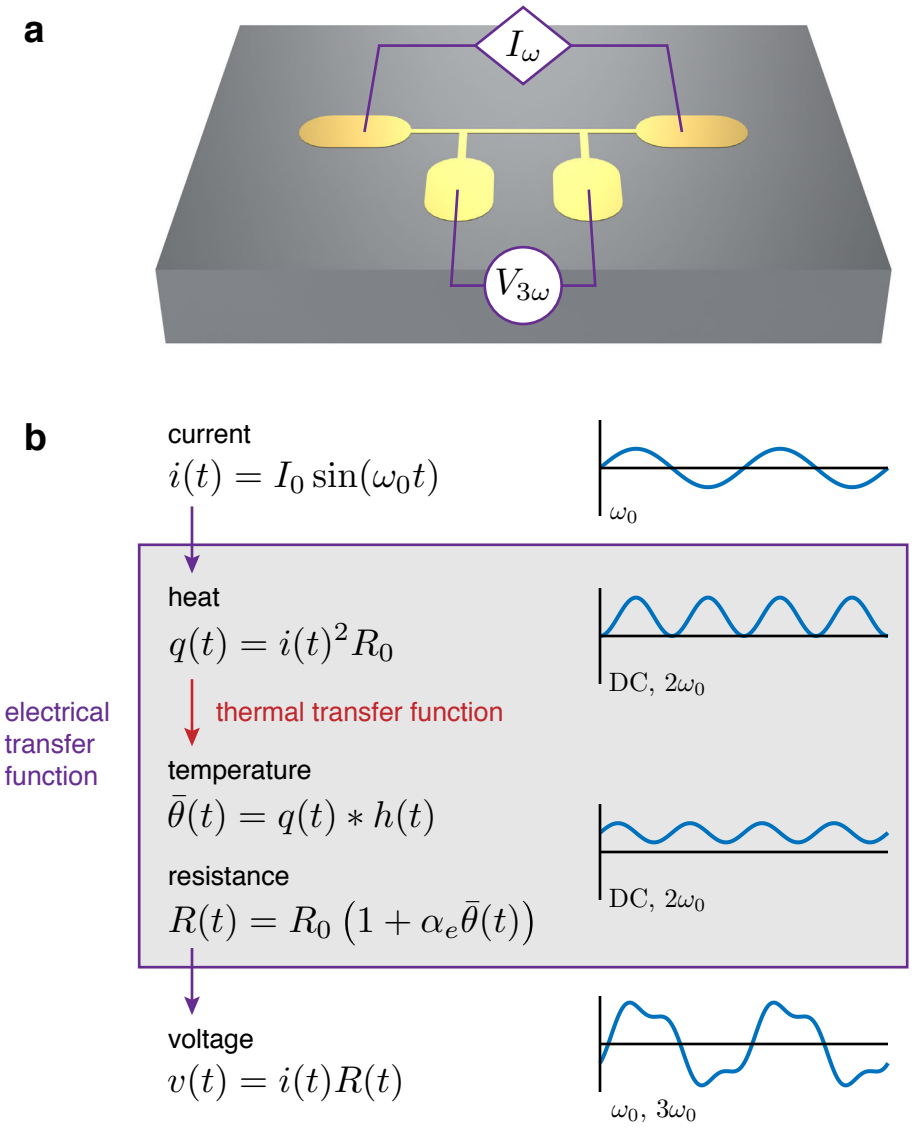

Figure 3.2: (a) Schematic illustration of a 3ω sample with a patterned metal line connected in a 4-wire sensing configuration. (b) Schematic relationship between thermal and electrical signals in the 3ω method, adapted from Reference 66.

3.2 3ω method

The 3ω method is an electrothermal measurement technique that employs a thin metal line for Joule heating and resistance thermometry [67]. Here, we outline the basic principles of the 3ω method using a systems approach, following Dames and Chen [66]. Corresponding lowercase and uppercase variables in this section denote a Fourier transform pair.

We can treat any 3ω sample as a thermal system for which input heat $q(t)$ from a

resistor causes an output temperature rise $\bar{\theta}(t) = T(t) - T_\infty$ of the resistor, averaged over its width and length. A linear transfer function $H(\omega)$, also called the frequency response, describes the general behavior of such a system in the frequency domain,

$$\bar{\Theta}(\omega) = Q(\omega)H(\omega). \tag{3.2a}$$

In the time domain,

$$\bar{\theta}(t) = q(t) * h(t), \tag{3.2b}$$

where $*$ denotes convolution and $h(t)$ is the inverse Fourier transform of the frequency response, also called the impulse response. Oscillatory heating at a frequency ω_0

$$q(t) = e^{j\omega_0 t} \tag{3.3a}$$

$$Q(\omega) = 2\pi\delta(\omega - \omega_0) \tag{3.3b}$$

leads to a temperature rise of the same frequency,

$$\bar{\Theta}(\omega) = 2\pi\delta(\omega - \omega_0)H(\omega) \tag{3.4a}$$

$$\bar{\theta}(t) = H(\omega_0)e^{j\omega_0 t}. \tag{3.4b}$$

The complex-valued transfer function $H(\omega)$ depends on the sample geometry and thermal properties, including densities, specific heats, and thermal conductivities of constituent materials.

The resistive metal line translates the thermal transfer function into a measurable electrical transfer function. This line not only generates heat, but also senses the temperature rise via its temperature-dependent resistance,

$$R(t) = R_0 \left(1 + \alpha_e \bar{\theta}(t)\right), \tag{3.5}$$

where R_0 is the zero-current resistance and $\alpha_e \equiv 1/R_0\,(dR/dT)$ is the temperature coefficient of resistance (TCR). This equation for electrical resistance holds even if the temperature $\theta(z,t)$ varies along the heater line. The gold heater lines used in this work have TCR values of 0.002 to 0.005 K^{-1} for temperatures of 30 to 300 K.

Figure 3.2 shows the heater line connected in a 4-wire sensing configuration. An AC current source supplies

$$i(t) = I_0 \sin(\omega_0 t) \tag{3.6a}$$

$$I(\omega) = j\pi I_0 \left[\delta(\omega + \omega_0) - \delta(\omega - \omega_0)\right], \tag{3.6b}$$

causing Joule heating,

$$q(t) = i(t)^2 R(t) \tag{3.7a}$$
$$= Q_0 \left[1 - \cos(2\omega_0 t)\right] \tag{3.7b}$$
$$Q(\omega) = \pi Q_0 \left[2\delta(\omega) - \delta(\omega + 2\omega_0) - \delta(\omega - 2\omega_0)\right], \tag{3.7c}$$

where $Q_0 = I_0^2 R_0/2$. We drop the resistance deviation term, $\alpha_e \bar{\theta}(t) \ll 1$, to get a leading-order approximation of the generated heat. The input heating consists of a DC component and an AC component at 2ω, resulting in a temperature rise with corresponding DC and AC components,

$$\bar{\Theta}(\omega) = \pi Q_0 \left[2\delta(\omega) - \delta(\omega + 2\omega_0) - \delta(\omega - 2\omega_0)\right] H(\omega) \tag{3.8a}$$
$$\bar{\theta}(t) = Q_0 \left[H(0) - \frac{1}{2} H(-2\omega_0) e^{-2j\omega_0 t} - \frac{1}{2} H(2\omega_0) e^{2j\omega_0 t}\right] \tag{3.8b}$$
$$= Q_0 \left[H(0) - \mathrm{Re}\{H(2\omega_0)\} \cos(2\omega_0 t) + \mathrm{Im}\{H(2\omega_0)\} \sin(2\omega_0 t)\right]. \tag{3.8c}$$

We can convert the complex exponentials into sines and cosines because the thermal impulse response $h(t)$ must be real-valued, implying that $H(-\omega) = H^*(\omega)$ in the frequency domain, where the asterisk superscript denotes complex conjugation. Note that the temperature rise contains in-phase and out-of-phase parts at nonzero frequencies that correspond to the real and imaginary parts of the transfer function, respectively. The temperature fluctuation at 2ω causes a fluctuation of electrical resistance per Eq. 3.5, so the first-order perturbation to the heater line voltage is

$$v(t) = i(t) R(t) \tag{3.9a}$$
$$= V_0 \sin(\omega_0 t) \left(1 + \alpha_e \bar{\theta}(t)\right) \tag{3.9b}$$
$$= V_0 \sin(\omega_0 t) \Big(1 + \alpha_e Q_0 [H(0) - \mathrm{Re}\{H(2\omega_0)\} \cos(2\omega_0 t) + \mathrm{Im}\{H(2\omega_0)\} \sin(2\omega_0 t)]\Big) \tag{3.9c}$$
$$= \frac{V_0}{2} \alpha_e Q_0 \Bigg[\frac{2}{\alpha_e Q_0} \sin(\omega_0 t) + 2H(0) \sin(\omega_0 t) + \mathrm{Re}\{H(2\omega_0)\} \left(\sin(\omega_0 t) - \sin(3\omega_0 t)\right) + \mathrm{Im}\{H(2\omega_0)\} \left(\cos(\omega_0 t) - \cos(3\omega_0 t)\right)\Bigg] \tag{3.9d}$$
$$= \frac{V_0}{2} \alpha_e Q_0 \Bigg[\left(\frac{2}{\alpha_e Q_0} + 2H(0) + \mathrm{Re}\{H(2\omega_0)\}\right) \sin(\omega_0 t) + \mathrm{Im}\{H(2\omega_0)\} \cos(\omega_0 t) - \mathrm{Re}\{H(2\omega_0)\} \sin(3\omega_0 t) - \mathrm{Im}\{H(2\omega_0)\} \cos(3\omega_0 t)\Bigg], \tag{3.9e}$$

where $V_0 = I_0 R_0$ is the ohmic voltage drop.

The relationship between these thermal and electrical signals becomes more intuitive when expressed as the imaginary part of complex exponentials. Euler's formula implies

$$\sin(n\omega_0 t) = \mathrm{Im}\{e^{jn\omega_0 t}\} \tag{3.10a}$$

$$\cos(n\omega_0 t) = \mathrm{Im}\{je^{jn\omega_0 t}\} \tag{3.10b}$$

for $n \in \mathbb{Z}$, so we can concisely summarize the important time-domain signals as

$$i(t) = I_0 \,\mathrm{Im}\{e^{j\omega_0 t}\} \tag{3.11}$$

$$q(t) = Q_0 \,\mathrm{Im}\left\{j - je^{2j\omega_0 t}\right\} \tag{3.12}$$

$$\bar{\theta}(t) = Q_0 \,\mathrm{Im}\left\{jH(0) - jH(2\omega_0)e^{2j\omega_0 t}\right\} \tag{3.13}$$

$$v(t) = V_0 \alpha_e Q_0 \,\mathrm{Im}\left\{\left(\frac{1}{\alpha_e Q_0} + H(0) + \frac{1}{2}H(2\omega_0)\right)e^{j\omega_0 t} - \frac{1}{2}H(2\omega_0)e^{3j\omega_0 t}\right\}. \tag{3.14}$$

Phase-sensitive detection with a lock-in amplifier enables the extraction of specific frequency components from the voltage $v(t)$, separated into in-phase (X) and out-of-phase (Y) parts with respect to the current $i(t)$. Using lock-in measurements at ω and 3ω, we obtain the time-invariant complex quantities

$$V_1(\omega_0) \equiv X_1(\omega_0) + jY_1(\omega_0) = V_0\left(1 + \alpha_e Q_0 H(0) + \frac{1}{2}\alpha_e Q_0 H(2\omega_0)\right) \tag{3.15}$$

$$V_3(\omega_0) \equiv X_3(\omega_0) + jY_3(\omega_0) = -\frac{V_0}{2}\alpha_e Q_0 H(2\omega_0). \tag{3.16}$$

We can express the lock-in signals in terms of the temperature rise components

$$\Theta_0 \equiv Q_0 H(0) \tag{3.17}$$

$$\Theta_2(\omega_0) \equiv Q_0 H(2\omega_0), \tag{3.18}$$

where Θ_0 is the real-valued steady-state temperature rise, the magnitude of Θ_2 represents the peak amplitude of the 2ω temperature fluctuation, and the complex argument of Θ_2 represents the phase lag with respect to the heat generation. Substitution of these expressions leads to

$$V_1(\omega_0) = V_0\left(1 + \alpha_e\Theta_0 + \frac{1}{2}\alpha_e\Theta_2(\omega_0)\right) \tag{3.19}$$

$$V_3(\omega_0) = -\frac{V_0}{2}\alpha_e\Theta_2(\omega_0). \tag{3.20}$$

For small temperature fluctuations, $1 \gg \alpha_e\Theta_0 \geq \alpha_e|\Theta_2|$, so the ohmic voltage dominates the ω signal, $V_1 \approx V_0$. More importantly, the 2ω temperature fluctuation is directly related to the 3ω signal,

$$\Theta_2(\omega_0) = -\frac{2}{\alpha_e}\frac{V_3(\omega_0)}{V_0}. \tag{3.21}$$

We recover the full thermal frequency response $\Theta_2(\omega_0)$ by performing a sweep of ω_0. Equation 3.21 reveals the crucial link between the electrical and thermal domains underlying the 3ω method.

3.3 3ω experimental setup

The 3ω experimental setup built in the Minnich lab closely mimics the setup used by Prof. Renkun Chen at UCSD and described by Feser [68]. Figure 3.3a shows a photograph of the full setup with the important hardware labeled and schematically illustrates the electrical support circuitry. A 6221 current source (Keithley Instruments) generates a sinusoidal AC current that flows through the 3ω sample and a reference resistance while an SR830 digital lock-in amplifier (Stanford Research Systems, Inc.) monitors the voltages across the sample and reference.

The reference is a resistance decade box (Extech Instruments) that enables cancellation of V_1 while measuring V_3. In a typical experiment with approximately 1 K of temperature rise, $|V_1/V_3| > 1000$ because of the heater line TCR, $\alpha_e \sim 10^{-3}$. V_1 therefore becomes the dominant source of noise when measuring V_3. This does not pose an inherent problem for our lock-in, which has more than 100 dB of dynamic reserve in "high reserve" mode. However, eliminating V_1 allows V_3 to dominate the input signal and drastically reduces the necessary amount of dynamic reserve. Measurement precision improves in "normal" and "low noise" modes since the lock-in does not withhold as much dynamic range for protection against high amplitude noise that could cause overloading. The amplifier applies a larger amount of gain to the analog input signal before converting it to a digital signal, leading to higher precision readings.

Our cancellation scheme uses the differential input feature of the SR830 lock-in along with a few integrated circuit (IC) components. A voltage multiplier automates the V_1 cancellation process, which consists of a digital-to-analog converter (AD7541A, Analog Devices, Inc.) and an operational amplifier (AD744, Analog Devices, Inc.). Together, these ICs multiply the reference signal by a computer-controlled factor between zero and one, with 12 bits of precision. These 12 bits

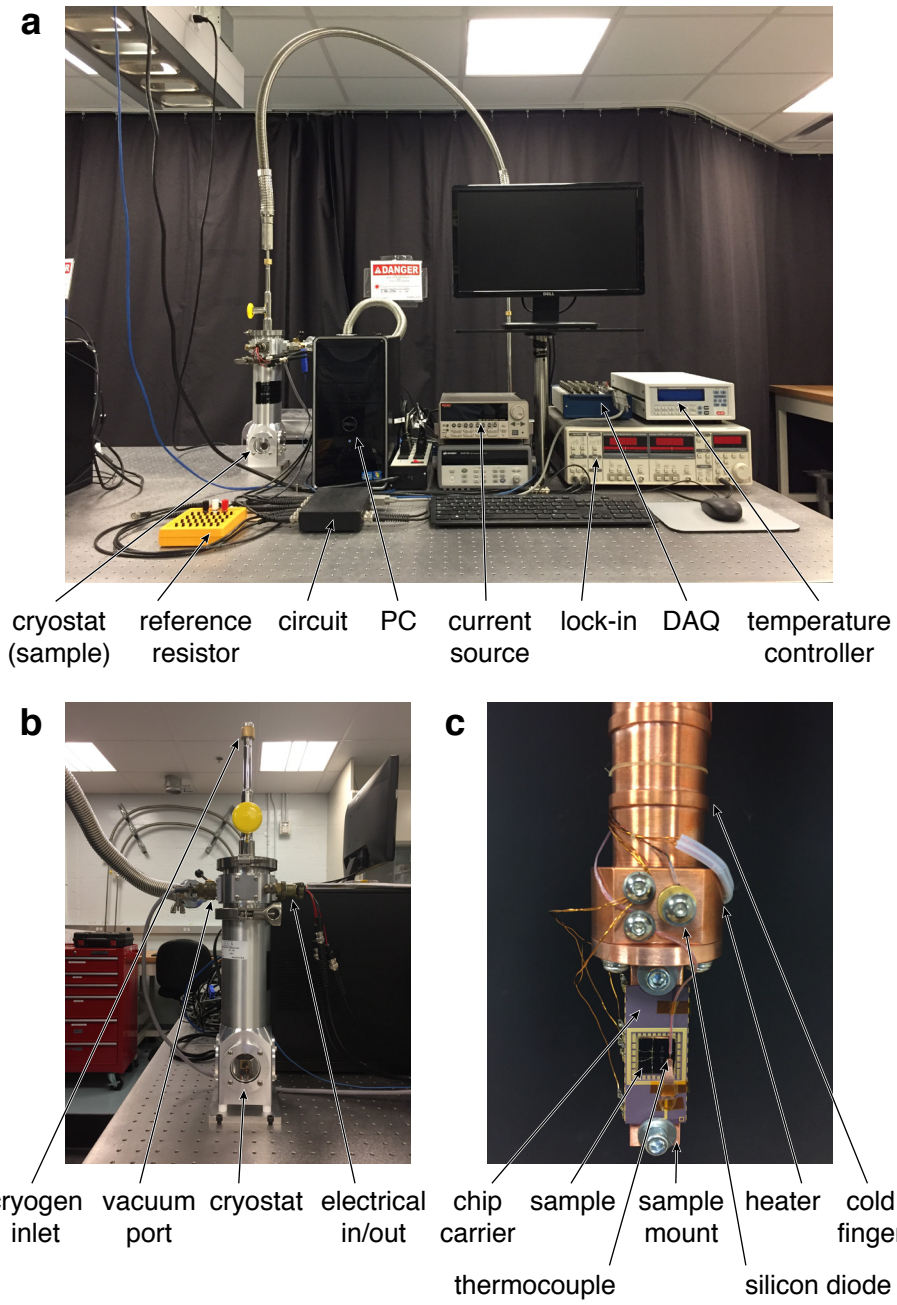

Figure 3.3: (a) The 3ω experimental setup in the Minnich Lab at Caltech. (b) Focused view of the cryostat. (c) Detailed view of a mounted sample.

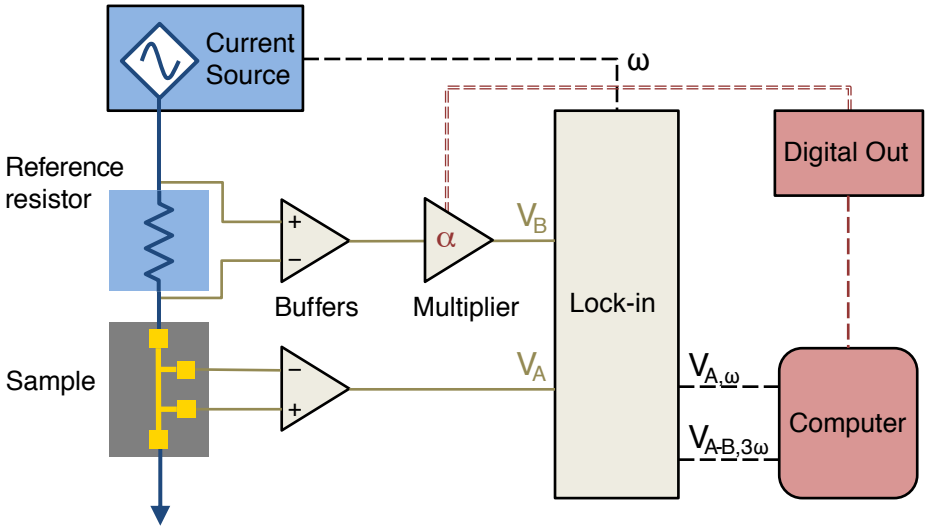

Figure 3.4: Block diagram of the 3ω circuit.

are given by 12 digital output lines of a data acquisition unit (National Instruments Corp.). Instead of tuning the reference resistance manually to match the resistance of the 3ω pattern on the sample, we programmatically adjust the multiplicative factor until the differential V_1 signal is minimized. Not only is this method more convenient, it also enables more complete cancellation, increasing the effective resistance resolution from $1\,\Omega$ of the discrete-valued decade box to $10^{-12}\,\Omega$ via the multiplier. Furthermore, we can automatically fine-tune the cancellation factor during frequency and temperature sweeps to account for sample resistance variations. We determine the optimal cancellation factor prior to each V_3 measurement, as described in Section 3.4.

In addition, two precision instrumentation amplifiers (AD524, Analog Devices, Inc.) provide low-noise buffering for the voltage signals across the reference resistor and the sample. The buffers convert the floating signals into grounded signals that can be transferred by a single grounded coaxial cable, and allow the lock-in to perform measurements without affecting the system. Due to the inverting behavior of the buffers and the multiplier, we carefully select the positive and negative buffer inputs to ensure that the V_1 voltages across the sample and reference are not artificially inverted with respect to the injected current. The sample signal undergoes a single reversal while the reference signal undergoes two reversals, so we connect the buffers as shown in Figure 3.4.

The support circuitry is built on a soldered protoboard and housed inside an aluminum enclosure for physical and electrical protection. Internal connections between circuit components use 22 AWG wire for analog signals and 24 AWG wire for digital signals. External connections with other hardware use coaxial BNC cables for analog signals passing between the circuit, current source, cryostat, and lock-in. A D-sub connector carries the digital signals going from the DAQ to the circuit. The metal enclosure and shielded external cables offer resistance against electromagnetic interference. Previous circuit prototypes that used jumper cables on a breadboard suffered from significant electrical reactance issues at low and high frequencies.

The ST-100 cryostat (Janis Research Co.) shown in Figure 3.3b allows us to perform experiments at vacuum pressures and cryogenic temperatures. A TPS-compact turbo pumping system (Agilent Technologies) evacuates the cylindrical vacuum shroud through a port on the instrumentation skirt. The pumping system combines a dry scroll backing pump that rapidly brings the pressure from atmosphere to 10^{-1} torr with a turbomolecular pump that has a base pressure rating of 10^{-8} torr. In practice, we achieve chamber pressures in the 10^{-6} torr range, which nullifies the contribution of air conduction and convection during our measurements. At cryogenic temperatures, the high vacuum level becomes essential for minimizing heat transfer to the cold finger via gas molecules and preventing ice formation. Ice at any interface between the cold finger and the sample could increase thermal resistance and thus increase the sample temperature. Worse, ice on the sample could lead to excess heat capacity or thermal conductivity.

We control the temperatures inside the cryostat by balancing cooling power from a cryogenic liquid, heating power from a resistive heater, and heat leakage from the ambient environment. To reach temperatures below ambient, we apply a continuous flow of liquid nitrogen (LN2) or liquid helium (LHe), which have boiling temperatures of 77 K and 4 K, respectively. The flexible transfer line connecting the cryogen storage dewar to the cryostat has a needle valve that regulates flow rate. However, because of the complex two-phase nature of the cryogen flow, which transitions from fully liquid in the dewar to fully vapor at the cryostat exhaust port, the needle valve only allows for crude control of the cooling power. In general, we use the minimum possible flow rate that can cool the system to the lowest desired temperature in order to conserve the cryogenic liquid.

A Model 335 temperature controller (Lake Shore Cryotronics, Inc.) provides

very fine control of the heating power and ultimately the cold finger temperature. The controller monitors the cold finger temperature using input from a silicon diode sensor and then applies a proportional-integral-derivative (PID) control algorithm to determine the output power to a cartridge heater. We assign P, I, and D values using a zone-based scheme as suggested by Lake Shore. Figure 3.3c shows the cold finger with the temperature sensor mounted on top and the heater embedded inside. An electrical feedthrough on the instrumentation skirt enables electrical connections between the interior components and exterior controller without introducing vacuum leaks.

Heat leakage from the environment can can cause the sample temperature to rise above the cold finger temperature. If it becomes comparable to the cooling power, lowest achievable temperature is affected. To measure the sample temperature directly, we place a T type thermocouple directly in contact with the sample. This reading can still be inaccurate if the thermocouple is not thermally anchored because the wire itself can carry heat. The best way to mitigate these problems is to minimize environmental heat loads. All wires leading to the sample are wrapped around and tied at multiple points along the length of the cold finger. A radiation shield reduces radiative heat transfer from the vacuum shroud. A high vacuum level ensures minimal gas conduction and convection. We take further measures to reduce the thermal resistance between the cold finger and the sample. All physical parts are joined using cryogenic thermal grease, Apiezon N (M&I Materials, Ltd.), and pressure from a screw or clip. This applies to all junctions between the cold finger, sample mount, chip carrier, chip, and thermocouple. The lowest sample temperature we could obtain with liquid helium was around 25 K due to these external heat loads.

3.4 3ω data collection procedure

This section describes the standard operating procedure for data collection with our 3ω setup. We detail the manual steps for mounting a sample and the automated algorithm for taking experimental data.

We use the following procedure to mount each sample. First, we spread a small amount of cryogenic thermal grease onto the chip carrier and screw it down to the sample mount, as shown in Figure 3.3c. We then connect the four current and voltage wires to the appropriate pins of the chip package, whose lead frame and wire bonds connect to the contact pads on the sample. By checking the resistances between the connected pins, we verify electrical connectivity and ensure that measured

values match those obtained after fabrication. Abnormally high resistances require additional sample processing, as discussed in Section 3.5. Then, we attach the thermocouple to the chip by securing the wire to the chip package with polyimide (Kapton) tape and pressing the measuring junction onto the chip surface under a beryllium-copper clip along with some thermal grease. We also use Kapton tape to electrically insulate the exposed thermocouple wire from the metal clip and to secure the clip onto the chip package. To apply additional pressure to the thermocouple junction, we created a sheet metal part that attaches to the chip carrier screws and rests directly on top of the clip. After reassembling the cryostat, we pump the chamber for several hours until the pressure reaches 10^{-6} torr and cool the sample with liquid nitrogen or helium if needed. The temperature controller adjusts the heating power to balance the cooling power until the system reaches the set temperature.

Once the temperature and pressure inside the cryostat stablizes, we can start the experiment. A LABVIEW program automates the entire data collection process except for the initial setup of the reference resistor box, which we manually set to a value slightly above the maximum resistance measured while mounting the sample. During the initialization phase, the program establishes communication with the current source, lock-in, data acquisition unit, and temperature controller. The main outer loop iterates through a logarithmically-spaced list of frequencies ω_0. For each frequency, we set the current source to generate a sinusoidal signal with the specified peak amplitude I_0. We also activate a zero-degree phase marker, which means that the current source sends a pulse to its trigger link at the zero-phase point of every sine wave cycle. The trigger link output connects to the lock-in's reference input, so the lock-in can phase-lock its internal oscillator to the current signal. Now, the lock-in can access the voltage signals caused by the thermal response of the sample. The three signals that we measure are the ω_0 voltage across the sample, $V_{1,A}$, the ω_0 voltage difference between the sample and reference after cancellation, $V_{1,A-B}$, and the $3\omega_0$ voltage difference between the sample and reference, $V_{3,A-B}$.

For each voltage signal, we apply an iterative method to find appropriate lock-in and digital output parameters, and to obtain a stable and accurate reading. The lock-in filter settings allow users to control the width and roll-off steepness of the low-pass filter used to isolate the voltage signal at a particular frequency. We found that a time constant of 300 ms and slope of 24 dB oct^{-1} offers a good balance of noise rejection at the minimum frequency of about 1 Hz and signal convergence

rate at the maximum frequency of about 1000 Hz. We use the low-noise reserve setting for the single-ended measurement, V_A, and the normal reserve setting for the differential measurements, V_{A-B}. For each measurement, we take a sample of 30 readings at intervals of one time constant. We decide whether the signal has converged inside the sample window based on a statistical t-test of the differences between consecutive readings. The distribution of these differences should have a mean close to zero for a converged signal. If the signal has not converged, then we continue to take up to a maximum of 10 samples. We determine the optimal lock-in sensitivity that accommodates both the converged signal and its fluctuations, and if that setting differs from the current setting, then we change it and repeat the sampling procedure. In the end, we get a set of converged lock-in readings taken with the ideal sensitivity, from which we take the mean and standard deviation.

As described in Section 3.3, we cancel out the V_1 during the V_3 measurement to improve precision, which we accomplish with the help of a voltage multiplier unit controlled by digital output lines of a DAQ. After measuring $V_{1,A}$, we have a decent idea of the heater line resistance based on the nominal current amplitude, $R_0 = V_0/I_0 \approx V_{1,A}/I_0$. We therefore set the initial multiplier value equal to $A_{V,0} = V_{1,A}/I_0 R_{\text{ref}}$ via the DAQ. To further improve cancellation, we employ Newton's method to determine the multiplier value for which the real part of the differential voltage $X_{1,A-B} = \text{Re}(V_{1,A-B})$ is closest to zero. We update the multiplier with the recurrence relation

$$A_{V,i+1} = A_{V,i} + \frac{X_{1,A-B}}{I_0 R_{\text{ref}}} \tag{3.22}$$

until the change becomes less than the 12-bit digital resolution, $\Delta A_V < 2^{-12}$. After finding the optimal multiplier value, we record $V_{1,A-B}$ and measure $V_{3,A-B}$. We also record the thermocouple temperature throughout the experiment, which gives us the true sample temperature and tells us whether any temperature changes occurred during the experiment. Based on the measured $V_1(\omega_0)$ and $V_3(\omega_0)$ curves, we use Eq. 3.21 to calculate the average heater line temperature rise.

3.5 Nanolattice sample design and fabrication

Literature review leads to two conceivable ways to design a nanolattice sample for 3ω measurement. First, we could fabricate a nanolattice sheet on a high thermal conductivity substrate and pattern the heater line and contact pads on top, as illustrated in Figure 3.5a. The sheet must be at least a few millimeters on each side to accommodate the metal pattern. This design resembles the geometry used for

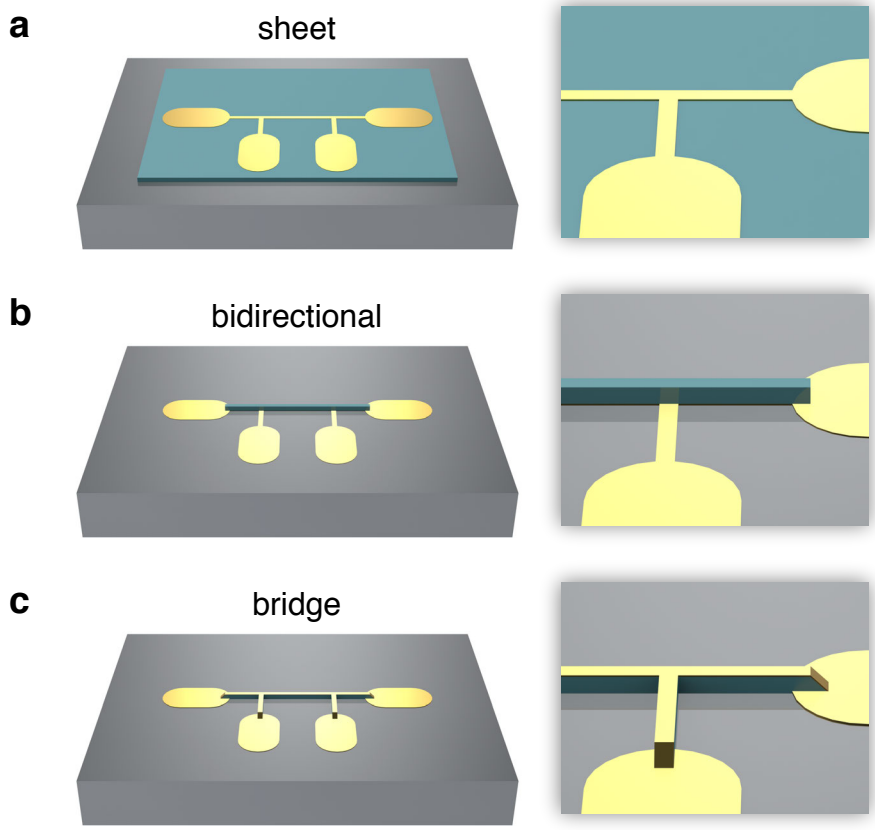

Figure 3.5: Three sample designs for 3ω measurement of nanolattices. (a) "Sheet" sample with the metal pattern on top of a nanolattice sheet. (b) "Bidirectional" sample with the metal pattern on the substrate and a narrow nanolattice covering only the heater line. (c) "Bridge" sample with the heater line on top of a narrow nanolattice and contact pads on the substrate. We use the bridge design because it minimizes nanolattice volume while maintaining experimental sensitivity.

measurements of thin films and porous materials [39], but unlike previously studied materials, nanolattices cannot yet be constructed efficiently over millimeter-scale areas. Creating a sheet of sufficient size would take many days.

Second, we could pattern the metal line directly on a low thermal conductivity substrate and construct a narrow nanolattice that covers only the heater line. As seen in Figure 3.5b, the substrate provides physical support for the contact pads so we can minimize the nanolattice size in the lateral direction with respect to the heater line. Heat travels one-dimensionally through the nanolattice in the cross-plane direction such that there is no excess volume that does not contribute to the thermal signal. Unfortunately, a majority of the heat diffuses into the substrate instead of the nanolattice because nanolattices have much lower thermal conductivity than any commonly available substrate material. The analysis done in Section 3.6 proves that the temperature response depends mostly on thermal properties of the substrate in this bidirectional design.

Neither the sheet design nor the bidirectional design work well for 3ω measurements of nanolattices, but we can combine elements of each to create a more suitable design. Our design includes a long, narrow nanolattice with the same dimensions as the heater line. We align the 3ω pattern with the structure such that metal coats the entire top surface of the nanolattice. Ramps connect the metal line to four contact pads that lie on the substrate. Our measured nanolattice samples use this design, which is illustrated in Figure 3.5c.

We fabricated alumina nanolattices using the process outlined in Figure 3.6a. We first create a three-dimensional polymer scaffold using two-photon lithography (TPL) and then conformally coat it with alumina using atomic layer deposition (ALD). We hollow out the structure by milling away sacrificial beams using a focused ion beam (FIB) and etching away the underlying polymer using oxygen plasma [69]. We then deposit 100 nm of gold through an aligned shadow mask to create a metal line on top of the structure connected to four contact pads on the substrate. The resulting alumina nanolattice depicted in Figure 3.6b and c is 50 µm tall, 50 µm wide, and 3 mm long. A cross-section of the structure in Figure 3.6d shows the octet-truss architecture and the top plate, which is written as a mesh during TPL. Pores of the polymer mesh are filled during ALD, forming alumina pillars that provide channels for heat conduction after the polymer is etched away. A side view of the nanolattice in Figure 3.6e highlights one of the four ramps that connect the heater line to the contact pads. Also shown are the sacrificial beams

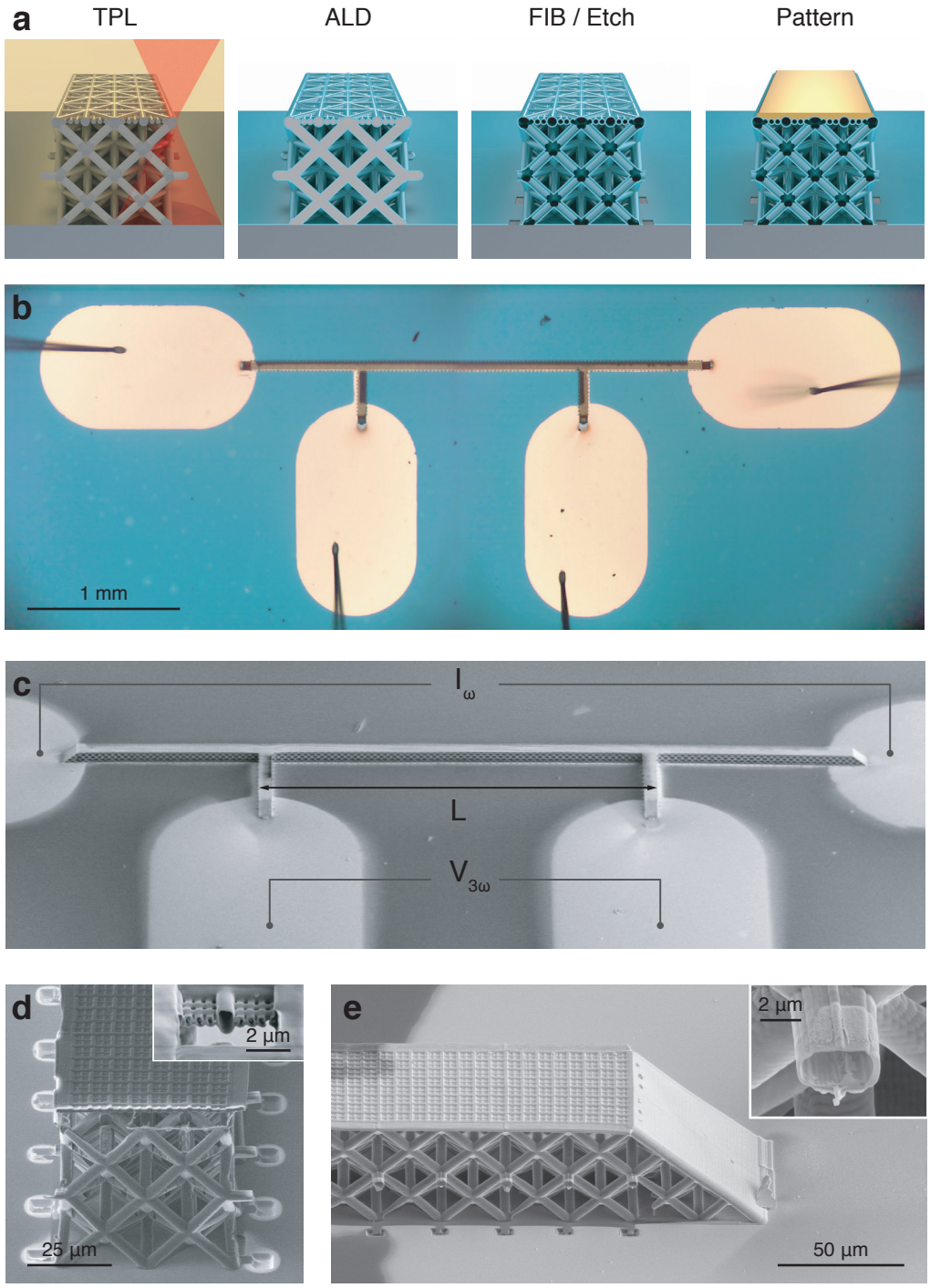

Figure 3.6: (a) Fabrication process for hollow alumina nanolattices using two-photon lithography and atomic layer deposition. (b) Optical microscope and (c) SEM images of the full sample geometry indicating the locations of current injection I_ω and voltage measurement $V_{3\omega}$. The length of the measured region is $L = 1.5$ mm. (d) Cross-sectional view showing the octet-truss architecture, the mesh top plate, and (inset) alumina pillars spanning the plate. (e) Side view highlighting a ramp and (inset) a sacrificial beam.

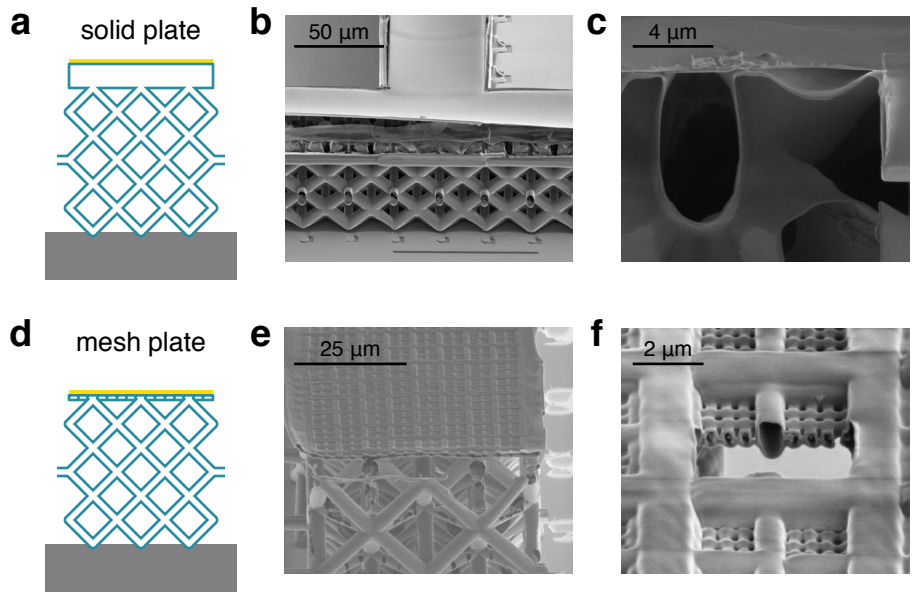

Figure 3.7: (a) Solid plate design. (b) Thick-walled solid plate (~ 205 nm Al_2O_3) with milled edges, showing a gap between the top and bottom layers. (c) Thin-walled solid plate (~ 32 nm Al_2O_3) with collapsed layers. (d) Mesh plate design. (e) Thin-walled mesh plate (~ 33 nm Al_2O_3) (f) with solid conduction pathways across the plate.

through which the etchant plasma accesses the internal polymer in the nanolattice.

To create hollow alumina nanolattice samples suitable for the 3ω experiment, we augment the general fabrication process outlined by Meza et al. [69]. The procedure begins by creating an octet-truss polymer scaffold using a two-photon lithography direct laser write process. We use the Photonic Professional system (Nanoscribe GmbH) with the proprietary IP-Dip photoresist. The Nanoscribe system incorporates a mirror galvanometer that enables rapid in-plane rastering and reduces the write time for this millimeter-length structure to a few hours. The structures are developed using propylene glycol methyl ether acetate and isopropyl alcohol.

A highly conformal layer of amorphous aluminum oxide is coated onto this polymer scaffold using a Savannah atomic layer deposition (ALD) system (Cambridge Nanotech). One ALD cycle consists of pulsing trimethylaluminum for 0.015 s, purging for 20 s, pulsing water for 0.015 s, and purging again for 20 s. The deposition chamber is held at 150 °C as 20 sccm of N_2 carrier gas is flowed through continuously. This ALD recipe produces self-limited growth of Al_2O_3 at a rate of 1.07 Å per cycle. Film thickness measurements taken with an alpha-SE ellipsometer (J.

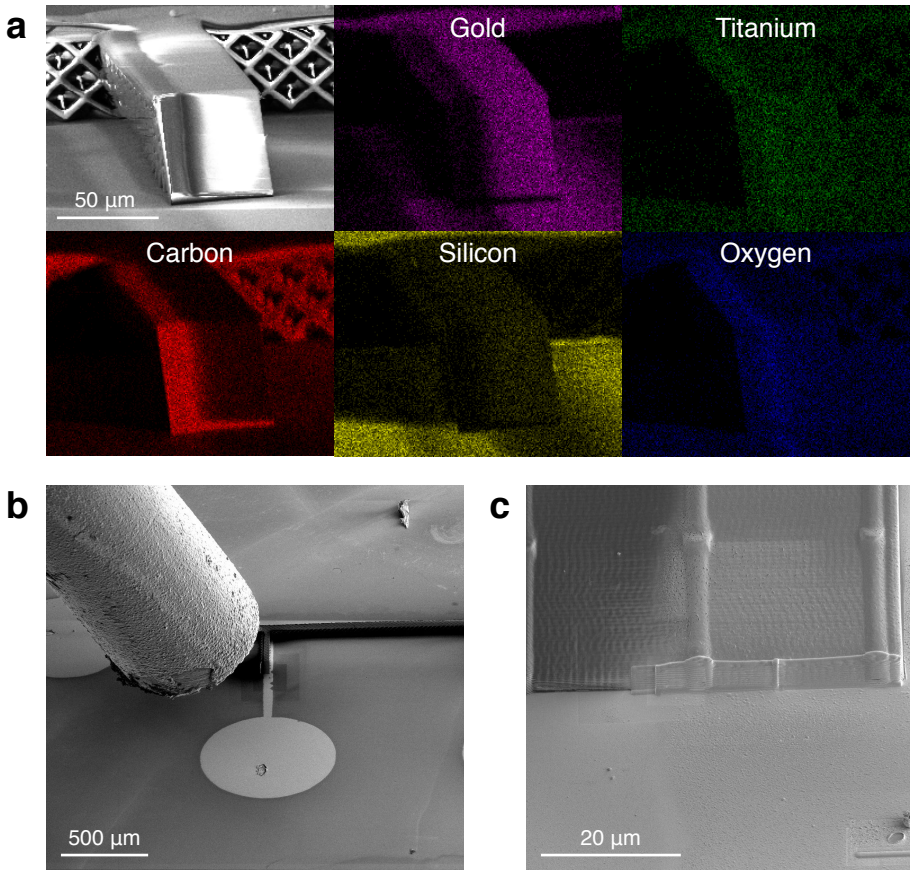

Figure 3.8: (a) Energy-dispersive X-ray spectroscopy reveals a gold discontinuity at the bottom edge of a nanolattice side ramp. (b) Gas-injection needle of a Nova NanoLab system (FEI Co.) used for ion beam-induced deposition of (c) a tungsten patch to bridge the disconnect.

A. Woollam Co.) confirm the accuracy of the recipe deposition rate to within 1 percent. The resulting nanolattice has beams with a polymer core encapsulated by an alumina shell.

We then remove the polymer inside the beams by milling away sacrificial beams with a focused ion beam (FIB) and etching away the polymer through these openings with oxygen plasma. The FIBs are part of larger Nova 200/600 NanoLab systems (FEI Co.) and the plasma asher is a Zepto unit (Diener electronic GmbH). To expedite complete removal of the polymer, we write sacrificial beams at the vertical center of the structure so that the longest diffusion paths to the top and bottom are minimized. All samples are etched for at least 36 hours with 100 W of power and the

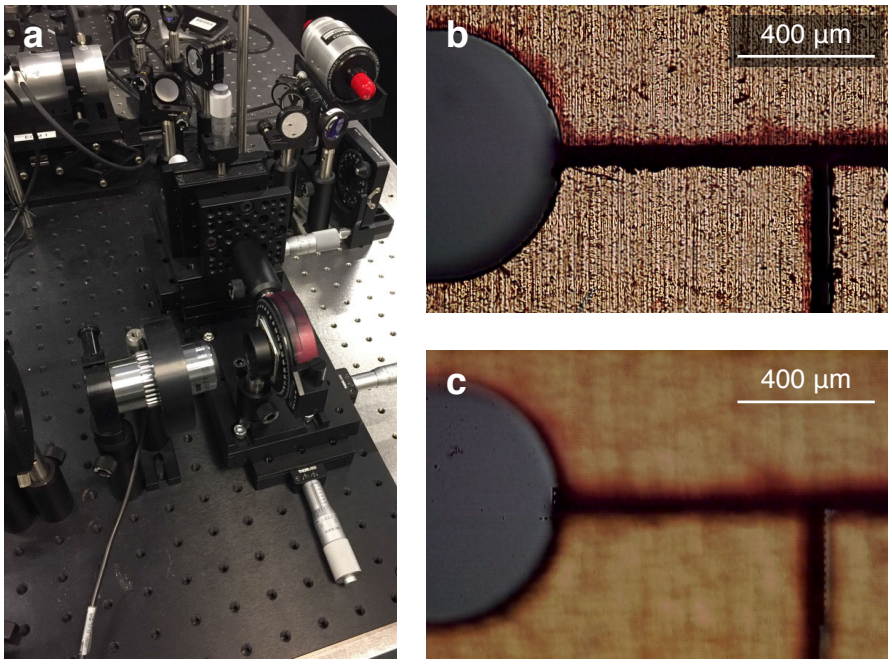

Figure 3.9: (a) Custom rig for manual mask alignment under an optical microscope. Since the mask is elevated above the nanolattice, checking their relative position requires switching between the focal plane of (b) the mask and (c) the nanolattice.

structures are inspected afterwards under a scanning electron microscope to check for a contrast change indicating that the beams are hollow.

Finally, we deposit gold through an aligned shadow mask to create a continuous heater line on the structure connected to four contact pads on the substrate. The mask is laser cut from 0.005 in stainless steel and has maximum edge waviness less than 5 µm. It is suspended above the sample by a spacer to avoid damaging the nanolattice and aligned under an optical microscope using micrometer-controlled translation stages. Thin film deposition is done in a LAB Line E-Beam evaporator (Kurt J. Lesker Co.) at pressures in the 10^{-7} torr range. A 10 nm layer of titanium promotes adhesion of the 100 nm gold layer.

Precise positioning and edge sharpness of the metal pattern are not critical for the experiment. On our fabricated samples, the pattern deviates from the nanolattice by up to 10 µm due to imperfect alignment and non-normal evaporation through the mask, as seen in Figure 3.6c and Figure 3.8a. Incomplete coverage of the nanolattice top plate generally does not pose a problem because heat spreads laterally into the uncovered region of the plate. Conduction still occurs mostly in the cross-plane

direction due to the physical boundaries of the structure. On the other hand, pattern misalignment could create an alternate conductive path between contact pads on the substrate. These short circuits could lead to a secondary heater line that not only diverts current away from the heater line above the nanolattice, but also creates a secondary thermal and electrical signal. To mitigate this problem, we use a focused ion beam to sever any secondary metal paths formed by misalignment of the mask. Large offsets can typically be observed under an optical microscope. If the offset occurs along a voltage measurement branch, we use ion beam-induced tungsten deposition to pattern additional metal along the deficient branch to reinforce the electrical connection. If the offset occurs along the measurement section of the line, we typically discard the sample.

We attach the chip to a chip package that facilitates electrical connections to the 3ω pattern. Our CSB02813 packages (distributed by Spectrum Semiconductor Materials, Inc. and manufactured by Kyocera Corp.) have 28 leads and a large $10 \times 10\,\text{mm}$ cavity. The external pins of these side-brazed dual in-line ceramic packages mate easily with individual connector contacts, a dual in-line package socket, or even a breadboard without the need for soldering. We mount the chip inside the cavity with thermal grease and wire bond the four contact pads to four different leads. The Model 7476D wedge-wedge wire bonder (Westbond, Inc.) uses ultrasonic energy to attach aluminum wire to the gold contacts at room temperature.

Once bonding is complete, we can perform a quality control test by measuring the electrical resistances across the connected leads with a multimeter. We expect the resistances to be less than $100\,\Omega$. A resistance on the order of $1\,\text{k}\Omega$ may indicate a significant misalignment of the gold pattern with respect to the nanolattice, such that the effective line width becomes much less than the nanolattice width. We use the strategies described above to address alignment issues. A resistance on the order of $1\,\text{M}\Omega$ may indicate the presence of a conduction path through the substrate despite the absence of a continuous metal connection. This situation does not occur for nonconductive substrates, including undoped semiconductors with high resistivity. A lack of connection sometimes occurs due to a discontinuity along the bottom edge of a ramp, as shown in Figure 3.8a. Energy-dispersive X-ray spectroscopy shows a strong carbon signal and no gold signal at the ramp-substrate interface, which clearly confirms the existence of a gap. In this situation, we use ion beam-induced tungsten deposition to patch the disconnect, illustrated in Figure 3.8b and c. Unfortunately, any additional sample processing at this stage requires removal of the chip from the

package. After fixing the sample, we remount the chip, wire bond it, and test it again.

3.6 Nanolattice thermal model

To extract thermal properties from a 3ω experiment, we need a model to describe the heat transfer behavior of the sample. The thermal model should predict the measured temperature, $\Theta_2(\omega_0)$, from the sample geometry and material properties. We want to measure effective thermal conductivity and the primary mode of thermal transport in the 3ω method is conduction, so our models come from solutions of the heat diffusion equation.

In the simplest case of a long and thin heater on an isotropic semi-infinite substrate, heat diffuses radially outward from the line in a one-dimensional, axisymmetric manner. This situation occurs when $b \ll \delta \ll d$, where b is half the line width, $\delta = \sqrt{\alpha/2\omega_0}$ is the penetration depth, and d is the substrate thickness. Under these conditions, Cahill [67] shows that the measured temperature rise can be approximated by

$$\Theta_2(\omega_0) = \frac{Q_0}{\pi L \kappa}\left(\frac{1}{2}\log\left(\frac{\alpha}{b^2}\right) - \frac{1}{2}\log(2\omega_0) + \eta - i\frac{\pi}{4}\right), \tag{3.23}$$

where $\eta = 0.923$ is a constant. This line-source model predicts a constant out-of-phase signal and a linear in-phase signal with respect to the logarithm of frequency, as depicted in Figure 3.10. Investigators typically infer the substrate thermal conductivity from the slope of Θ_2 versus $\log(2\omega_0)$,

$$\kappa = -\frac{Q_0}{2\pi L}\left(\frac{d\Theta_2(\omega_0)}{d\log(2\omega_0)}\right)^{-1}. \tag{3.24}$$

This data reduction method, called the slope method, does not depend on line width, specific heat, or interfacial resistance, so uncertainties in those quantities do not affect the calculation of thermal conductivity. Many studies use the slope method rather than more sophisticated models due to its simplicity and robustness.

For the more general case of a multilayered system with anisotropic thermal properties, Borca-Tasciuc et al [70] give an analytic solution for the average temperature rise

$$\Theta_2(\omega_0) = -\frac{Q_0}{\pi L}\int_0^\infty \frac{1}{A_1\kappa_1 q_1}\frac{\sin^2(b\xi)}{(b\xi)^2}\,d\xi, \tag{3.25}$$

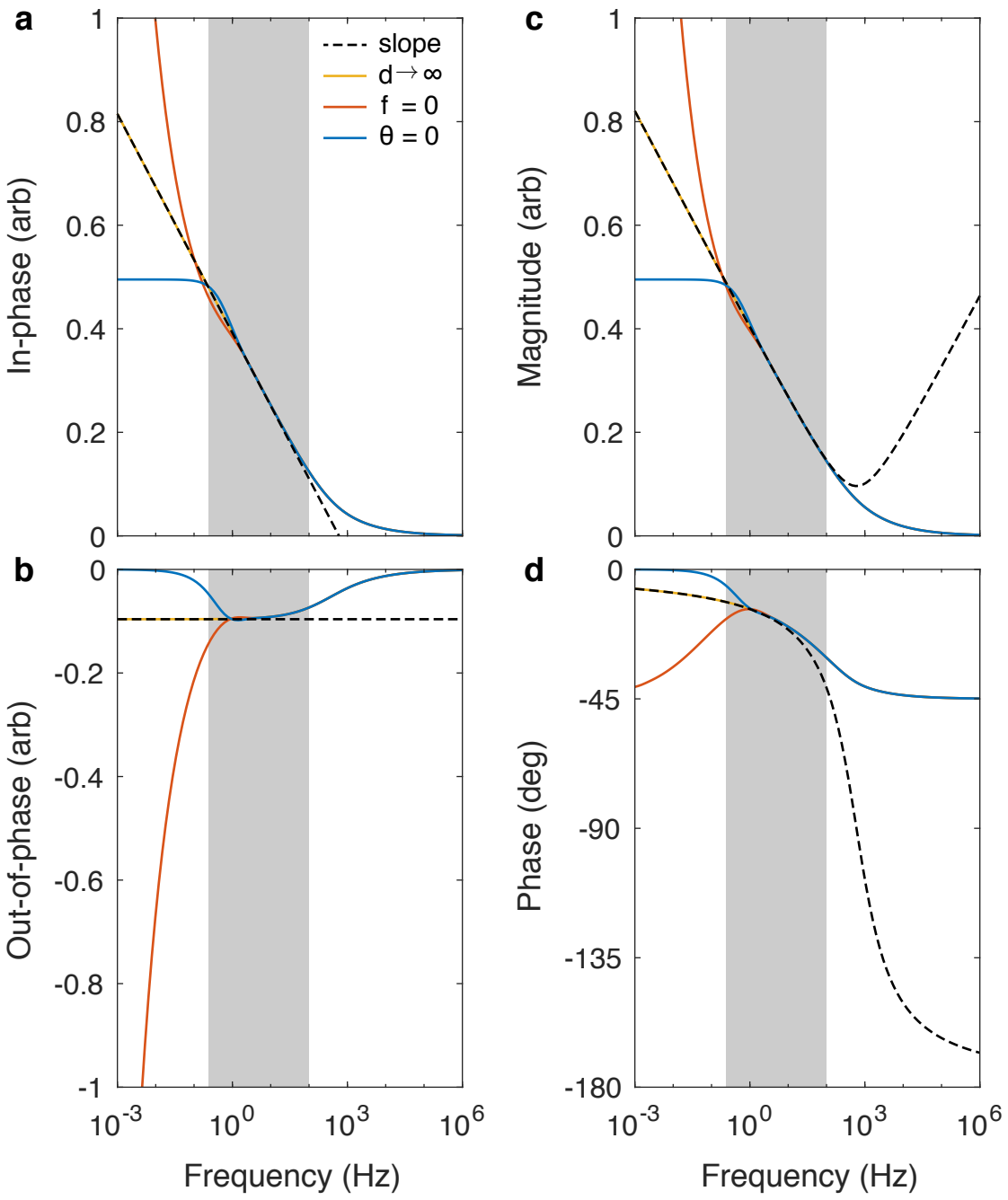

Figure 3.10: Simulated 3ω thermal signal for a 500 µm-thick fused silica substrate and a 50 µm-wide heater line, comparing the line-source model (slope method) to the multilayer model with semi-infinite ($d \rightarrow \infty$), adiabatic ($f = 0$), and isothermal ($\theta = 0$) boundary conditions. The (a) in-phase X, (b) out-of-phase Y, (c) magnitude R, and (d) phase Φ signals are the complex components of the thermal frequency response, $\Theta_2 = X + jY = R\exp(j\Phi)$. The shaded region indicates the frequency regime in which the slope method is valid.

where

$$A_{i-1} = \frac{\dfrac{A_i \kappa_i q_i}{\kappa_{i-1} q_{i-1}} - \tanh(q_{i-1} d_{i-1})}{1 - \dfrac{A_i \kappa_i q_i}{\kappa_{i-1} q_{i-1}} \tanh(q_{i-1} d_{i-1})} \tag{3.26}$$

$$q_i = \left(\lambda_i \xi^2 + j \frac{2\omega_0}{\alpha_i} \right)^{1/2} \tag{3.27}$$

for layers $i = 1 \ldots m$, starting from the layer in contact with the heater line. Here, Q_0 is the heat input at $2\omega_0$, L and b are the length and half-width of the line, d_i are the layer thicknesses, α_i and κ_i are the cross-plane thermal diffusivities and conductivities, and λ_i is the ratio of in-plane to cross-plane conductivities. Isothermal, adiabatic, or semi-infinite boundary conditions are enforced for the substrate, layer m, by setting

$$A_m = \begin{cases} -\dfrac{1}{\tanh(q_m d_m)} & \text{for} \quad \theta\big|_{d_m} = 0 \\ -\tanh(q_m d_m) & \text{for} \quad f\big|_{d_m} = 0 \\ -1 & \text{for} \quad d_m \gg q_m^{-1}, \end{cases} \tag{3.28}$$

respectively. Starting from A_m, we apply Eq. 3.26 iteratively to calculate A_1, which we use in Eq. 3.25 to get the temperature rise Θ_2.

To compare the slope method to the multilayer model, we plot simulated 3ω data for a 500 µm-thick fused silica substrate (Corning 7980 High Purity Fused Silica) measured with a 50 µm-wide heater line in Figure 3.10. We divide the thermal response into three frequency regimes, defined by how the penetration depth δ compares to the the heater line half-width b and the substrate thickness d. The threshold frequencies at which $\delta = b$ and $\delta = d$ are

$$\nu_b = \frac{\alpha}{4\pi b^2} \tag{3.29}$$

$$\nu_d = \frac{\alpha}{4\pi d^2}, \tag{3.30}$$

respectively. Using the thermal diffusivity of fused silica, $\alpha = 7.5 \times 10^{-7}\ \mathrm{m^2\,s^{-1}}$, we get $\nu_b = 95$ Hz and $\nu_d = 0.24$ Hz. The shaded region in Figure 3.10 corresponds to $\nu_d < \nu < \nu_b$ or $b < \delta < d$. Consistency between the line-source and multilayer models confirms the validity of the slope method in this frequency regime.

At higher frequencies, the penetration depth is less than the heater line half-width, $\delta < b$. The temperature profile transitions from axisymmetric to one-dimensional

as frequency increases, with thermal gradients aligning in the cross-plane direction. The multilayer model deviates from the line-source model, predicting that the thermal signal asymptotically approaches zero with a 45-degree phase lag.

At lower frequencies, the penetration depth is greater than the substrate thickness, $\delta > d$. In this case, the boundary condition imposed on the back of the substrate becomes important. With a semi-infinite boundary condition, the multilayer model matches the line-source model, ignoring the physical boundary of the substrate. With an adiabatic boundary condition, the thermal fluctuation diverges as frequency approaches zero. This behavior stems from the lack of a heat sink. Without a mechanism for heat transfer to the environment, the temperature of the system increases without bound. With an isothermal boundary condition, the signal magnitude plateaus to a steady in-phase value.

We assign a boundary condition according to the relative thermal conductivities and diffusivities of the substrate and the material on which it rests. If the substrate is mounted to a highly conductive thermal mass, then we use an isothermal boundary condition. If the substrate is suspended, then we use an adiabatic boundary condition. If the substrate has a complex geometry whose characteristic length is large compared to the penetration depth, then we use a semi-infinite boundary condition.

The accuracy of the model becomes questionable when the penetration depth is much larger than the substrate thickness, because transport behavior beyond the substrate will affect the measurement. Therefore, we restrict our measurement to $\nu > \nu_d$ such that the choice of boundary condition does not matter.

The line-source model or the multilayer model provide accurate descriptions of typical samples that consist of a slab or uniform film on a substrate with a metal heater line patterned on top [39, 71]. These well-established models assume negligible temperature gradients in the direction parallel to the line. As long as the voltage measurement points lie sufficiently far from the ends of the line, this assumption generally holds. As explained in Section 3.5, fabrication of a nanolattice that covers an entire substrate would take prohibitively long, so we build the structure only underneath the heater line.

The nanolattice sample geometry leads to non-negligible heat loss through the metal heater line. This occurs because the heater line connects to electrical contact pads that lie directly on the substrate, creating a secondary path for heat conduction. The nanolattice thermal conductivity is so low that despite the small cross-sectional

area of the metal line, the thermal resistance of the conduction path through the nanolattice is comparable to the thermal resistance through the metal line. Hence, we need to develop a new thermal model that incorporates heat conduction along the heater line.

The following equations describe heat conduction through our nanolattice sample during a 3ω experiment.

$$\frac{\partial^2\theta_i}{\partial y_i^2} + \lambda_i \frac{\partial^2\theta_i}{\partial z^2} - \frac{1}{\alpha_i}\frac{\partial\theta_i}{\partial t} = 0 \qquad \text{in} \quad 0 < y_i < d_i, \quad 0 < z < L \tag{3.31}$$

$$\frac{\kappa_1}{\kappa_0 d_0}\frac{\partial\theta_1}{\partial y_1} + \lambda_0 \frac{\partial^2\theta_0}{\partial z^2} - \frac{1}{\alpha_0}\frac{\partial\theta_0}{\partial t} = -\frac{g}{\kappa_0} e^{j\omega t} \qquad \text{on} \quad y_1 = 0 \tag{3.32}$$

$$\kappa_i \frac{\partial\theta_i}{\partial y_i} = \kappa_{i-1}\frac{\partial\theta_{i-1}}{\partial y_{i-1}} \qquad \text{on} \quad y_i = 0, \quad i = 2 \ldots m \tag{3.33}$$

$$\theta_i = \theta_{i-1} \qquad \text{on} \quad y_i = 0, \quad i = 1 \ldots m \tag{3.34}$$

$$\theta_m = 0 \qquad \text{on} \quad y_m = d_m \tag{3.35}$$

$$\theta_i = 0 \qquad \text{on} \quad z = 0, \quad z = L \tag{3.36}$$

In the equations above, z is the in-plane coordinate parallel to the heater line and y_i is the cross-plane coordinate, defined such that $y_i = d_i$ coincides with $y_{i+1} = 0$. Because the width of the heater line is identical to that of the nanolattice, we expect no temperature variation in the other in-plane direction x, perpendicular to the heater line. θ_i, κ_i, λ_i, α_i, and d_i denote the temperature, cross-plane thermal conductivity, ratio of in-plane to cross-plane thermal conductivity, cross-plane thermal diffusivity, and thickness of the i-th layer, where $i = 0$ corresponds to the heater line. Instead of a prescribed surface heat flux, we impose a boundary condition that describes a thin skin of highly conductive material that generates heat (Eq. 3.32) [72].

The general solution that satisfies the diffusion equation (Eq. 3.31) and isothermal boundary conditions in z (Eq. 3.36) can be expressed as a Fourier sine series. In layer i, the temperature and heat flux have the form

$$\theta_i = e^{j\omega t}\sum_{n=1}^{\infty}\theta_{in}\sin\frac{n\pi z}{L} \tag{3.37}$$

$$Q_i = e^{j\omega t}\sum_{n=1}^{\infty}Q_{in}\sin\frac{n\pi z}{L}, \tag{3.38}$$

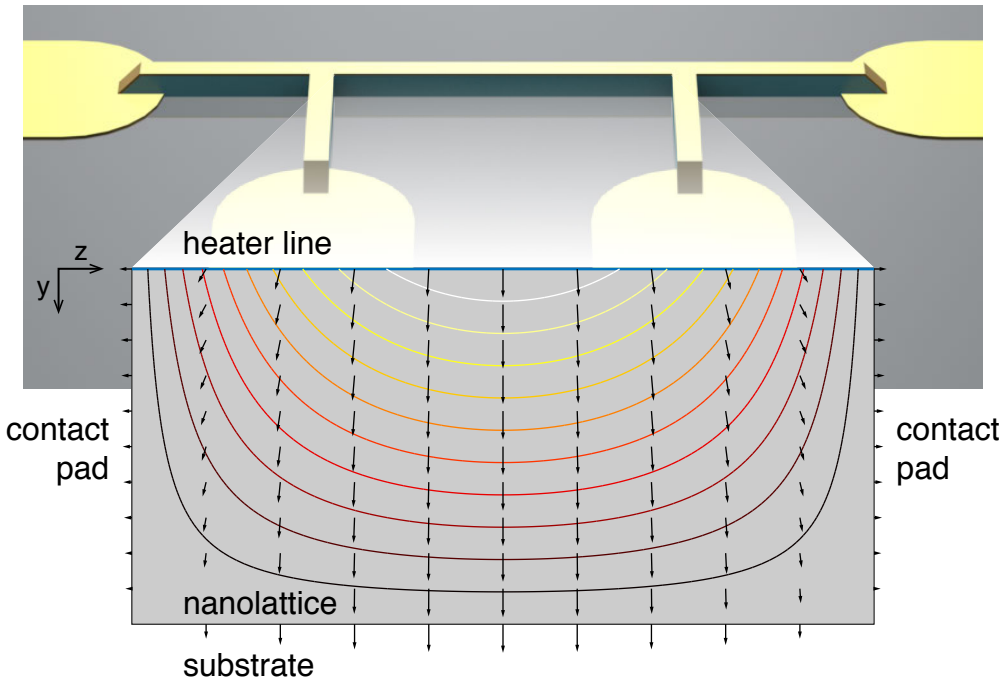

Figure 3.11: Temperature and heat flux fields in a nanolattice calculated using our custom nanolattice model. The top boundary represents the heater line as a thin skin of highly conductive material with heat generation. The left, right, and bottom boundaries represent the isothermal contact pads and substrate. The domain interior represents the nanolattice as a single layer in this simplified model. We include additional top plate and substrate layers above and below the nanolattice in the more accurate model used for 3ω data analysis.

where

$$\theta_{in} = (a_{in} \cosh q_{in} y_i + b_{in} \sinh q_{in} y_i) \tag{3.39}$$

$$Q_{in} = (a_{in} \sinh q_{in} y_i + b_{in} \cosh q_{in} y_i) \tag{3.40}$$

$$q_{in}^2 = \lambda_i \left(\frac{n\pi}{L}\right)^2 + \frac{j\omega}{\alpha_i}. \tag{3.41}$$

The constants a_{in} and b_{in} are chosen to satisfy the boundary conditions in y_i. These can be solved using the transfer matrix method [72],

$$\begin{pmatrix} \theta_{in} \\ Q_{in} \end{pmatrix}_{y_i \le d_i} = \begin{pmatrix} \cosh q_{in} y_i & -\frac{1}{\kappa_i q_{in}} \sinh q_{in} y_i \\ -\kappa_i q_{in} \sinh q_{in} y_i & \cosh q_{in} y_i \end{pmatrix} \begin{pmatrix} \theta_{in} \\ Q_{in} \end{pmatrix}_{y_i = 0}. \tag{3.42}$$

By enforcing continuity of temperature and heat flux across layers (Eqs. 3.33 and 3.34), we can compose m of these matrices to relate θ_{0n} and Q_{0n} at the heater line

to θ_{mn} and Q_{mn} at the isothermal surface.

$$\begin{aligned}\begin{pmatrix}\theta_{mn}\\ Q_{mn}\end{pmatrix}_{y_m=d_m} &= \begin{pmatrix}A_{mn} & B_{mn}\\ C_{mn} & D_{mn}\end{pmatrix}\cdots\begin{pmatrix}A_{1n} & B_{1n}\\ C_{1n} & D_{1n}\end{pmatrix}\begin{pmatrix}\theta_{1n}\\ Q_{1n}\end{pmatrix}_{y_1=0}\\ &= \begin{pmatrix}A_n & B_n\\ C_n & D_n\end{pmatrix}\begin{pmatrix}\theta_{1n}\\ Q_{1n}\end{pmatrix}_{y_1=0}\end{aligned} \tag{3.43}$$

Here, matrix elements are evaluated at $y_i = d_i$. The isothermal boundary condition $\theta_{mn} = 0$ (Eq. 3.35) thus implies

$$\theta_{1n} = -\frac{B_n}{A_n}Q_{1n} = \frac{\gamma_n}{\kappa_0 q_{0n}}Q_{1n}, \tag{3.44}$$

where we define the dimensionless quantity $\gamma_n = -\kappa_0 q_{0n} B_n/A_n$. The ratio B_n/A_n can be calculated using the algorithm given by Borca-Tasciuc et al. [70]. Finally, the heater line boundary condition is used to obtain a_{1n} and b_{1n}, giving

$$\theta_1 = \frac{g d_0^2}{\kappa_0} e^{j\omega t} \sum_{n\,\text{odd}} \frac{\gamma_n \cosh q_{1n}y_1 - \frac{\kappa_0 q_{0n}}{\kappa_1 q_{1n}} \sinh q_{1n}y_1}{(1+\gamma_n q_{0n} d_0)\, q_{0n} d_0} \left(\frac{4}{n\pi}\sin\frac{n\pi z}{L}\right) \tag{3.45}$$

$$Q_1 = g d_0 e^{j\omega t} \sum_{n\,\text{odd}} \frac{\cosh q_{1n}y_1 - \gamma_n \frac{\kappa_1 q_{1n}}{\kappa_0 q_{0n}} \sinh q_{1n}y_1}{1+\gamma_n q_{0n} d_0} \left(\frac{4}{n\pi}\sin\frac{n\pi z}{L}\right). \tag{3.46}$$

Note that the sum is evaluated only over odd natural numbers. Because hyperbolic cosine and sine grow rapidly, it is more numerically stable to evaluate the temperature and heat flux using exponentials. For example,

$$\theta_1 = \frac{g d_0^2}{\kappa_0} e^{j\omega t} \sum_{n\,\text{odd}} \frac{c_{1n} e^{q_{1n}y_1} + d_{1n} e^{-q_{1n}y_1}}{(1+\gamma_n q_{0n} d_0)\, q_{0n} d_0} \left(\frac{4}{n\pi}\sin\frac{n\pi z}{L}\right) \tag{3.47}$$

$$c_{1n} = \frac{1}{2}\left(\gamma_n - \frac{\kappa_0 q_{0n}}{\kappa_1 q_{1n}}\right) \tag{3.48}$$

$$d_{1n} = \frac{1}{2}\left(\gamma_n + \frac{\kappa_0 q_{0n}}{\kappa_1 q_{1n}}\right). \tag{3.49}$$

Figure 3.11 shows an example temperature and heat flux field for a single layer.

In the 3ω experiment, the measured voltage is directly related to the average heater line temperature, given by evaluating Eq. 3.45 at $y_1 = 0$ and integrating with respect to z. The resulting thermal frequency response is

$$\theta_\omega = \frac{g d_0^2}{\kappa_0} \sum_{n\,\text{odd}} \frac{8\gamma_n}{n^2\pi^2 (1+\gamma_n q_{0n} d_0)\, q_{0n} d_0}. \tag{3.50}$$

We select a thermal model—the line-source model, the standard multilayer model, or our custom nanolattice model—based on the sample and measurement conditions. For experimental validation on a glass substrate, we use the slope method because of its simplicity. For our room temperature measurements of polymer, alumina, and silicon nanolattices, both the multilayer and nanolattice models work well after normalizing the data or fitting a scaling factor. Low temperature experiments of nanolattices require the use of our custom model to accurately interpret the thermal response data.

3.7 Glass and polymer nanolattice measurements

Here, we present and analyze some preliminary 3ω results. We first show measurements of fused silica from 30 to 300 K to validate the experimental setup and data analysis approach described in previous sections. Then we look at polymer nanolattices with solid beams to observe their variation of thermal conductivity as a function of relative density. We perform these room temperature measurements in ambient air and in vacuum and confirm their consistency with finite element simulations.

We measured fused silica substrates (Corning 7980 High Purity Fused Silica) to validate our 3ω setup. Using a peak current of 20 mA, we observed temperature rises from 0.5 to 3 K at the heater line. Figure 3.12a shows an example thermal response curve taken at room temperature along with a nearly perfect model fit. We fit the experimental data in the 10 to 1000 Hz region using the multilayer model, with an overall scaling factor and the substrate thermal conductivity as the fitting parameters. In this frequency regime, we note that the slope method would also suffice. Figure 3.12b shows that the experimental results agree with handbook values [73] to within the experimental uncertainty.

Next, we measured polymer nanolattices with the octet-truss architecture. Five nanolattices with 25 µm unit cells and beam radii of 1.2, 1.6, 2.0, 2.4, and 2.8 µm were fabricated and tested in both air and vacuum environments at room temperature. Figure 3.13(a) depicts the thermal response of the lowest density structure (r = 1.2 µm) in vacuum, corresponding the lowest thermal conductivity measured in this batch of experiments, 9 mW m^{-1} K^{-1}. We notice a marked qualitative difference in the frequency response shape compared to fused silica. The signal magnitude drops steeply at low frequencies and more gradually above 10 Hz, coinciding with a rapid increase in phase lag that tails off at around the same threshold frequency.

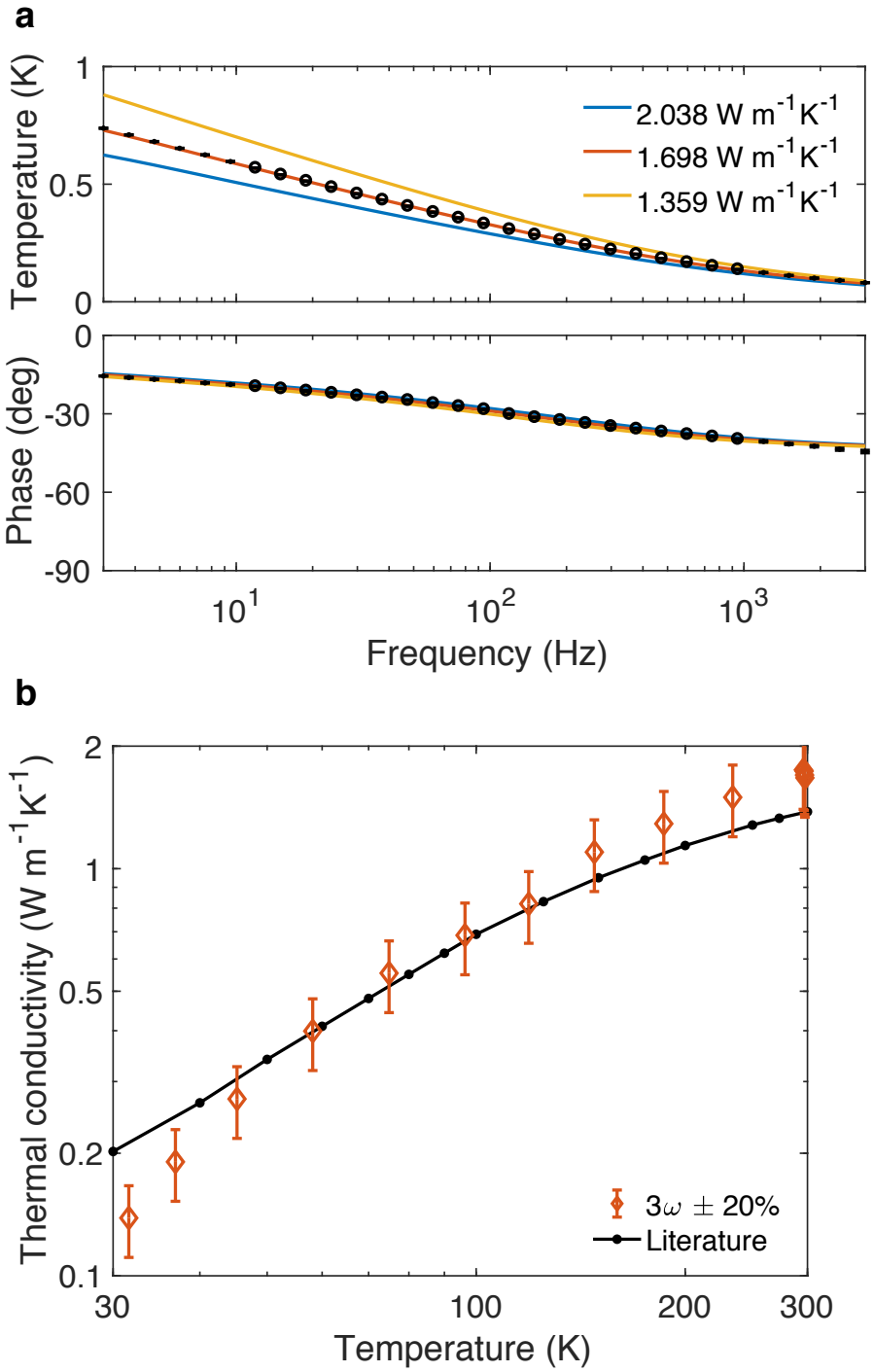

Figure 3.12: (a) 3ω temperature response of a fused silica glass substrate at room temperature. Markers denote experimental data, with open circles indicating the range of data used for model fitting. Lines are model-generated, with the middle curve representing the best fit and the other two curves showing 20 percent bounds. (b) Temperature-dependent thermal conductivity of fused silica glass measured by our 3ω setup, compared to literature values.

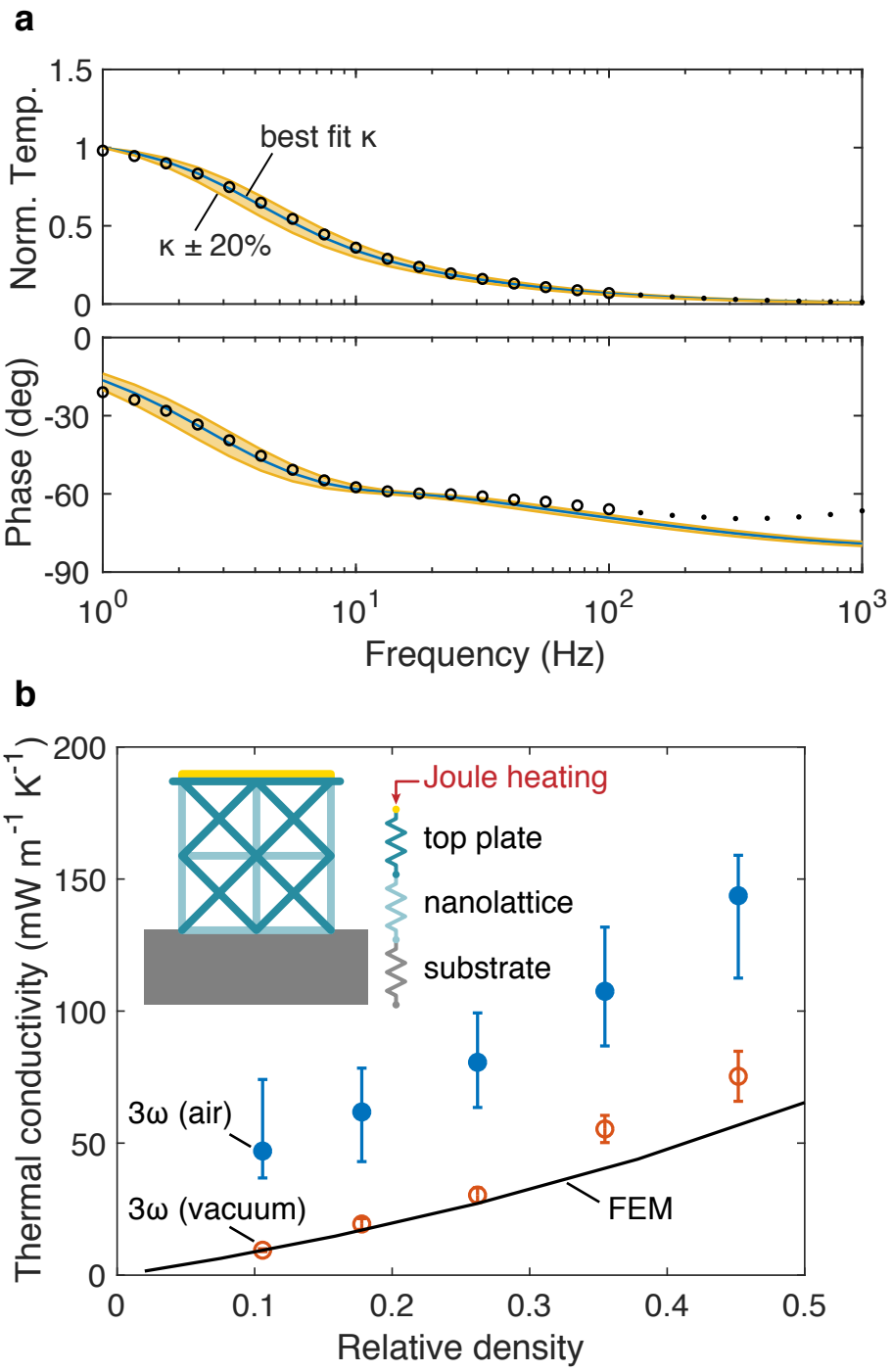

Figure 3.13: (a) Normalized 3ω temperature response for a polymer octet-truss nanolattice (markers), along with the best fit curve (center line) and ±20% bounds (shaded region). Data below 100 Hz (open circles) are used for fitting to a (b inset) standard multilayer model composed of top plate, nanolattice, and substrate layers. (b) Effective thermal conductivity versus relative density for polymer nanolattices. Thermal conductivities are measured using 3ω experiments in air (filled circles) and in vacuum (open circles), and calculated using finite element simulations (line).

We explain this data using a three layer model that accounts for the plate, the nanolattice, and the substrate. This model suggests that the ultralow thermal conductivity and heat capacity of the nanolattice are responsible for the thermal signal at low frequencies, with the top plate becoming more important at high frequencies. Since the multilayer model treats each layer as an effective medium, it cannot capture the geometric details of heat spreading from the top plate to the nanolattice beams, which becomes important when the penetration depth drops below the nanolattice height. Hence, we fit the 3ω data from 1 to 100 Hz to the model with a constant scaling factor and the nanolattice thermal conductivity as the only two fitting parameters. Vacuum measurements are in good agreements with the predictions of finite element simulations and the measurements performed in air are systematically higher, indicating the significant role of air conduction at ambient pressure.

The nanolattice measurements demonstrate that our 3ω approach works and produces expected results for diffusive transport in relatively high density structures. In the next chapter, we investigate hollow-beam alumina and silicon nanolattices with much lower densities and at lower temperatures, for which the predicted thermal conductivities are considerably lower.

Chapter 4

ULTRALOW THERMAL CONDUCTIVITY AND MECHANICAL RESILIENCE

This chapter has been adapted from: [1]

> Dou, N. G., Jagt, R. A., Portela, C. M., Greer, J. R. & Minnich, A. J. Ultralow thermal conductivity and mechanical resilience of architected nanolattices (in review).

Materials with low density, high elastic modulus, and low thermal conductivity are highly desirable for aerospace applications, as motivated in Chapter 1, but most materials cannot realize this combination of properties due to the correlation between these physical properties for both bulk and porous solids. Nanolattices have the potential to fill this gap in the property space by virtue of their hierarchical design [16] and nanoscale dimensions that decouple their thermal and mechanical properties [56]. In the thermal domain, relative density and intrinsic thermal transport properties of the constituent material control the effective thermal conductivity of nanolattices, as demonstrated in Chapter 3. The nanoscale features of hollow-beam nanolattices can increase boundary scattering of phonons and lower the thermal conductivity [50, 56] in materials that have phonons with long mean free paths, as shown in Chapter 2.

Here, we create low density hollow-beam nanolattices composed of alumina and silicon to observe the effect of relative density and architecture on their effective thermal conductivity at temperatures from 95 to 300 K. A comparison of the 3ω experiments with FEM simulations helps us draw conclusions about the nature of phonon transport in these alumina nanolattices. We also perform compression tests on the alumina nanolattices to test their mechanical resilience and demonstrate their viability as a multifunctional, structural thermal insulation material.

[1] N. G. D. built the 3ω experiment, conducted the thermal measurements, and developed the thermal model; R. A. J. fabricated samples and assisted with thermal measurements; C. M. P. performed the mechanical measurements; J. R. G. and A. J. M. provided technical guidance and supervision. All authors contributed to writing the paper.

4.1 Alumina nanolattice thermal conductivity

First, we consider hollow-beam alumina nanolattices. We measured thermal conductivity using the 3ω method [67] described in Section 3.2. Briefly, the method employs a microfabricated metal line as both a heater and a thermometer. A sinusoidal current applied through the heater line at frequency ω leads to Joule heating at 2ω, and the resulting temperature rise is deduced from the measured voltage across the line at 3ω.

We perform 3ω experiments in a ST-100 cryostat (Janis Research Co.) at temperatures from 95 to 300 K and pressures in the 10^{-6} torr range. A 6221 current source (Keithley Instruments) supplies power and an SR830 lock-in amplifier (Stanford Research Systems Inc.) measures voltages. In each experiment, we tune input power in the 4 to 40 μW range to ensure that the temperature rise at the heater line is less than 1 K. The thermal frequency response is measured from 1 to 1000 Hz by averaging 30 data points at each frequency. Additional details of our experimental setup and data collection procedure are provided in Sections 3.3 and 3.4.

To interpret the experimental data, we developed a custom thermal model described in Section 3.6. Our model accounts for lateral heat conduction through the gold heater line, one-dimensional heat conduction through the alumina plate, and two-dimensional heat conduction through the nanolattice and into the silicon substrate. The back side of the silicon chip is assumed to be isothermal. We use handbook values for density, specific heat, and thermal conductivity of silicon [73]. For amorphous alumina, we take the density to be 2900 kg m^{-3} [75] and the specific heat as the handbook value. The temperature-dependent thermal conductivity of bulk amorphous alumina is taken from measurements of RF-sputtered alumina [71]. The heat capacities and effective thermal conductivities of the plate and nanolattice are further scaled by the calculated relative densities of the respective structures. For the gold heater line, we use a density of 18 884 kg m^{-3} [76] and calculate thermal conductivity from electrical resistance via the Wiedemann-Franz law.

We extract thermal conductivity by performing a nonlinear least-squares fit on both the in-phase and out-of-phase components of the temperature response from 1 to 100 Hz. The thermal penetration depth is much longer than the height of the nanolattice in this low frequency range, implying that the entire nanolattice contributes to the temperature response and the experiment is sensitive to the effective thermal conductivity. The fitting parameters are nanolattice thermal conductivity and a constant normalization factor.

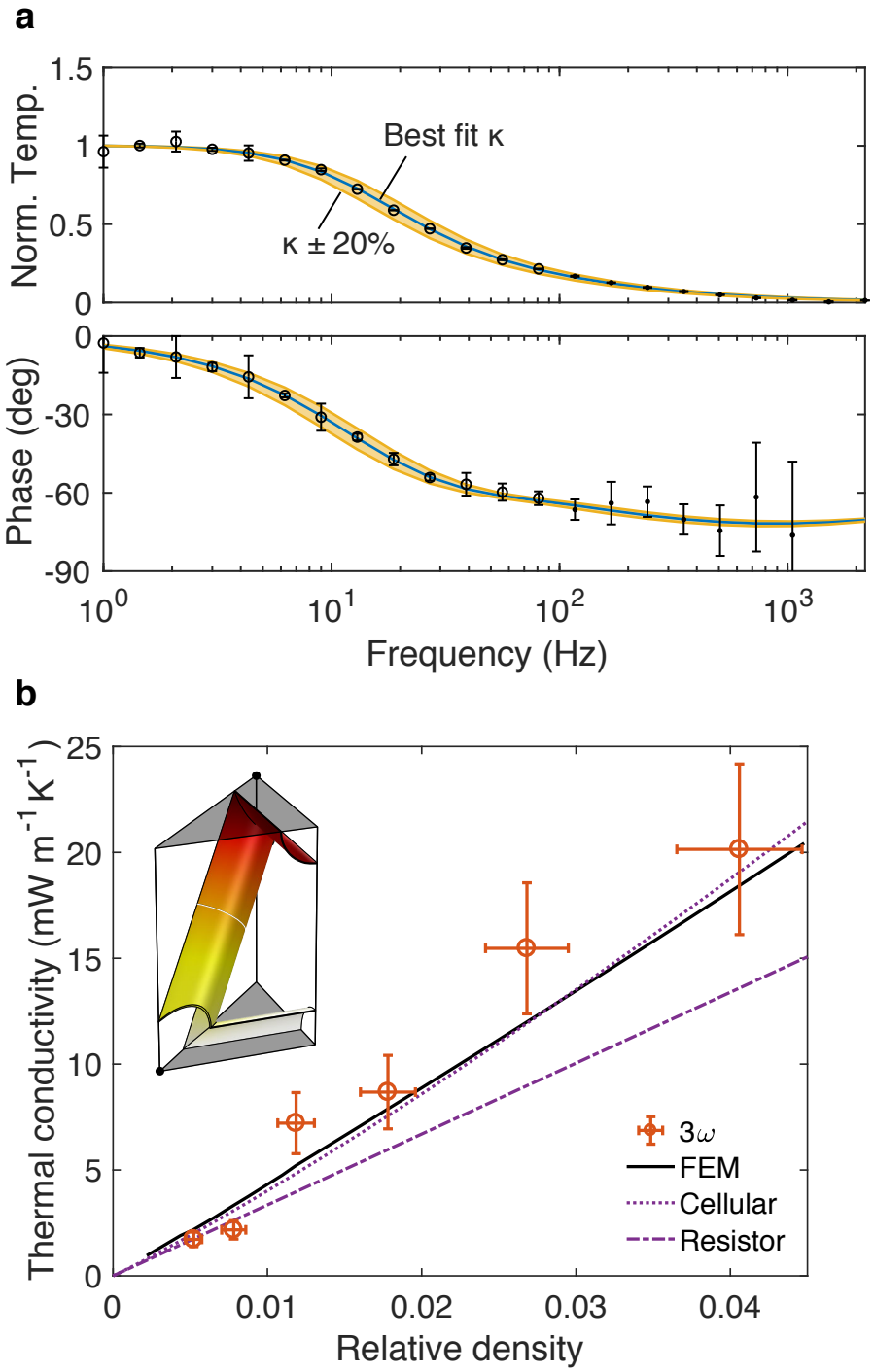

Figure 4.1: (a) Representative 3ω thermal response of the 81 nm wall thickness nanolattice along with the model-fitted curve and ±20% bounds. (b) Plot of room temperature thermal conductivity versus relative density depicting measured values, finite element simulations of a representative unit cell (inset), a thermal conductivity model developed for cellular solids [1], and our previous thermal resistance model [56].

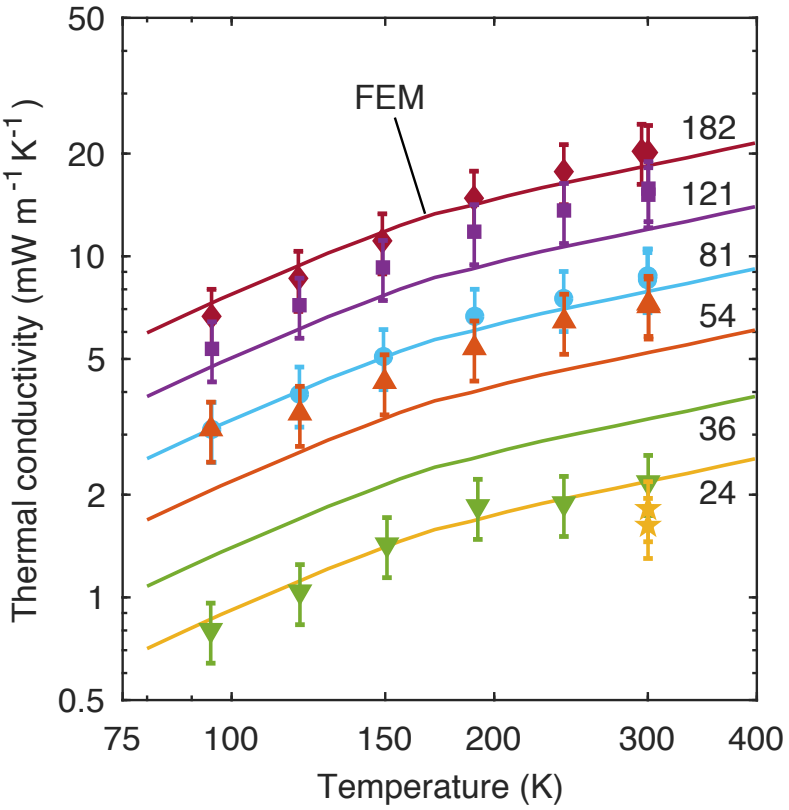

Figure 4.2: Measured thermal conductivity (symbols) versus temperature from 95 to 300 K, along with finite element predictions (lines). Good agreement between simulations and experiments indicates that heat conduction occurs by diffusion. Data sets are labeled by wall thickness (nm). Low temperature measurements of the 24 nm sample are not available.

We performed 3ω experiments for six hollow alumina nanolattices with octet-truss unit cells of side length 25 µm, circular beams of radius 1.8 µm, and wall thicknesses from 24 to 182 nm, which have relative densities ranging from 0.5 to 4%. Figure 4.1a shows the 3ω frequency response for the 81 nm wall thickness nanolattice at room temperature plotted with the best fit curve and model-generated curves for thermal conductivity deviations of ±20%, illustrating experimental sensitivity to the thermal conductivity of the nanolattice.

Room temperature thermal conductivities of six nanolattices are plotted against their relative density in Figure 4.1b. The 20% error bars reflect uncertainty from the fitting procedure, as well as uncertainty in the nanolattice dimensions caused by fabrication imperfections. Earlier work revealed that the ALD-deposited alumina is amorphous [69], so we expect the heat transport to occur by diffusion and the thermal

conductivity to follow classical effective medium theories. To test this hypothesis, we performed finite element method (FEM) simulations on the representative unit cell shown in the inset of Figure 4.1b using the thermal conductivity of amorphous alumina reported in literature [71]. The measured 3ω data are consistent with the predictions of FEM and a thermal conductivity model developed for cellular solids [1]. In the low-density regime, a simple thermal resistor model gives a reasonable approximation [56].

The temperature-dependent thermal conductivities are also in agreement with FEM simulations, as depicted in Figure 4.2. The thermal conductivities of these nanolattices have similar temperature dependence, which suggests that phonon transport occurs by diffusion and classical size effects are not significant. The observed diffusive transport behavior is consistent with the expectation that vibrational mean free paths are on the order of a few nanometers in amorphous alumina [77, 78].

4.2 Alumina nanolattice mechanical properties

Having proven that hollow-beam alumina nanolattices can achieve ultralow thermal conductivity, we now turn to their mechanical properties. As introduced in Chapter 1, we expect that lattice architecture and relative density set the effective elastic modulus of the material. For low densities ($\rho < 10\,\mathrm{kg\,m^{-3}}$), the stiffness of solid-beam nanolattices scales linearly with density for stretching-dominated architectures and quadratically for bending-dominated architectures [47, 79]. Hollow-beam nanolattices exhibit more complex mechanical behavior in which the architecture, beam-radius-to-length ratio r/l, and wall-thickness-to-beam-radius ratio t/r all play important roles in determining the stiffness, strength, and failure modes of the material [69]. At the nanoscale, appropriate values for these dimensional ratios can greatly improve the mechanical resilience of nanolattices. Recoverability after global deformation is enabled through a combination of elastic beam buckling, shell buckling, and micro-fracture at the nodes [80]. We do compression tests on hollow alumina nanolattices with identical geometries to those measured in the thermal experiments to confirm that their stiffnesses and deformation behavior match the properties reported in literature.

We performed uniaxial compression experiments on $5 \times 5 \times 5$ lattices to $\sim 50\%$ strain at a rate of $0.001\ \mathrm{s^{-1}}$ in a G200 XP Nanoindenter (Agilent Technologies). The Young's modulus was estimated by averaging the loading slopes of the stress-strain data of several identical samples. For the lowest density nanolattices (24 nm wall

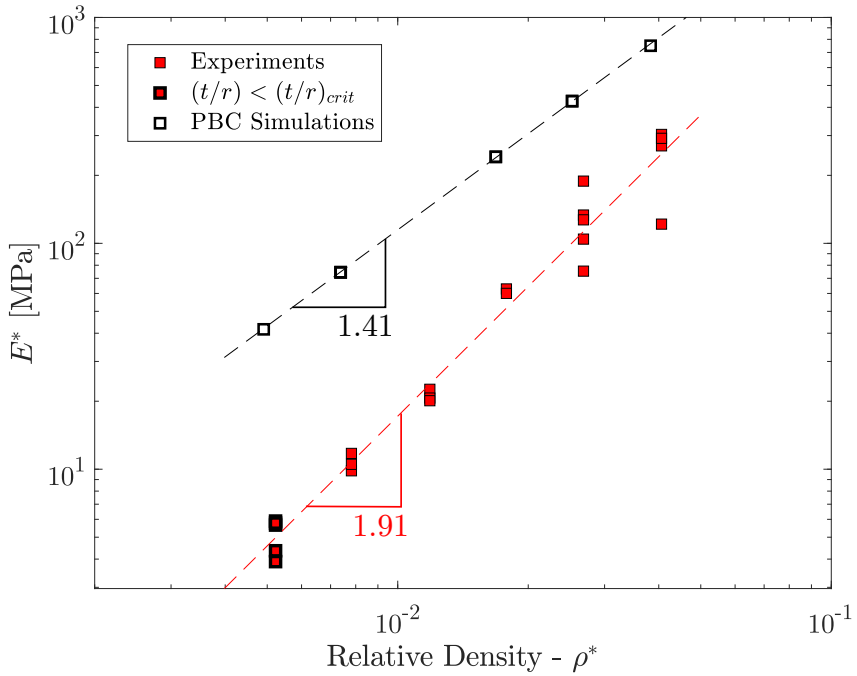

Figure 4.3: Experimental and computational stiffness values. The experiments where $t/r < (t/r)_{\text{crit}}$ are marked by a thicker black outline. Power-law fits of the form $E^* = ax^b$ for both experiments and simulations are shown as dotted lines. Due to imperfections in manufacturing, the experiments show a slightly higher scaling exponent b, and a vertical offset, in comparison to the simulations.

thickness, 0.5% relative density), we performed additional *in situ* experiments using an InSEM (Nanomechanics Inc.) nanoindenter, where cyclic loading to $\sim$ 20% strain allowed recoverability and deformation modes to be observed.

The uniaxial compression experiments provided stress-strain curves from which the Young's modulus of each nanolattice was calculated. Slight misalignments between the indenter tip and the top of the lattice commonly caused a non-linear regime upon first contact, followed by a linear loading regime, which transitioned into sequential or catastrophic failure, depending on the t/r ratio. In order to minimize the effects of initial misalignments between the lattices and the indenter, the maximum slope of the linear loading regime was taken as the measured Young's modulus.

Several identical samples were compressed for each set of parameters that were used for the thermal samples. Specifically, all samples had an r/l ratio of 0.108, t/r ratios from 0.013 to 0.10, and spanned a relative density range from 0.78 to 4.1 %.

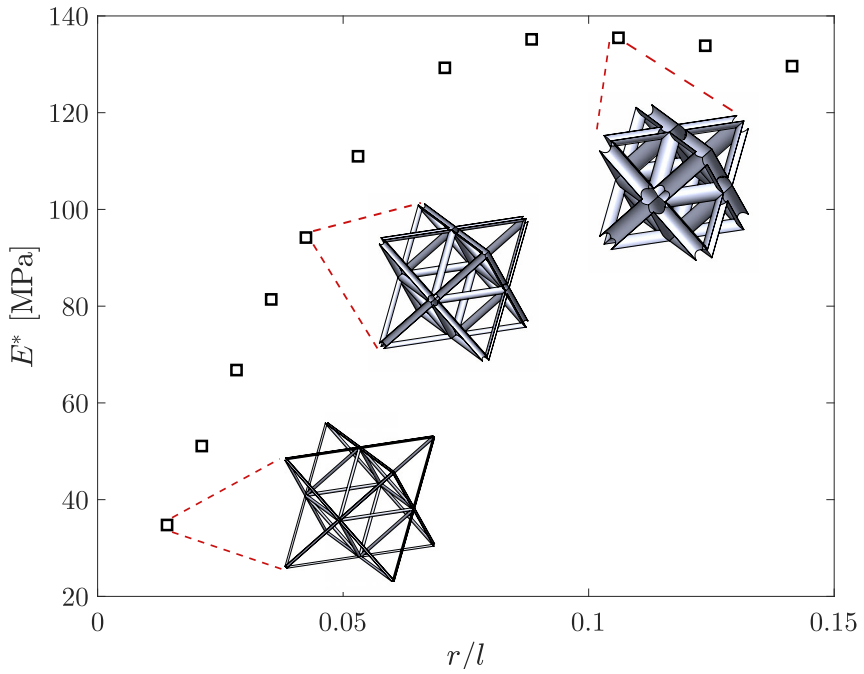

Figure 4.4: Periodic boundary condition simulations with a constant wall thickness but varying r/l, showing optimal values of r/l to maximize stiffness.

The relative density values were calculated using a CAD model (SolidWorks), using dimensions obtained from SEM micrographs. Figure 4.3 shows the stiffness values of all fabricated samples compared to finite element simulations with identical parameters (Abaqus FEA). The simulations consisted of a discretized octet-truss unit cell composed of S3R shell elements and a linear elastic material model, where the Young's modulus and Poisson's ratio of ALD alumina were used [81]. Periodic boundary conditions (PBC) were applied on all sides of the unit cell, and a uniaxial strain was enforced as a linear perturbation. The simulation size ranged from 110 000 to 310 000 elements depending on the r/l and t/r parameters used.

The power-law fits of the form $E^* = ax^b$ in Figure 4.3 yielded scaling constants $b = 1.41$ and 1.91 for simulations and experiments, respectively. The vertical offset and the higher scaling of the experimental samples in comparison to the defect-free simulations can be attributed to imperfections such as wall waviness (on the order of a few nanometers), which has been shown to significantly decrease the stiffness of thin-walled hollow beams [79]. The non-linear scaling is consistent with the analysis done in that work, where the complex parameter space of hollow nanolattices is explained.

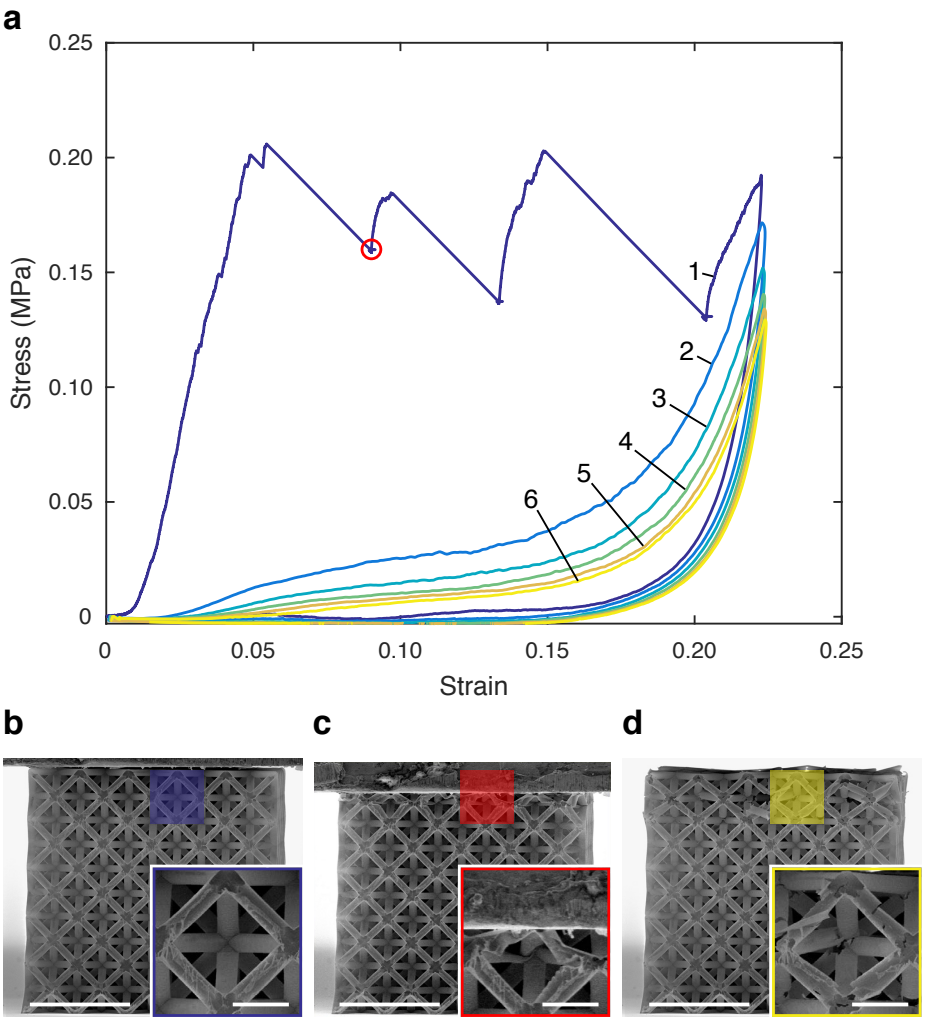

Figure 4.5: (A) Stress and strain recorded during a 6-cycle compression test of a 24 nm wall thickness nanolattice. Curves are labeled with the cycle number. SEM images (B) before, (C) during, and (D) after the test show 98% recovery. The circular marker indicates the stress and strain of the partially compressed nanolattice shown in (C). Zoomed images (insets) illustrate the contribution of beam buckling, shell buckling, and fracture. Scale bars are 50 nm for (B, C, D) and 10 nm for insets.

Prior to manufacturing the samples, PBC simulations with constant wall thickness and unit cell size but varying beam radius r were used to find an optimal r/l value at which the stiffness of circular-beam hollow octet-truss nanolattices was maximized. Figure 4.4 shows the resulting stiffness as r/l was varied from 0.014 to 0.14 and t/l remained at 0.007. The observed trend guided the design of the samples with $r/l \approx 0.1$.

Figure 4.5a depicts the stress-strain data for cyclic compression of a 24 nm wall

thickness nanolattice. Images of the structure before, during, and after the test are shown in Figure 4.5b, c, and d. After yielding, the nanolattice experiences bursts of strain that correspond to layer-by-layer collapse. This serrated deformation signature is characteristic of competing failure modes—brittle fracture of tube walls, hollow beam buckling, and local shell buckling [69]. The strain bursts are caused by non-catastrophic brittle fracture of the ceramic walls at nodes, while the mechanism of recoverable deformation is elastic shell buckling as shown in Figure 4.5C. This explanation for recoverability is further supported by adapting the analysis by Meza et al. [69] to circular hollow beams. The localization of cracks at the lattice nodes causes the stiffness of the nanolattices to significantly decrease throughout cyclic loading, but the structure still recovers to 98% of its original dimensions after each cycle. We expect that recoverable behavior can occur at strains as large as 50% [69], which was not probed in this work.

Following the analysis done by Meza et al. [69], the dominating deformation modes for circular cross-section hollow nanolattices can be estimated. The three modes to be considered are material fracture, beam buckling, and shell buckling. The critical stress values for each mode are

$$\sigma_{\text{frac}} = \sigma_f, \tag{4.1}$$

$$\sigma_{\text{buckle}} = \frac{\pi^2 E I}{L_e^2 A_{\text{tube}}}, \tag{4.2}$$

$$\sigma_{\text{shell}} = \frac{E}{\sqrt{3(1-\nu^2)}}\left(\frac{t}{r_c}\right), \tag{4.3}$$

respectively. Here, σ_f is the fracture strength, E is the Young's modulus, and ν is the Poisson's ratio of the constituent material. The cross-sectional area of the tube is denoted as A_{tube}, its second area moment is I, and its effective length is L_e (depending on the boundary conditions). In the case of the octet-truss architecture, $L_e = L/2$, where L is the actual length of the tube. The quantities t and r_c refer to the wall thickness and the wall's radius of curvature, respectively. For a circular hollow tube, $r_c = r$, where r is the tube radius.

Approximating the second area moment to $I = \pi r^3$ and the cross-sectional area to $A_{\text{tube}} = \pi r t$, setting $\sigma_{\text{buckle}} = \sigma_{\text{frac}}$ and $\sigma_{\text{shell}} = \sigma_{\text{frac}}$, and solving for r/l and t/r

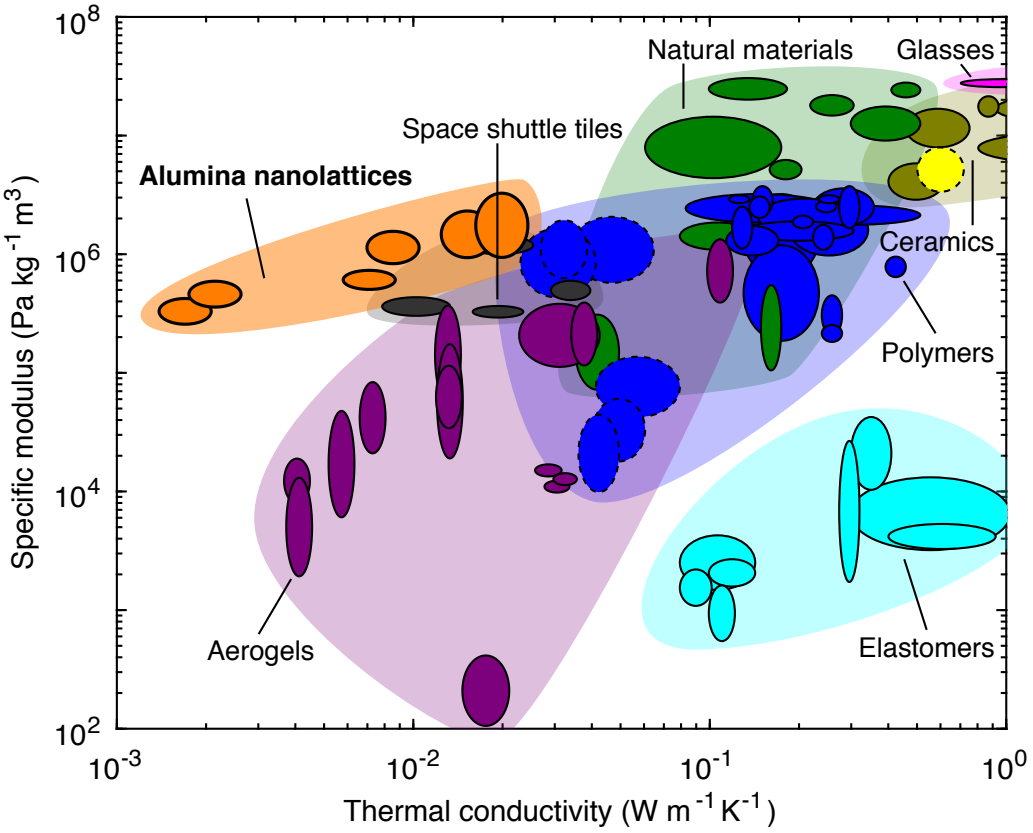

Figure 4.6: Material property plot of specific modulus versus thermal conductivity. Dashed outlines indicate foams. For the same specific stiffness, our results demonstrate that nanolattices can achieve an order of magnitude lower thermal conductivity than polymer foams and porous ceramics used for space shuttle thermal protection systems. For the same thermal conductivity, nanolattices have almost two orders of magnitude higher specific stiffness than evacuated aerogels.

yields

$$\left(\frac{r}{l}\right)_{\text{crit}} = \frac{1}{2\pi}\sqrt{\frac{\sigma_f}{E}}, \tag{4.4}$$

$$\left(\frac{t}{r}\right)_{\text{crit}} = \frac{\sigma_f}{E}\sqrt{3(1-\nu^2)}, \tag{4.5}$$

where $(r/l)_{\text{crit}}$ and $(t/r)_{\text{crit}}$ are the critical ratios below which elastic Euler buckling and elastic shell buckling are expected to dominate over material fracture, respectively.

4.3 Alumina nanolattice multifunctional performance

We examine the multifunctional performance of these hollow-beam alumina nanolattices on a plot of specific elastic modulus versus thermal conductivity, shown

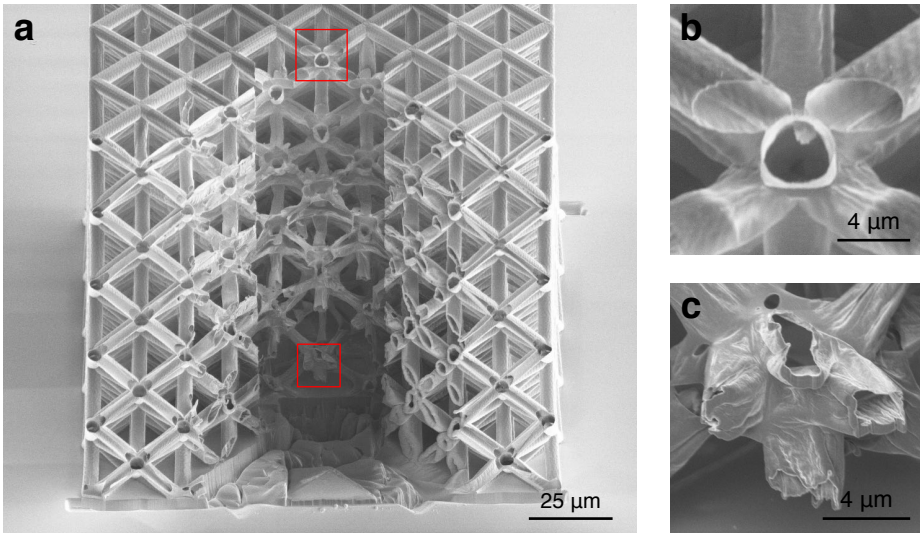

Figure 4.7: (a) Focused ion beam cross-section of a hollow silicon nanolattice. Zoomed-in views of (b) top beams close to the outer surface and (c) bottom beams furthest from the surface show a dramatic difference in deposition quality. Panels (b) and (c) correspond to the upper and lower squares in panel (a), respectively.

in Figure 4.6. The nanolattices have comparable or lower thermal conductivity than aerogels while achieving specific moduli up to two orders of magnitude higher. Compared to the porous ceramics used for spacecraft thermal protection systems, nanolattices have a similar specific modulus but almost an order of magnitude lower thermal conductivity. Most aerogels also experience catastrophic failure under modest mechanical loads, while alumina nanolattices exhibit recoverability and ductile-like deformation behavior, especially low-density structures that have the lowest thermal conductivities. The nanolattices provide the added benefit of tunable mechanical properties, which can be decoupled from thermal properties by fixing the relative density and changing the characteristic ratios r/l and t/r.

Our experiments demonstrate that hollow alumina nanolattices simultaneously achieve ultralow thermal conductivity, high specific stiffness, and the ability to recover from large compressive strains by exploiting architecture and nanoscale feature sizes. A wider range of physical properties are attainable by modifying the lattice architecture, structural dimensions, and constituent material. Next, we investigate whether we can further decrease thermal conductivity by creating silicon nanolattices.

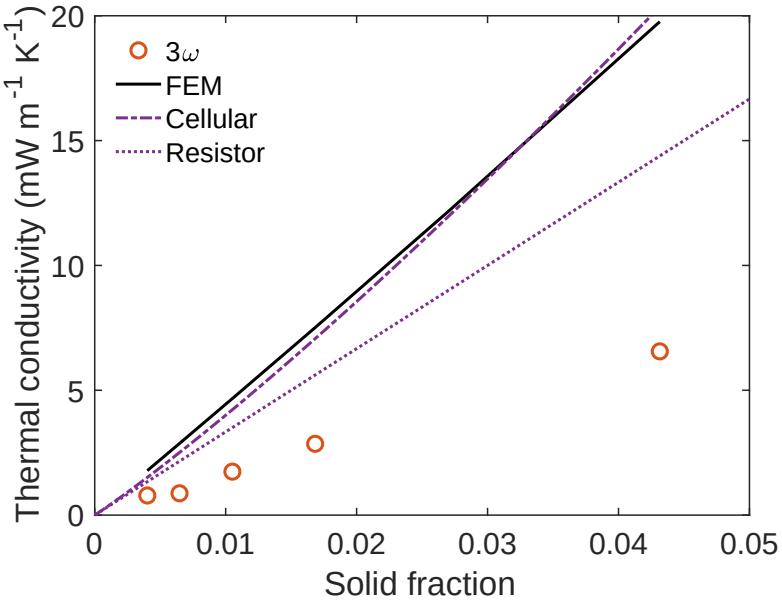

Figure 4.8: Nanolattice thermal conductivity versus nominal solid fraction at room temperature and in vacuum. Poor structural quality is likely a major cause of the large discrepancy between experimental measurements and model predictions.

4.4 Silicon nanolattice thermal conductivity

Given that our Monte Carlo simulations in Section 2.7 show the importance of phonon size effects in silicon nanolattices, we want to experimentally corroborate that observation. To that end, we fabricate hollow octet-truss nanolattices composed of amorphous silicon by coating the lattice scaffold using plasma-enhanced chemical vapor deposition (PECVD). Unlike atomic layer deposition (ALD), which adds a consistent and conformal layer of material to the deposited film during every self-limiting cycle, PECVD grows the film continuously in a non-uniform manner that depends on the transport of precursor to the deposition location. By taking a focused ion beam cross-section through the middle of a $5\times5\times5$ structure, shown in Fig. 4.7a, we see a striking variation of deposition quality from the surface to the middle of the structure. While the upper beams in panel b look normal, the lower beams in panel c have deep wrinkles and holes.

Despite the poor structural quality of the silicon nanolattices, we took 3ω measurements at room temperature and in vacuum of 5 samples with unit cell widths of 25 µm, beam radii of 2 µm, and nominal silicon thicknesses of 18, 29, 47, 75, and 192 nm. Fig. 4.7d plots nanolattice thermal conductivity versus nominal relative density. The experimental data lie about a factor of 3 below the finite element pre-

dictions for the ideal structures assuming a-Si thermal conductivity of 1 $\mathrm{W\,m^{-1}\,K^{-1}}$. If we characterized the true relative densities of the nanolattice samples, the 3ω data would likely shift leftward, and if we incorporate wall thickness variations into the finite element model, the simulation predictions would probably shift downward because of heat spreading to regions of higher density. The severe structural defects prevent us from confirming or denying the existence of size effects.

Demonstration of phonon size effects requires the synthesis and characterization of nanolattices with higher structural quality and known or measurable dimensions. Only then can we accurately model its thermal behavior and isolate size effects by comparing measurements with diffusion theory predictions, as we do for our Monte Carlo simulations in Section 2.7.

Chapter 5

SUMMARY AND OUTLOOK

In this work, we developed a framework for computationally and experimentally studying thermal transport in architected materials with a range of length scales from nanometers to millimeters. Significant modifications to existing techniques allowed us to extend their range of applicability to multi-scale structures. We applied these techniques to polymer, ceramic, and semiconductor nanolattices with the octet architecture, showing that they can achieve ultralow thermal conductivity. We further demonstrated that the ceramic nanolattices have excellent mechanical stiffness and resilience, thus achieving a combination of thermo-mechanical properties never before realized in a single material. Here, we summarize our key contributions and identify several directions for further exploration that could push the boundaries of the currently accessible material property space.

Monte Carlo methods for phonon transport simulation enable numerical solutions of the Boltzmann transport equation in geometries that are not conducive to analytical solutions, but no prior research has studied a structure nearly as complex as a nanolattice. We designed and implemented a general geometry representation scheme to facilitate efficient simulation of the highly complex computational domain. Based on the results of our Monte Carlo and finite element method simulations, we decoupled the contributions of diffusion and classical size effects to create a simple yet powerful model for the prediction of effective thermal conductivity. This model can be applied to any nanoarchitected material with a shell structure whose wall thickness represents the primary length scale of phonon confinement. More generally, our method can elucidate how interfaces—free boundaries, grain boundaries, or material boundaries—affect phonon transport in any three-dimensional nanostructure that satisfies the assumptions of the linearized BTE with the relaxation time approximation. With ab initio phonon dispersions and lifetimes as inputs, our method can calculate detailed and accurate information about the mode-dependent transport behavior in an arbitrary structure [82].

The 3ω method has been widely used to measure the thermal properties of solids, thin films, liquids, suspended wires, and suspended membranes, but their application to nanolattices is not straightfoward. We designed and fabricated a specialized 3ω

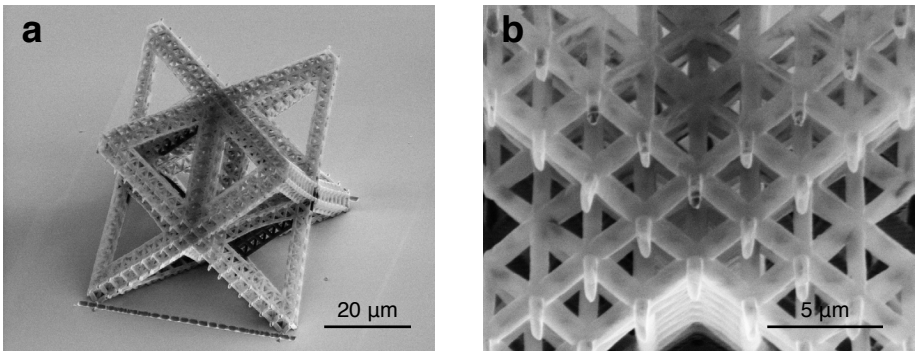

Figure 5.1: (a) Hollow alumina nanolattice with the hierarchical octet-of-octets architecture. (b) Zoomed-in view of a higher-order node, showing sacrificial beams through which polymer is etched out.

sample for which we deposit the metal heater line on top of a bridge-like nanolattice structure, allowing us to obtain the best possible sensitivity with the least volume of nanolattice. Since heat conduction through the metal line becomes significant in this configuration, we developed a custom thermal model to account for two-dimensional heat conduction in the cross-plane direction and in-plane direction parallel to the line. We measured the ultralow thermal conductivity of alumina nanolattices with the strategy, finding good agreement with diffusive transport predictions at room temperature and below. Our sample design and model are applicable to other microscale structures created by additive manufacturing techniques.

The nanolattice fabrication process allows us to modify structural dimensions, lattice architecture, and constituent material with relative ease. Our study barely scratches the surface of the design space. Additional investigation into the thermal properties of nanoarchitected materials would undoubtedly expand the accessible region of material property space.

Fractal nanolattices with additional orders of hierarchy could offer even lower thermal conductivities than first-order nanolattices. These hierarchical lattices distribute mechanical load more efficiently among their beams, leading to stiffness and strength scalings that approach the theoretical ideal [80]. We do not expect solid-polymer or hollow-ceramic hierarchical nanolattices to exhibit phonon size effects, but even in the diffusive regime, their significantly lower relative density would result in proportionally lower effective thermal conductivity. This strategy would reach lower thermal conductivities without compromising specific stiffness.

Another approach for lowering thermal conductivity involves alternately coat-

ing different materials onto the nanolattice to create multi-layered beam walls with an annular superlattice structure. The contrast in atomic or molecular weights across material interfaces could increase phonon interfacial scattering [83], thus suppressing thermal conductivity for higher relative density structures. Since relative density would likely affect mechanical properties more than interface density, we expect these lattices to have higher stiffness and strength commensurate with their mass density. This strategy would reach higher specific stiffnesses for the same ultralow thermal conductivities.

These ideas would presumably yield substantial improvements in material properties, but our work suggests that manipulation of architecture at the microscale would not affect the intrinsic phonon transport behavior. Therefore, combining diffusion theory with simple models for phonon size effects, such as Fuchs-Sondheimer theory, should adequately describe the transport behavior of most architected materials.

Although we have answered some important questions regarding heat conduction in nanolattices, many more issues must be addressed before architected materials can be applied in real thermal engineering applications. On the mechanical side, experiments that can measure the tensile, shear, and fracture properties are needed and additional in-depth characterization and modeling are desired [46]. On the thermal side, we did not consider the contributions of gas conduction and radiation, which become important in many common situations. In high temperature applications, for example, radiation could even dominate. As shown for aerogels, radiation can be mitigated by adding opacifiers to increase absorption [30] and gaseous conductivity can be reduced if pore sizes are comparable to the mean free path of gas molecules [18]. Pyrolysis is one avenue for obtaining smaller feature sizes which has been successfully demonstrated for nanolattices [84].

Scalability remains the biggest roadblock to real-world application of nanolattices. The first thermal applications of nanolattices might be small-scale, small-batch aerospace components which require customizability and extreme thermal and mechanical properties. Efforts to increase production involve parallel exposure via phase-mask lithography [85] or interference lithography [86]. If large-scale manufacturing can be achieved, nanolattices could replace aerogels as the premier thermal insulation material.

BIBLIOGRAPHY

1. Ashby, M. F. The properties of foams and lattices. en. *Philosophical Transactions of the Royal Society of London A: Mathematical, Physical and Engineering Sciences* **364,** 15–30. ISSN: 1364-503X, 1471-2962 (Jan. 2006).
2. Finckenor, M. M. *Materials for Spacecraft* in *Aerospace Materials and Applications* chap. 6 (Jan. 2016).
3. Henson, G. & Jone, C. S. I. *Materials for Launch Vehicle Structures* in *Aerospace Materials and Applications* chap. 7 (Feb. 2017).
4. Mouritz, A. P. *Introduction to aerospace materials* ISBN: 978-0-85709-515-2 (Elsevier, May 2012).
5. Heydenreich, R. Cryotanks in future vehicles. *Cryogenics* **38,** 125–130. ISSN: 0011-2275 (Jan. 1998).
6. Glass, D. *Ceramic Matrix Composite (CMC) Thermal Protection Systems (TPS) and Hot Structures for Hypersonic Vehicles* in *15th AIAA International Space Planes and Hypersonic Systems and Technologies Conference* (American Institute of Aeronautics and Astronautics, 2008). doi:10.2514/6.2008-2682.
7. Gibson, L. J. & Ashby, M. F. *Cellular Solids: Structure and Properties* ISBN: 978-0-521-49911-8 (Cambridge University Press, July 1999).
8. Gibson, L. J., Ashby, M. F. & S, F. R. The mechanics of three-dimensional cellular materials. *Proc. R. Soc. Lond. A* **382,** 43–59. ISSN: 0080-4630, 2053-9169 (July 1982).
9. Garnett, J. C. M. Colours in Metal Glasses and in Metallic Films. *Philosophical Transactions of the Royal Society of London A: Mathematical, Physical and Engineering Sciences* **203,** 385–420. ISSN: 0264-3952 (Jan. 1904).
10. Bruggeman, D. a. G. Berechnung verschiedener physikalischer Konstanten von heterogenen Substanzen. I. Dielektrizitätskonstanten und Leitfähigkeiten der Mischkörper aus isotropen Substanzen. *Annalen der Physik* **416,** 636–664. ISSN: 1521-3889 (Jan. 1935).
11. Hashin, Z. & Shtrikman, S. A Variational Approach to the Theory of the Effective Magnetic Permeability of Multiphase Materials. *Journal of Applied Physics* **33,** 3125–3131. ISSN: 0021-8979, 1089-7550 (Oct. 1962).
12. Landauer, R. The Electrical Resistance of Binary Metallic Mixtures. *Journal of Applied Physics* **23,** 779–784. ISSN: 0021-8979, 1089-7550 (July 1952).
13. Costescu, R. M., Bullen, A. J., Matamis, G., O'Hara, K. E. & Cahill, D. G. Thermal conductivity and sound velocities of hydrogen-silsesquioxane low-k dielectrics. *Physical Review B* **65,** 094205 (Feb. 2002).

14. Carson, J. K., Lovatt, S. J., Tanner, D. J. & Cleland, A. C. Thermal conductivity bounds for isotropic, porous materials. *International Journal of Heat and Mass Transfer* **48,** 2150–2158. ISSN: 0017-9310 (May 2005).

15. Tillotson, T. M. & Hrubesh, L. W. Transparent ultralow-density silica aerogels prepared by a two-step sol-gel process. *Journal of Non-Crystalline Solids* **145,** 44–50. ISSN: 0022-3093 (Jan. 1992).

16. Schaedler, T. A. *et al.* Ultralight Metallic Microlattices. en. *Science* **334,** 962–965. ISSN: 0036-8075, 1095-9203 (Nov. 2011).

17. Kistler, S. S. The Relation between Heat Conductivity and Structure in Silica Aerogel. *The Journal of Physical Chemistry* **39,** 79–86. ISSN: 0092-7325 (Jan. 1934).

18. Fricke, J., Lu, X., Wang, P., Buttner, D. & Heinemann, U. Optimization of monolithic silica aerogel insulants. *International Journal of Heat and Mass Transfer* **35,** 2305–2309. ISSN: 0017-9310 (Sept. 1992).

19. Lu, X. *et al.* Thermal Conductivity of Monolithic Organic Aerogels. en. *Science* **255,** 971–972. ISSN: 0036-8075, 1095-9203 (Feb. 1992).

20. Gross, J., Reichenauer, G. & Fricke, J. Mechanical properties of SiO2 aerogels. en. *Journal of Physics D: Applied Physics* **21,** 1447. ISSN: 0022-3727 (Sept. 1988).

21. Woignier, T. & Phalippou, J. Mechanical strength of silica aerogels. *Journal of Non-Crystalline Solids. Glasses and Glass Ceramics from Gels* **100,** 404–408. ISSN: 0022-3093 (Mar. 1988).

22. Gross, J. & Fricke, J. Scaling of elastic properties in highly porous nanostructured aerogels. *Nanostructured Materials. Proceedings of the Second International Conference on Nanostructured Materials* **6,** 905–908. ISSN: 0965-9773 (Jan. 1995).

23. Hæreid, S., Anderson, J., Einarsrud, M. A., Hua, D. W. & Smith, D. M. Thermal and temporal aging of TMOS-based aerogel precursors in water. *Journal of Non-Crystalline Solids* **185,** 221–226. ISSN: 0022-3093 (June 1995).

24. Martin, J., Hosticka, B., Lattimer, C. & Norris, P. M. Mechanical and acoustical properties as a function of PEG concentration in macroporous silica gels. *Journal of Non-Crystalline Solids* **285,** 222–229. ISSN: 0022-3093 (June 2001).

25. Wei, T.-Y., Lu, S.-Y. & Chang, Y.-C. Transparent, Hydrophobic Composite Aerogels with High Mechanical Strength and Low High-Temperature Thermal Conductivities. *The Journal of Physical Chemistry B* **112,** 11881–11886. ISSN: 1520-6106 (Sept. 2008).

26. Randall, J. P., Meador, M. A. B. & Jana, S. C. Tailoring Mechanical Properties of Aerogels for Aerospace Applications. *ACS Applied Materials & Interfaces* **3,** 613–626. ISSN: 1944-8244 (Mar. 2011).

27. Katti, A. *et al.* Chemical, Physical, and Mechanical Characterization of Isocyanate Cross-linked Amine-Modified Silica Aerogels. *Chemistry of Materials* **18,** 285–296. ISSN: 0897-4756 (Jan. 2006).

28. Lu, X., Nilsson, O., Fricke, J. & Pekala, R. W. Thermal and electrical conductivity of monolithic carbon aerogels. *Journal of Applied Physics* **73,** 581–584. ISSN: 0021-8979 (Jan. 1993).

29. Pekala, R. W., Alviso, C. T. & LeMay, J. D. Organic aerogels: microstructural dependence of mechanical properties in compression. *Journal of Non-Crystalline Solids* **125,** 67–75. ISSN: 0022-3093 (Nov. 1990).

30. Lee, D., Stevens, P. C., Zeng, S. Q. & Hunt, A. J. Thermal characterization of carbon-opacified silica aerogels. *Journal of Non-Crystalline Solids. Proceedings of the Fourth International Symposium on AEROGELS* **186,** 285–290. ISSN: 0022-3093 (June 1995).

31. Blanco, A. *et al.* Large-scale synthesis of a silicon photonic crystal with a complete three-dimensional bandgap near 1.5 micrometres. en. *Nature* **405,** 35013024. ISSN: 1476-4687 (May 2000).

32. Vlasov, Y. A., Bo, X.-Z., Sturm, J. C. & Norris, D. J. On-chip natural assembly of silicon photonic bandgap crystals. en. *Nature* **414,** 289–293. ISSN: 0028-0836 (Nov. 2001).

33. Scott, R. W. J. *et al.* Tin Dioxide Opals and Inverted Opals: Near-Ideal Microstructures for Gas Sensors. en. *Advanced Materials* **13,** 1468–1472. ISSN: 1521-4095 (Oct. 2001).

34. Chen, J. I. L., von Freymann, G., Choi, S. Y., Kitaev, V. & Ozin, G. A. Amplified Photochemistry with Slow Photons. en. *Advanced Materials* **18,** 1915–1919. ISSN: 1521-4095 (July 2006).

35. Esmanski, A. & Ozin, G. A. Silicon Inverse-Opal-Based Macroporous Materials as Negative Electrodes for Lithium Ion Batteries. en. *Advanced Functional Materials* **19,** 1999–2010. ISSN: 1616-3028 (June 2009).

36. Choi, S.-W., Xie, J. & Xia, Y. Chitosan-Based Inverse Opals: Three-Dimensional Scaffolds with Uniform Pore Structures for Cell Culture. en. *Advanced Materials* **21,** 2997–3001. ISSN: 1521-4095 (Aug. 2009).

37. Stein, A., Wilson, B. E. & Rudisill, S. G. Design and functionality of colloidal-crystal-templated materials—chemical applications of inverse opals. en. *Chemical Society Reviews* **42,** 2763–2803 (2013).

38. Ma, J. & Sinha, S. Thermoelectric properties of highly doped n-type polysilicon inverse opals. *Journal of Applied Physics* **112,** 073719. ISSN: 0021-8979, 1089-7550 (Oct. 2012).

39. Ma, J. *et al.* Coherent Phonon-Grain Boundary Scattering in Silicon Inverse Opals. *Nano Letters* **13,** 618–624. ISSN: 1530-6984 (Feb. 2013).

40. Pikul, J. H. *et al.* Micromechanical devices with controllable stiffness fabricated from regular 3D porous materials. en. *Journal of Micromechanics and Microengineering* **24,** 105006. ISSN: 0960-1317 (2014).

41. Maxwell, J. C. On the calculation of the equilibrium and stiffness of frames. *The London, Edinburgh, and Dublin Philosophical Magazine and Journal of Science* **27,** 294–299. ISSN: 1941-5982 (Apr. 1864).

42. Jacobsen, A. J., Barvosa-Carter, W. & Nutt, S. Micro-scale Truss Structures formed from Self-Propagating Photopolymer Waveguides. *Advanced Materials* **19,** 3892–3896. ISSN: 0935-9648 (Oct. 2007).

43. Zheng, X. *et al.* Design and optimization of a light-emitting diode projection micro-stereolithography three-dimensional manufacturing system. *Review of Scientific Instruments* **83,** 125001. ISSN: 0034-6748 (Dec. 2012).

44. Maruo, S., Nakamura, O. & Kawata, S. Three-dimensional microfabrication with two-photon-absorbed photopolymerization. *Optics Letters* **22,** 132–134. ISSN: 1539-4794 (Jan. 1997).

45. Selimis, A., Mironov, V. & Farsari, M. Direct laser writing: Principles and materials for scaffold 3D printing. *Microelectronic Engineering. Micro and Nanofabrication Breakthroughs for Electronics, MEMS and Life Sciences* **132,** 83–89. ISSN: 0167-9317 (Jan. 2015).

46. Bauer, J. *et al.* Nanolattices: An Emerging Class of Mechanical Metamaterials. *Advanced Materials* **29,** 1701850. ISSN: 0935-9648 (Sept. 2017).

47. Zheng, X. *et al.* Ultralight, ultrastiff mechanical metamaterials. en. *Science* **344,** 1373–1377. ISSN: 0036-8075, 1095-9203 (June 2014).

48. Jang, D., Meza, L. R., Greer, F. & Greer, J. R. Fabrication and deformation of three-dimensional hollow ceramic nanostructures. en. *Nature Materials* **12,** 893–898. ISSN: 1476-1122 (Oct. 2013).

49. Chen, G. *Nanoscale Energy Transport and Conversion : A Parallel Treatment of Electrons, Molecules, Phonons, and Photons* ISBN: 978-0-19-977468-5 (Oxford University Press, Feb. 2005).

50. Sondheimer, E. H. The mean free path of electrons in metals. *Advances in Physics* **1,** 1–42. ISSN: 0001-8732 (Jan. 1952).

51. Balandin, A. & Wang, K. L. Significant decrease of the lattice thermal conductivity due to phonon confinement in a free-standing semiconductor quantum well. *Physical Review B* **58,** 1544–1549 (July 1998).

52. Liu, W. & Asheghi, M. Phonon–boundary scattering in ultrathin single-crystal silicon layers. *Applied Physics Letters* **84,** 3819–3821. ISSN: 0003-6951 (Apr. 2004).

53. Volz, S. G. & Chen, G. Molecular dynamics simulation of thermal conductivity of silicon nanowires. *Applied Physics Letters* **75,** 2056–2058. ISSN: 0003-6951 (Sept. 1999).

54. Li, D. *et al.* Thermal conductivity of individual silicon nanowires. *Applied Physics Letters* **83,** 2934–2936. ISSN: 0003-6951 (Sept. 2003).

55. Cahill, D. G. *et al.* Nanoscale thermal transport. *Journal of Applied Physics* **93,** 793–818. ISSN: 0021-8979, 1089-7550 (Jan. 2003).

56. Dou, N. G. & Minnich, A. J. Heat conduction in multifunctional nanotrusses studied using Boltzmann transport equation. *Applied Physics Letters* **108,** 011902. ISSN: 0003-6951 (Jan. 2016).

57. Majumdar, A. Microscale Heat Conduction in Dielectric Thin Films. *Journal of Heat Transfer* **115,** 7–16. ISSN: 0022-1481 (Feb. 1993).

58. Peterson, R. B. Direct Simulation of Phonon-Mediated Heat Transfer in a Debye Crystal. *Journal of Heat Transfer* **116,** 815–822. ISSN: 0022-1481 (Nov. 1994).

59. Mazumder, S. & Majumdar, A. Monte Carlo Study of Phonon Transport in Solid Thin Films Including Dispersion and Polarization. *Journal of Heat Transfer* **123,** 749–759. ISSN: 0022-1481 (Jan. 2001).

60. Lacroix, D., Joulain, K. & Lemonnier, D. Monte Carlo transient phonon transport in silicon and germanium at nanoscales. *Physical Review B* **72,** 064305 (Aug. 2005).

61. Jeng, M.-S., Yang, R., Song, D. & Chen, G. Modeling the Thermal Conductivity and Phonon Transport in Nanoparticle Composites Using Monte Carlo Simulation. *Journal of Heat Transfer* **130,** 042410–042410–11. ISSN: 0022-1481 (Mar. 2008).

62. Hao, Q., Chen, G. & Jeng, M.-S. Frequency-dependent Monte Carlo simulations of phonon transport in two-dimensional porous silicon with aligned pores. *Journal of Applied Physics* **106,** 114321. ISSN: 0021-8979 (Dec. 2009).

63. Péraud, J.-P. M. & Hadjiconstantinou, N. G. Efficient simulation of multidimensional phonon transport using energy-based variance-reduced Monte Carlo formulations. *Phys. Rev. B* **84,** 205331 (Nov. 2011).

64. Péraud, J.-P. M. & Hadjiconstantinou, N. G. An alternative approach to efficient simulation of micro/nanoscale phonon transport. *Applied Physics Letters* **101,** 153114. ISSN: 0003-6951, 1077-3118 (Oct. 2012).

65. Minnich, A. J., Chen, G., Mansoor, S. & Yilbas, B. S. Quasiballistic heat transfer studied using the frequency-dependent Boltzmann transport equation. *Phys. Rev. B* **84,** 235207 (Dec. 2011).

66. Dames, C. & Chen, G. 1ω, 2ω, and 3ω methods for measurements of thermal properties. *Review of Scientific Instruments* **76,** 124902. ISSN: 0034-6748 (Dec. 2005).

67. Cahill, D. G. Thermal conductivity measurement from 30 to 750 K: the 3ω method. *Review of Scientific Instruments* **61,** 802–808. ISSN: 0034-6748, 1089-7623 (Feb. 1990).

68. Feser, J. P. *Scalable Routes to Efficient Thermoelectric Materials* PhD thesis (2010).

69. Meza, L. R., Das, S. & Greer, J. R. Strong, lightweight, and recoverable three-dimensional ceramic nanolattices. en. *Science* **345,** 1322–1326. ISSN: 0036-8075, 1095-9203 (Sept. 2014).

70. Borca-Tasciuc, T., Kumar, A. R. & Chen, G. Data reduction in 3ω method for thin-film thermal conductivity determination. *Review of Scientific Instruments* **72,** 2139–2147. ISSN: 0034-6748, 1089-7623 (Apr. 2001).

71. Lee, S.-M., Cahill, D. G. & Allen, T. H. Thermal conductivity of sputtered oxide films. *Physical Review B* **52,** 253–257 (July 1995).

72. Carslaw, H. S. & Jaeger, J. C. *Conduction of Heat in Solids* 2nd ed. ISBN: 978-0-19-853368-9 (Oxford University Press, Oxford, New York, Apr. 1986).

73. Touloukian, Y. S., Powell, R. W., Ho, C. Y. & Klemens, P. G. *Thermophysical Properties of Matter - The TPRC Data Series* en (1970).

74. Dou, N. G., Jagt, R. A., Portela, C. M., Greer, J. R. & Minnich, A. J. Ultralow thermal conductivity and mechanical resilience of architected nanolattices (in review).

75. Groner, M. D., Fabreguette, F. H., Elam, J. W. & George, S. M. Low-Temperature Al2O3 Atomic Layer Deposition. *Chemistry of Materials* **16,** 639–645. ISSN: 0897-4756 (Feb. 2004).

76. Kahlbaum, G. W. A., Roth, K. & Siedler, P. Über Metalldestillation und über destillierte Metalle. en. *Zeitschrift für anorganische Chemie* **29,** 177–294. ISSN: 1521-3749 (Jan. 1902).

77. Freeman, J. J. & Anderson, A. C. Thermal conductivity of amorphous solids. *Physical Review B* **34,** 5684–5690 (Oct. 1986).

78. Cahill, D. G. & Pohl, R. O. Thermal conductivity of amorphous solids above the plateau. *Physical Review B* **35,** 4067–4073 (Mar. 1987).

79. Meza, L. R. *et al.* Reexamining the mechanical property space of three-dimensional lattice architectures. *Acta Materialia* **140,** 424–432. ISSN: 1359-6454 (Aug. 2017).

80. Meza, L. R. *et al.* Resilient 3D hierarchical architected metamaterials. en. *Proceedings of the National Academy of Sciences* **112,** 11502–11507. ISSN: 0027-8424, 1091-6490 (Sept. 2015).

81. Berdova, M. *et al.* Mechanical assessment of suspended ALD thin films by bulge and shaft-loading techniques. *Acta Materialia* **66,** 370–377. ISSN: 1359-6454 (Mar. 2014).

82. Yang, L. & Minnich, A. J. Thermal transport in nanocrystalline Si and SiGe by *ab initio* based Monte Carlo simulation. *Scientific Reports* **7,** 44254. ISSN: 2045-2322 (Mar. 2017).

83. Chiritescu, C. *et al.* Ultralow Thermal Conductivity in Disordered, Layered WSe_2 Crystals. en. *Science* **315,** 351–353. ISSN: 0036-8075, 1095-9203 (Jan. 2007).

84. Bauer, J., Schroer, A., Schwaiger, R. & Kraft, O. Approaching theoretical strength in glassy carbon nanolattices. *Nature Materials* **15,** 438–443. ISSN: 1476-4660 (Apr. 2016).

85. Jeon, S. *et al.* Fabricating complex three-dimensional nanostructures with high-resolution conformable phase masks. *Proceedings of the National Academy of Sciences* **101,** 12428–12433. ISSN: 0027-8424, 1091-6490 (Aug. 2004).

86. Divliansky, I., Mayer, T. S., Holliday, K. S. & Crespi, V. H. Fabrication of three-dimensional polymer photonic crystal structures using single diffraction element interference lithography. *Applied Physics Letters* **82,** 1667–1669. ISSN: 0003-6951 (Mar. 2003).